1971

An Orthogonal Meteor Scatter System For The Measurement Of Wind Velocities

Ernest Salo Hanff

AN ORTHOGONAL METEOR SCATTER SYSTEM FOR THE MEASUREMENT OF WIND VELOCITIES

by

Ernest Salo Hanff
Faculty of Engineering Science

Submitted in partial fulfillment
of the requirements for the degree of
Doctor in Philosophy

Faculty of Graduate Studies
The University of Western Ontario
London, Canada
August 1971

ABSTRACT

The feasibility of using an orthogonal forward scatter system for the measurement of winds in the meteor region is investigated. Such a system is attractive because of its simplicity, relatively low cost and negligible attendance requirements.

Results obtained with a simplified prototype model, although not sufficiently accurate, indicate the suitability of the proposed system for the intended purpose.

An overall design proposal for a definitive working model is presented on the basis of the performance of the prototype system.

PREFACE

This work basically represents a study of the feasibility of a novel meteor region wind velocity measuring system. The nature of such a work suggests a rather unconventional approach to the organization of the text. For the sake of continuity a number of subjects that more or less digress from the main line of argument are relegated to appendices.

The first chapter presents some background on winds in the meteor region and methods to measure them; it also explains the advantages of the proposed system. Further details are found in Appendix 1 and Chapter 2 which contains a very brief summary of meteor physics relevant to the work at hand and radio echo theory as well as a review of the properties of the winds in the meteor region. This information serves as a basis on which the necessary specifications for the system are selected.

The prototype model is described in detail in Chapter 3 where its operation is also explained. The results obtained are presented and discussed in Chapter 4 with a detailed error analysis given in Appendix 7.

Chapter 5 presents a design proposal for a definitive working model based on the performance of the prototype.

A chapter on discussion and conclusions has been omitted since it would merely represent a duplication of topics previously discussed.

The author wishes to express his appreciation to Prof. P. A. Forsyth of the Department of Physics for his guidance and unwavering support of the present work. The innumerable fruitful discussions with Prof. G. F. Chess of the Faculty of Engineering Science and his extraordinary patience during the revisions of the manuscript are also greatly appreciated.

The project was substantially supported by the Federal Department of Transport (Purchase Order H1861).

TABLE OF CONTENTS

LIST OF ILLUSTRATIONS

LIST OF TABLES

GLOSSORY OF SYMBOLS

A	Effective antenna aperture
B	System bandwidth
B_{HF}	Predetection bandwidth
d	Antenna separation
D	Diffusion coefficient
g	Antenna numerical gain
G_R	Receiver antenna gain in direction of interest
G_T	Transmitter antenna gain in direction of interest
H	Atmospheric density scale height
k	Boltzman's constant
P_N	Receiver noise power
$P_R(t)$	Received echo power
P_T	Transmitted power
q	Electron line density
R_1	Transmitter range of target
R_2	Receiver range of target
r_o	Initial trail radius
S	RMS signal amplitude
S	Envelope amplitude
t	Time
T_{un}	Underdense echo decay time

T_{ov}	Overdense echo duration
v	Velocity of meteoroid
α	Receiver azimuth angle
α	Interferometer direction cone semi-angle
α_o	Angle between N-S and E-W antenna pair axes
β	Angle between trail and intersection of the propagation and tangent plane
γ	Angle between incident electric vector and the receiver line of sight
δ	Transmitter azimuth angle of the target
ε	Elevation of received signal
η	Angle between the N-S and E-W direction cones at their intersection
θ	Angle between the incident ray and antenna pair axis
λ	Wavelength
ρ_a	Air density
ρ_{amax}	Air density at height of maximum ionization
σ	RMS noise amplitude
σ	RMS height error
τ	Post-detection bandwidth
ϕ	One half of scattering angle
ϕ	Azimuth angle measured from broadside array axis

Φ	Zero crossing error
χ	Meteor zenith angle
ψ	Phase angle between signals arriving at two antennas
ψ_c	Receiving system phase constant
ψ_{c1}	Receiver phase constant
ψ_{c2}	Phase constant of antennas, preamplifiers and transmission lines

CHAPTER 1

INTRODUCTION

It has been recognized for many years that variations in the earth's magnetic field are related to large scale motions in the ionosphere; evidence of the highly dynamic ionospheric state at slightly lower altitudes has been found in the motion and distortion of bright, long-enduring meteors as well as of the rare noctiluscent clouds. The mechanisms governing atmospheric motions are not fully known in spite of significant efforts directed toward understanding them by scientists in the various atmospheric disciplines. Foremost are the meteorologists, for whom a more complete grasp of the physical phenomena that determine these motions as well as other properties of the atmosphere, could prove to be an invaluable aid in weather forecasting and conceivably even in developing methods to control climatic conditions. The connections between lower and upper atmospheric motions are not yet clear, but it seems that an attempt to determine them should begin with a wide scale comprehensive study of ionospheric motions coupled with investigations

in the lower levels. In addition, space scientists in predicting the reentry of space vehicles, require a good knowledge of the air density and motion in the meteor region where most of the deceleration takes place. These requirements justify the investigation of motions in the 70 - 100 km height range.

Figure 1 shows the various methods used to measure ionospheric movements with their respective applicable height ranges and Table 1 summarizes the main characteristics of each (Kent and Wright, 1967). The absence of other suitable natural targets that follow the local air motions, lead to the conclusion that the radio meteor system is the only viable method for accurate and economical routine wind measurements in the lower E-region.

It is widely accepted that meteor trails are carried by the motion of neutral particles at heights up to about 95 km, above which magnetic forces may play an important roll in determining the movement of the charged particles (Kaiser, Pickering and Watkins, 1969). Within these limitations, it is sufficient to observe by means of radio methods the movement of the reflecting point (basically the centre of the principal Fresnel zone) on the trail to obtain the wind velocity at the corresponding location. This is usually done by determining the

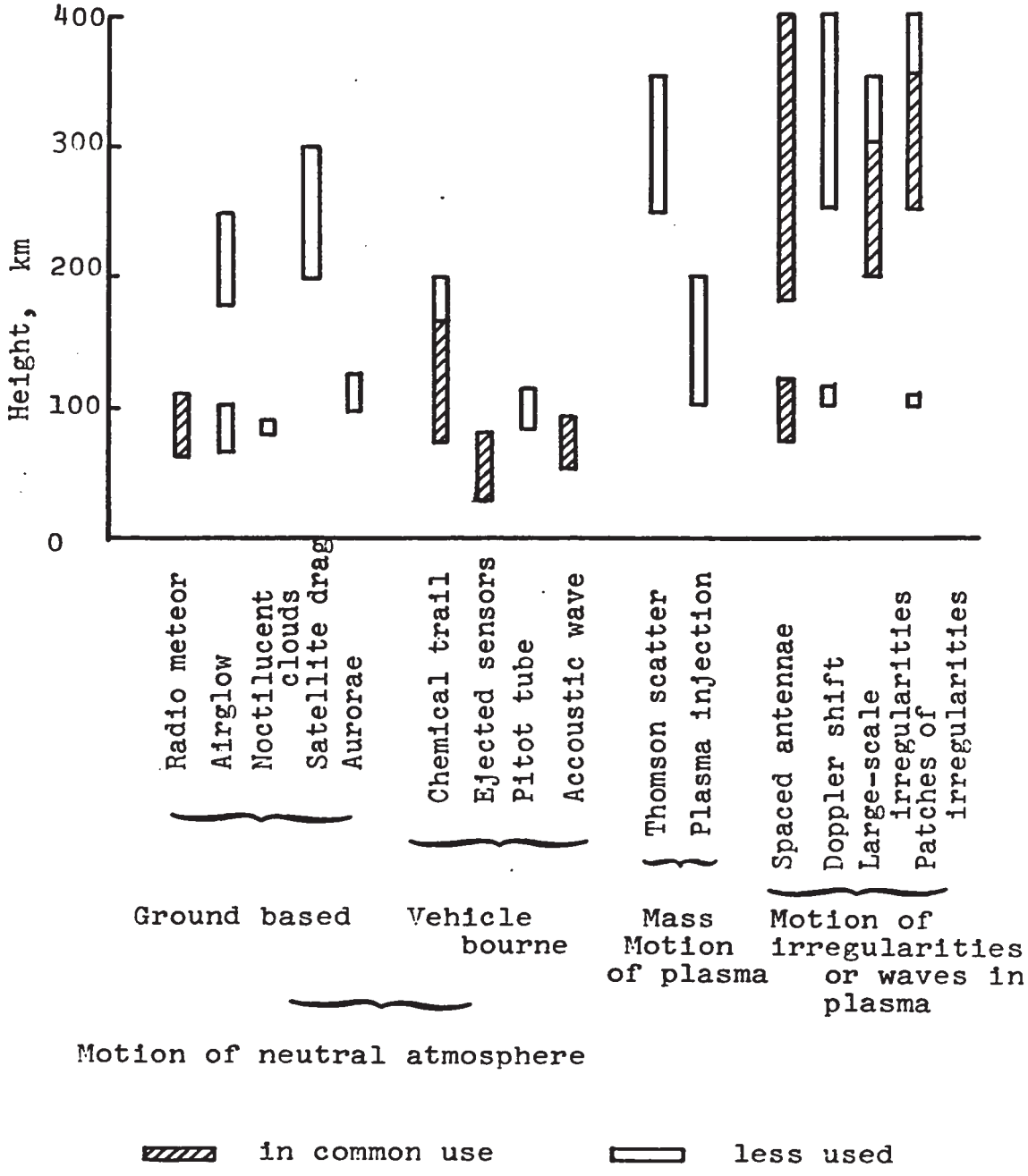

Fig. 1 Methods of measuring ionospheric movements and their heights of operation (After Kent and Wright, 1967)

TABLE 1 PRINCIPAL ADVANTAGES AND DISADVANTAGES OF THE METHODS OF MEASURING IONOSPHERIC MOTIONS (AFTER KENT AND WRIGHT, 1967)

Method	Class	Main Characteristics
Radio meteor	N	Relatively simple direct method, restricted height range.
Airglow	N	Little used, interpretation difficult.
Noctilucent clouds	N	Shows horizontal behaviour, very restricted height range, relatively rare events.
Satellite drag	N	Only available neutral method above 200 km. Requires extensive averaging.
Aurorae	N	Very dubious interpretation.
Chemical trail	N	Very direct, trail lifetime only a few minutes, night-time only.
Ejected sensors	N	Restricted to heights below 80 km.
Pitot tube	N	Little used.
Acoustic wave	N	Restricted to heights below 90 km.

continued...

TABLE 1 Continued

Method	Class	Main Characteristics
Thomson scatter	P	A new method of considerable promise. Needs sophisticated equipment.
Plasma injection	P	Relatively little used, similar to chemical trail.
Close-spaced antennae	I	Very common, interpretation under debate.
Doppler shift	I	Particularly used to observe waves in plasma.
Large-scale irregularities	I	A variety of methods, not applicable to small irregularities.
Patches of irregularities	I	Restricted to certain classes of ionospheric irregularities.

N = neutral atmosphere: P = bulk plasma: I = plasma irregularity.

Doppler shift of the received signal which is proportional to the rate of change in the propagation path length. As winds have been found to be substantially horizontal (Manning et al, 1950; Robertson et al, 1953), only the horizontal wind component is considered necessary.

It is well known that the wind structure in the meteor region is highly anisotropic, having quite short vertical correlation lengths as opposed to very long horizontal ones (Greenhow and Neufeld, 1959a);it is therefore evident that in order to obtain meaningful wind velocity profiles, the height of the reflection point needs to be determined with a much higher accuracy that the other two spatial coordinates. Occasionally the height is obtained from the decay times of underdense echoes, however this method has proven to be inaccurate on an individual echo basis although statistically it appears to be adequate (see Chapter 2). A more widespread approach is to locate the reflection point by triangulation. This method provides more accuracy and as it is independent of echo shape the criteria for the selection of useful echoes may be relaxed.

Most of the existing systems (discussed in Appendix 1), are monostatic or closely spaced multistatic back-scatter radars that essentially provide only one wind

velocity component. The determination of the horizontal wind vector requires two components, preferably orthogonal for higher accuracy. These could be obtained with existing systems either by using a single station to observe two regions in the sky, or by using two widely separated stations whose radiation lobes converge orthogonally on the region under observation. The former method has the drawback that in order to have such two distinct components, it is necessary to have a horizontal separation between the two regions which is sufficient to significantly reduce the correlation between the winds in them, and the latter requires two complete systems, each with attending personnel, making this solution economically unattractive, particularly if wide coverage is desired by means of many stations.

It appeared that both these difficulties could be circumvented by using a system based on a forward scatter geometry and consisting of two extremely simple and economical remote transmitting stations requiring no attendance except for occasional maintenance and one receiving station containing part or all of the data processing facilities. In addition, this geometry provides a smaller scattering loss, an increase in the echo duration as well as allowing the use of continuous

wave (cw) transmissions whose advantages are listed in Appendix 1.

The proposed geometry is shown in Figure 2. Transmitting stations, T_1 and T_2 send CW signals toward the volume under observation, P where meteors with orientations that satisfy the condition of specularity reflect the signal from either or both transmitting stations to the receiving site, R. The Doppler shift of the signals received from T_1 and T_2 provide the reflection point drift component along the bisectors of the corresponding scattering angles, V_1 and V_2 which are orthogonal as a result of the selected geometry. The reflection point

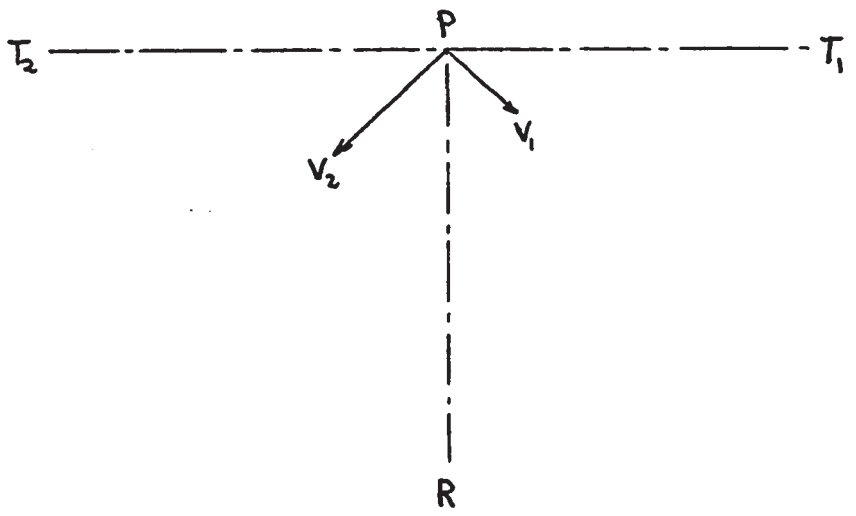

Fig. 2 Plan view of proposed geometry

is located by determining the direction of arrival of the received signal and the trail azimuth as seen from the transmitting stations. Details of the methods used to accomplish this are given in Chapter 3 where a detailed description of the complete system is presented.

The main object of the project was to develop a prototype model that could be used to assess the effectiveness of the proposed system which by virtue of its novelty required an empirical investigation of various unknown parameters to be used in the design of a definitive working model.

CHAPTER 2

THEORETICAL REVIEW

As an exhaustive coverage of the theory associated with meteor region wind measurements is beyond the scope of this work, only a brief summary of some of the most pertinent aspects are presented in this chapter. Others are mentioned in those sections where their relevancy is more manifest. The chapter is divided as follows:

(1) Meteoroids and trails

(2) Meteor trail radio scatter

(3) Meteor region winds.

These topics have been treated extensively and unless stated otherwise, the information was obtained from the comprehensive book by McKinley (1961).

2.1 Meteoroids and Trails

The earth is continually being combarded by meteoroids ranging in weight from milligrams to several tons that can be divided into two groups depending on

their behaviour.

(a) Shower meteoroids share a common orbit and thereby appear to originate from the same point on the celestial sphere (radiant of the shower). It is possible that they are the remnants of the destruction of a larger body.

(b) Non shower or sporadic meteoroids do not belong to a specific shower and consequently appear to originate from radiants distributed over the whole celestial sphere. The number of sporadic meteors arriving at a particular region varies diurnally as well as seasonally. The first variation can be explained in terms of the motion of the earth and the second by assuming a non uniform sporadic radiant distribution which is more dense near the ecliptic and biased toward certain ecliptic longitudes (Lovell, 1954; Weiss, 1957).

When a meteoroid penetrates the atmosphere, its kinetic energy is transformed through collisions with the air molecules mostly into heat as well as light and ionization. According to the simple evaporation theory, the ionization along the trail left by the passage of a meteoroid is

$$q = q_{max} \frac{9\rho_a}{4\rho_{amax}} \left(1 - \frac{\rho_a}{3\rho_{amax}}\right)^2 \qquad (2.1)$$

where:

q = electron line density at a height with atmospheric density ρ_a

q_{max} = maximum value of q occurring at a level where $\rho_a = \rho_{amax}$

q_{max} and ρ_{amax} are given by the following expressions,

$$q_{max} = \frac{4}{9} \frac{\beta}{\mu H} m \cos \chi \qquad (2.2)$$

$$\rho_{amax} = \frac{2\ell}{\Lambda v^2 AH} m^{1/3} \cos \chi \qquad (2.3)$$

where

β = probability that an ablated atom will produce a single ionization

μ = mass of meteor atom

H = atmospheric density scale height

m = initial mass of the meteoroid

χ = zenith angle of meteor trail

ℓ = heat of ablation of the meteoric material

Λ = heat transfer coefficient

v = velocity of meteoroid

$A = \lambda_0 m^{-2/3}$ where λ_0 is the initial cross section of the meteoroid normal to the line of flight.

Most meteors, however, are characterized by an irregular ionization component superimposed on the simple theoretical profile (Rice and Forsyth, 1963, 1964). The importance of this deviation is discussed in the next section.

2.2 Meteor Trail Radio Scatter

In the presence of an electromagnetic wave, the free electrons of a trail oscillate under the influence of the applied field thus scattering the signal. Depending on the electron density, there can be two distinct scattering mechanisms that give rise to the so-called underdense and overdense trails.

(a) Underdense trail: The electron line density is less than approximately 10^{14} m^{-1} and the interaction between the electrons is negligible, so that each is free to oscillate under the effect of the incident wave and act as an independent scattering unit.

(b) Overdense trail: In this case the electron line density exceeds 10^{14} m^{-1}, secondary scattering

between the electrons is important and the dielectric constant is negative throughout a significant volume within the trail. Under these conditions the trail reflects like a metallic conductor and there is a great attenuation of the signal penetrating the region of negative dielectric constant.

A wave incident on a trail is specularly reflected with most of the echo power originating at the principal Fresnel zone. Radar observation of trails can be accomplished with two scattering geometries depending on the separation between the transmitting and receiving stations. If they are closely spaced, the echo returns essentially along the same path as the transmitted signal giving rise to the backscatter case. However, if the two stations are widely separated, the echo travels along a distinctly different path, leading to a forward scatter geometry. Both of these cases are illustrated in Fig. 3. The various relationships pertinent to meteor radio echo theory are shown in the next sections.

2.2.1 Underdense Trail

(a) Forward scatter.

In the case of an underdense trail the echo amplit-

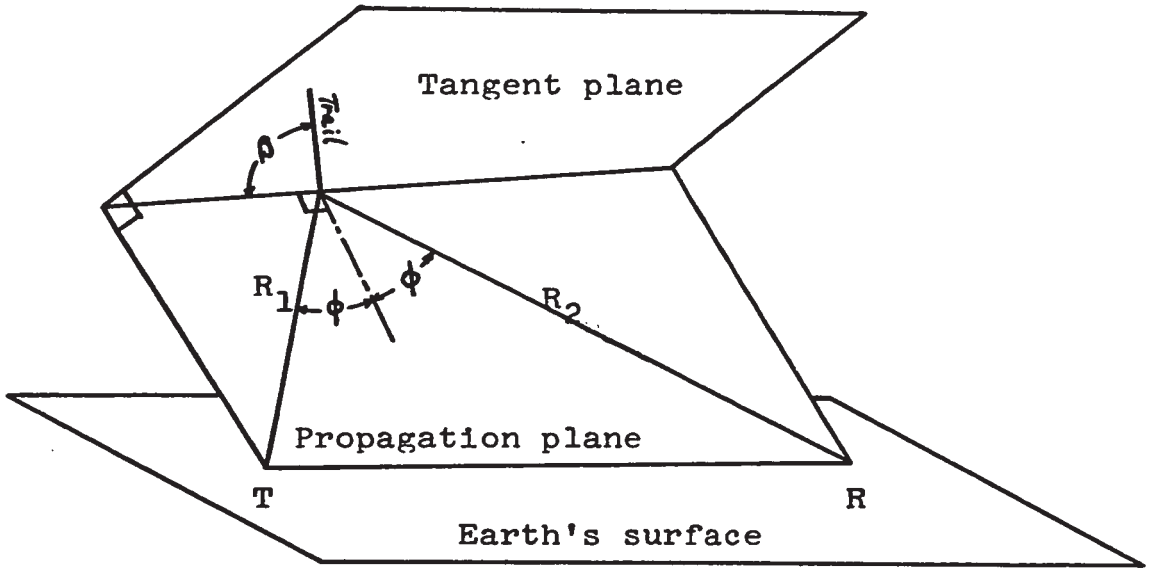

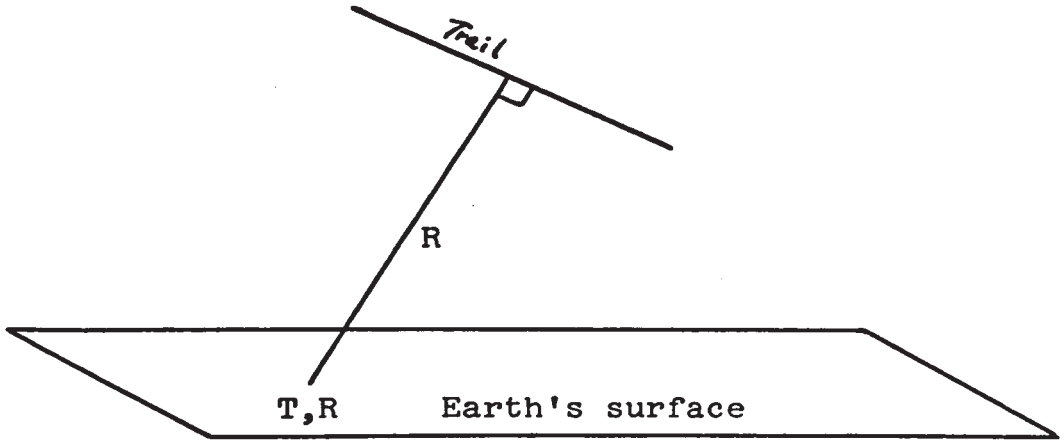

Fig. 3 Forward and backscatter geometries

ude rises rapidly during formation and subsequently decays exponentially due to the increasingly destructive interference between the signals scattered by electrons whose separation increases as a result of the expansion of the trail through diffusion. The received echo power after formation is:

$$P_R(t) = P_R(0)\exp-(8\pi^2 r_o^2 / \lambda^2 \sec^2\phi)\exp-(32\pi^2 Dt/\lambda^2 \sec^2\phi) \quad (2.4)$$

where t = time

λ = wavelength (m)

D = diffusion coefficient (m^2/sec)

r_o = initial trail radius (m)

ϕ = one half of scattering angle (Fig. 3)

$P_R(0)$ = received power from trail assumed to have zero radius and given by:

$$P_R(0) = 5\times10^{-32} P_T G_T G_R \lambda^3 \frac{q^2 \sin^2\gamma}{R_1 R_2 (R_1+R_2)(1-\sin^2\phi\cos^2\beta)} \quad (2.5)$$

where

P_T = transmitted power (watts)

G_T, G_R = transmitting and receiving antenna gains in the direction of interest

R_1, R_2 = transmitter and receiving ranges (Fig. 3)

γ = angle between incident electric vector and the line of sight of the receiver

β = angle between the trail and the intersection of the propagation and tangent planes (Fig. 3).

b) Back scatter.

In this case $\phi = 0$, $R_1 = R_2 = R$ and $\gamma = 0$, therefore (2.4) and (2.5) become

$$P_R(t) = P_R(0)\exp-(8\pi r_o^2/\lambda^2)\exp-(32\pi^2 Dt/\lambda^2) \quad (2.6)$$

$$P_R(0) = 2.5\times10^{-32}\ P_T G_T G_R \frac{\lambda^3}{R^3} q^2 \quad (2.7)$$

The first exponential terms of (2.4) and (2.6) correspond to the attenuation caused by the destructive interference due to the initial trail radius and the second describes the decay due to diffusion. Therefore the echo amplitude time constant (decay time) for the forward and back scatter geometries are

$$T_{un} = \frac{\lambda^2 \sec^2\phi}{16\pi^2 D} \quad (2.8)$$

$$T_{un} = \frac{\lambda^2}{16\pi^2 D} \quad (2.9)$$

and it follows that the forward scatter geometry provides longer durations as well as larger echo amplitudes which may be an asset in a wind measuring system.

2.2.2 Overdense Trail

The amplitude of an echo reflected from an overdense trail is characterized by a fast initial rise which slowly tapers off to a maximum and then decays rather rapidly. These echoes are usually much longer than the ones associated with underdense trails. Expressions for the echo powers in the forward and back scatter geometries are (Hines and Forsyth, 1957)

$$P_R(t) = \frac{P_T G_T G_R \lambda^2 \sin^2\gamma}{32\pi^2 R_1 R_2 (R_1+R_2)(1-\sin^2\phi\cos^2\beta)} \quad x \qquad (2.10)$$

$$x \sqrt{\frac{4Dt}{\sec^2\phi} \ln \left(\frac{\mu_o e^2}{4m} \frac{q\lambda^2\sec^2\phi}{4\pi^3 Dt}\right)}$$

and

$$P_R(t) = \frac{P_T G_T G_R \lambda^2}{64\pi^2 R^3} \sqrt{4Dt \ln \left(\frac{\mu_o e^2 q\lambda^2}{4m4\pi^3 Dt}\right)} \qquad (2.11)$$

where

μ_o = permeability of free space

m = electronic mass

e = electronic charge.

The corresponding durations, now defined as the time for the trail to become underdense are for the forward and backscatter geometries

$$T_{ov} = 7x10^{-17} \frac{\lambda^2 q \sec^2 \phi}{D}$$

and

$$T_{ov} = 7x10^{-17} \frac{\lambda^2 q}{D}$$

2.2.3 Height Determination From Decay Times

Equations (2.8) and (2.9) together with an expression for the diffusion coefficient as a function of altitude would seem to indicate that the height of the reflection point can be determined from the decay time of underdense meteors. Nevertheless Greenhow and Neufeld (1955), Weiss (1955), Murray (1959) and others found large discrepancies between the diffusion and triangulated heights, which could not be attributed to errors in the measurements. Various explanations have been suggested

to account for this discrepancy:

(a) Variations in diffusion coefficient

(b) Effect of the magnetic field of the earth on diffusion

(c) Distortion of the trail by winds

(d) Inclusion of meteors approaching critical density

(e) Distortion of exponential decay due to plasma resonance

(f) Finite meteoroid velocity

(g) Irregularities in the ionization along the trail.

The equivalent apparent scatter in the diffusion coefficient versus height persisted in multifrequency experiments that eliminated effects (a), (b) and (c). In addition a careful selection of the echoes used minimized the influence of (d), (e) and (f) leading to the conclusion that inhomogeneities in the ionization along the trail could cause the scatter. This view was supported by theoretical calculations based on a trail with a superimposed sinusoidal variation in its ionization (Rice and Forsyth, 1963) and subsequently confirmed experimentally (Rice and Forsyth, 1964). Inasmuch as

this scatter is unavoidable, it can be concluded that the decay time method is inadequate if heights are to be known accurately on an individual echo basis, however, it appears to be statistically satisfactory (Weiss, 1955; Murray, 1959).

2.3 Meteor Region Winds

The wind in the meteor region is fairly complex, basically consisting of three components that can be separated on the basis of their behaviour. The main features relevant to their measurement are considered in the following sections.

2.3.1 Prevailing Wind

This component is approximately constant over long periods of time and is approximately directed toward the east in summer and winter and toward the west in spring and autumn, although variations of this pattern have been reported. The uniformity of this wind arises from its quasi-equilibrium condition under the effects of a pressure gradient, Coriolis force resulting from the

rotation of the earth, and gravity (Hines, 1965).

Fig. 4 shows the average prevailing wind measured over a year at Jodrell Bank with latitude 53°N (Greenhow and Neufeld, 1955b): similar results have been found in Kharkov (50°N) and Obninsk (55°N) (Kashcheyev and Lysenko, 1967).

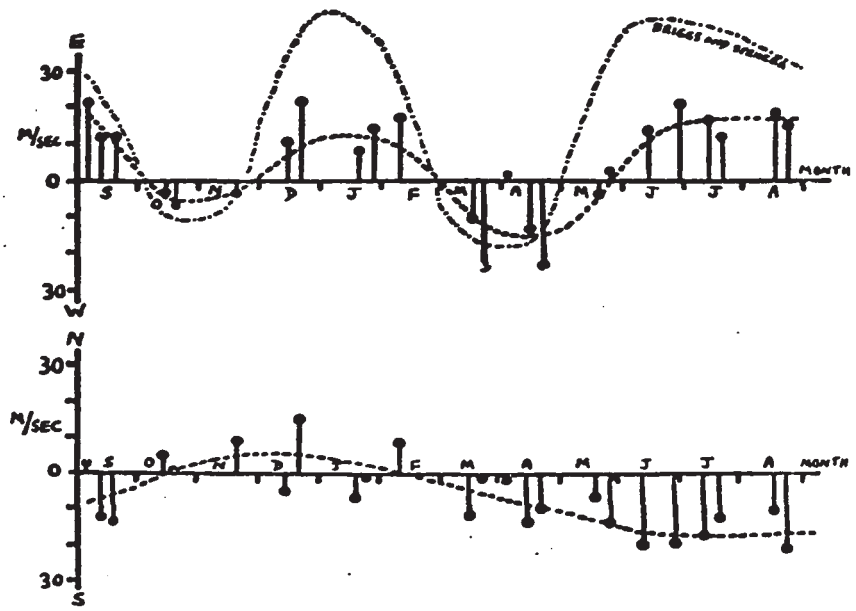

Fig. 4 Components of prevailing wind. Sept.53-Aug. 54. Points are shown for individual days. (After Greenhow and Neufeld, 1955b).

The prevailing wind gradients obtained at Jodrell Bank are shown in Fig. 5 (Greenhow and Neufeld, 1956); Elford (1959) reports gradients up to four times in excess of these. It should be noted that these gradients are usually fairly constant over the meteor region, an important

feature insofar as measurements are concerned.

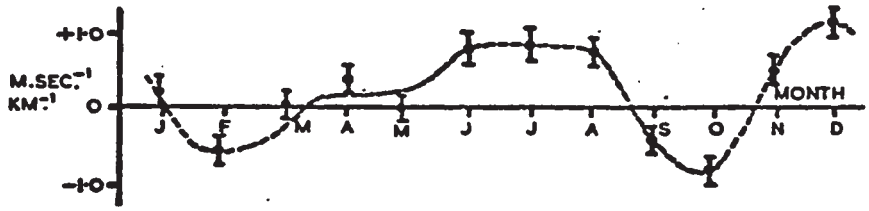

Fig. 5 Prevailing wind gradient (After Greenhow and Neufeld, 1956)

2.3.2 Tides

Superimposed on the prevailing wind are cyclic components with periods of 12 and 24 hours. Also weaker higher harmonics have been detected. These tides are attributed to thermal excitation of the atmosphere by the sun as well as to a minor gravitational influence of the sun and the moon.

Observations at Jodrell Bank have yielded a distinctly dominant semi diurnal component shown in Fig. 6 (Greenhow and Neufeld, 1956), whereas investigations at Adelaide revealed a dominant diurnal component (Elford and Robertson, 1953; Roper, 1968). Tidal amplitudes of 30 m/sec and shears of 3m/sec-km are common. As in the case of prevailing winds tides

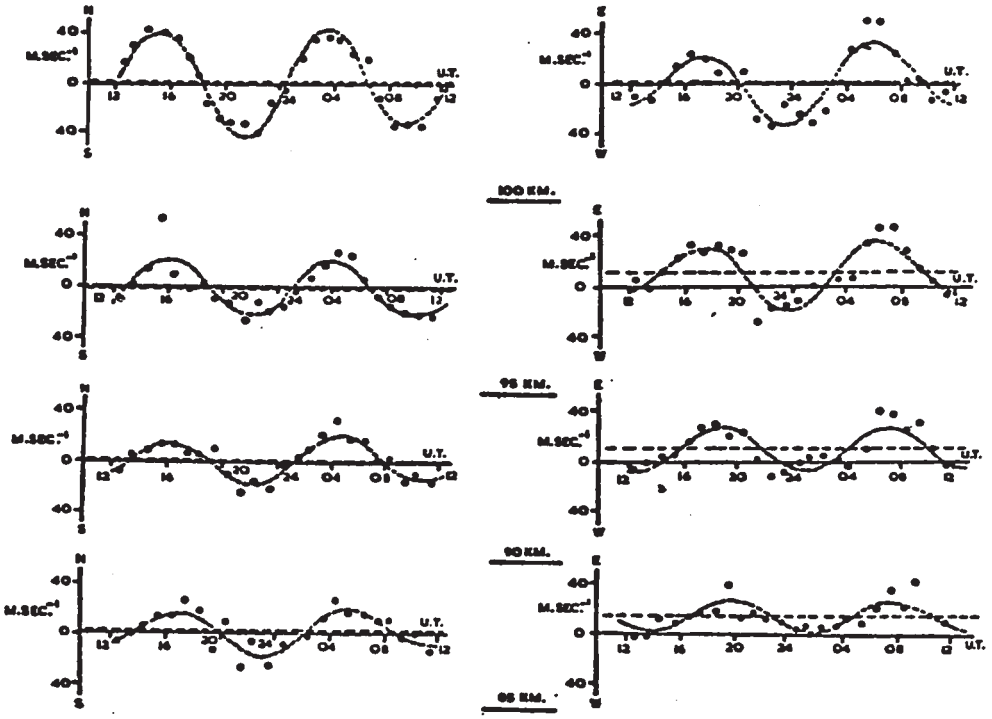

Fig. 6 Height variation of N-S and E-W wind components. The constant and sum of the first two periodic terms of the Fourier series are shown as broken lines. Sept. 16-17, 1954 (After Greenhow and Neufeld, 1956)

can easily be measured although a larger number of measurements are required because of their shorter periodicity.

2.3.3 Gravity Waves

In addition to the well organized tidal motions, there are highly anisotropic irregular wind components of comparable amplitude, with vertical and horizontal scales of approximately 6 and 150 km respectively and shears as high as 100 m/sec km. The statistical properties of these irregularities have been described by Greenhow and Neufeld (1959 a) using vertical spatial and temporal autocorrelation functions as depicted in Fig. 7; similar results were obtained by Spizzichino and Revah (1968).

Certain features of these irregularities led Hines (1960) to propose that the apparently random wind fluctuations resulted from the superposition of a broad spectrum of more coherent modes of propagation. This theory has been widely accepted and theoretical considerations based on it may be used to determine the requirements to be imposed upon a wind measuring system. The most important parameters are the minimum vertical

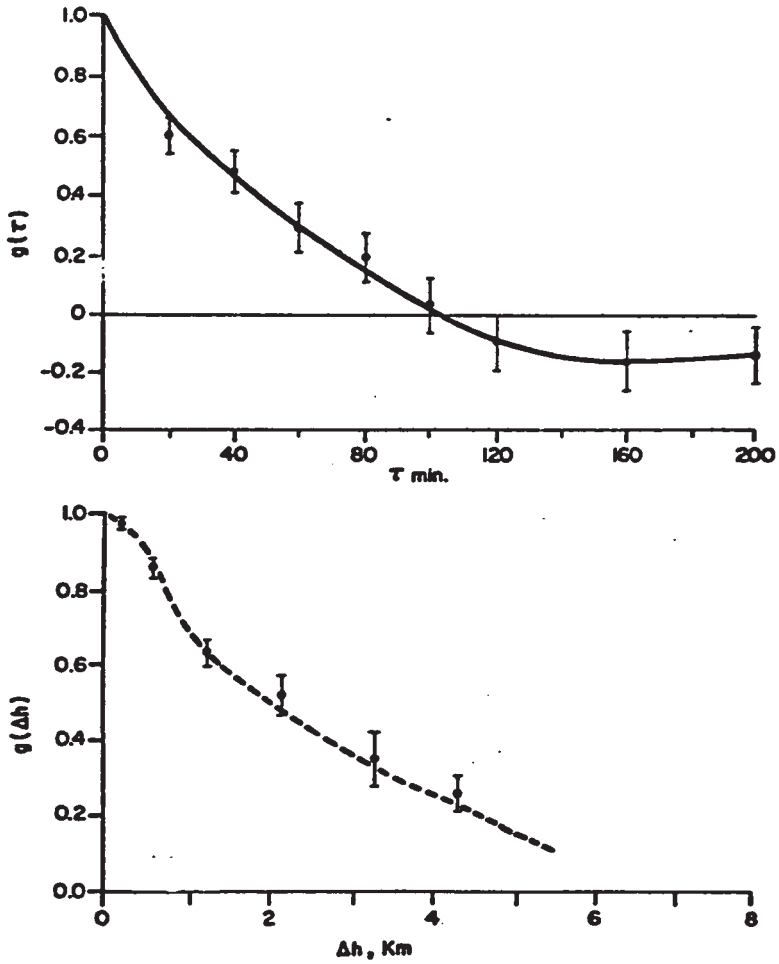

Fig. 7 Temporal and spatial autocorrelation coefficients of irregular wind component (After Greenhow and Neufeld, 1959 a)

wavelength and the shortest period that can propagate into the meteor region, the former being 100 m at 80 km height and 1 km at 100 km (although the smallest observed wavelengths have been at least three times as large (Hines, 1963) and the latter being approximately 10 minutes which is also several times shorter than the minimum observed periods. These are extreme values considerably more demanding from a measurement point of view than the dominant propagation modes at the corresponding heights, nonetheless, because of their small spatial and temporal structure, the observation of wind irregularities is far more difficult than that of the other components.

2.4 Determination of System Accuracies

The accuracies attainable with the system to be developed are determined by inherent limitations in the observational procedure as well as by noise, equipment limitations, and data processing.

Since the received echo amplitude can be assumed to be the integral of the signal scattered over the principal Fresnel zone of the trail, it would be meaningless

to define the position of the reflection point with an accuracy significantly smaller than the radius of the zone. Likewise, the observed apparent motion of the reflection point corresponds to some form of average over the complete Fresnel zone, which implies a smoothing of the very small wind structure. For the case described herein the radius of the zone is approximately 1 to 2 km depending on the trail orientation; however, its vertical projection remains at about 1 km, leading to the selection of a maximum error of 1 km in height due to the other sources mentioned above.

The accuracy required for the location of the reflection point in the horizontal plane is determined by the relative horizontal and vertical correlation lengths which are in a ratio of approximately 20 to 1. Therefore, if similar wind errors are desired as a result of an erroneous vertical or horizontal reflection point location, a horizontal accuracy of about 20 km is necessary.

In the presence of large shears, the error in height introduces significant errors in the determination of wind velocities which are difficult to evaluate due to the irregularities in the shear as well as the smoothing effect mentioned above. Average shears of 10

to 20 m/sec km are common (Greenhow and Neufeld, 1959 b; Kochanski, 1964) leading to errors in the order of 10 to 20 m/sec for 1 km error in height. In view of this rather large uncertainty, it does not appear to be economically justifiable to aim at extremely small wind measurement errors due to equipment limitations and data processing. An accuracy of 2 m/sec is fairly easy to achieve with reasonably priced oscillators and it would not unduly degrade the overall system accuracy.

CHAPTER 3

PROTOTYPE SYSTEM DESCRIPTION AND OPERATION

3.1 General

The general features of the proposed wind measuring system are described in Chapter 1, where it is shown that two identical subsystems, each consisting of a transmitting and receiving station (the latter common to both subsystems) are required for the determination of two orthogonal components of the wind velocity.

A prototype model was developed to assess the effectiveness of the proposed system. By virtue of the symmetry apparent from Fig. 2, the prototype may consist of only one of the required subsystems and any conclusions reached on the basis of its performance are equally applicable to the other. Consequently the prototype is composed of one transmitting and a simplified receiving station, and is therefore capable of determining

one wind velocity component.

The transmitting station is located in the vicinity of Ottawa, Ontario. It radiates two C.W. signals of approximately 18 watts at 40.3500 and 40.3505 MHz beamed in slightly diverging directions aimed approximately toward the west (Fig. 8).

The receiving station located in Delaware, Ontario, consists of three receivers connected to antenna arrays pointed in an approximately northward direction so that their beams intercept those of the transmitters roughly over Sudbury, Ontario which thus becomes the region under observation. When a meteor with an orientation that satisfies the condition for specularity between the two stations is produced in this region, it reflects the transmitted signal such that an echo is detected at the receiving site.

3.2 Location of Reflection Point

The location of the reflection point on the trail is determined by the following parameters,

(a) Transmitter azimuth angle of the target δ (Fig. 8)

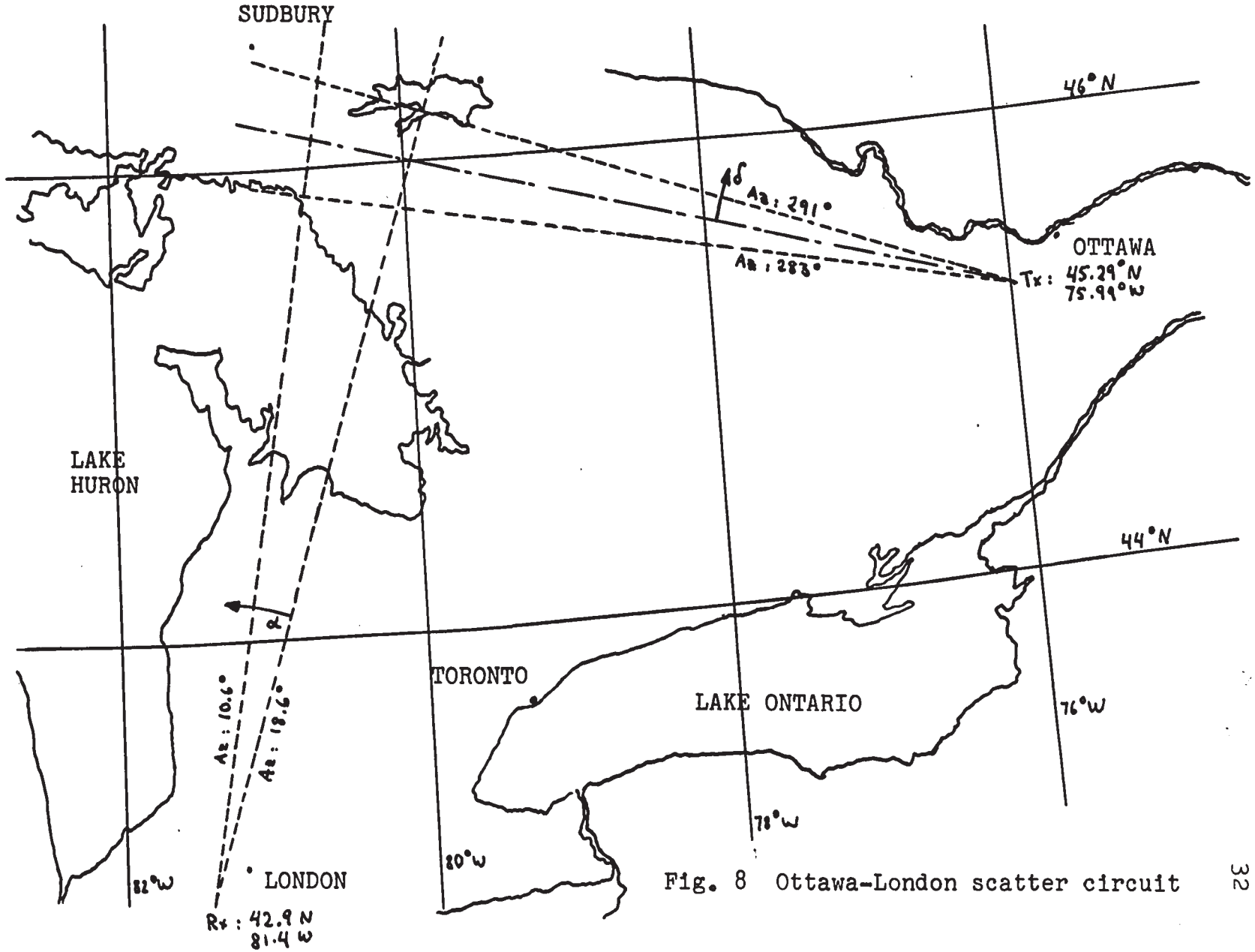

Fig. 8 Ottawa-London scatter circuit

(b) Azimuth angle of the received signal α (Fig. 8)

(c) Elevation angle of received signal ε

The transmitter azimuth of the target and the vertical at the transmitting site define a plane that contains the reflection point, which is identified by the intersection of the plane and the line defined by the azimuth and elevation angle of the received signal.

The methods used to determine the parameters are explained in the following sections; complete calculations to locate the reflection point are presented in Appendix 3.

3.2.1 Transmitter Azimuth Angle of Reflecting Point

Equations (2.4) and (2.10) give the received echo power in terms of system parameters and scattering geometry for the case of underdense and overdense trails respectively. Since the wavelengths of the two transmitted signals are virtually equal, the scattering geometry of both signals is identical for a given trail. Therefore the ratio of the powers received at the two frequencies is a function of only the gains of the

respective transmitter antenna array in the direction of interest. As a result of the diverging transmitting lobes the gains for any one reflection point generally differ and consequently the ratio of the received powers (and amplitudes) at both frequencies is a function of transmitter azimuth only. Barring ambiguities due to side lobes, there is a unique solution for the azimuth in terms of amplitude ratio. Fig. 9 shows such a relationship calculated for the theoretical transmitter radiation patterns (Appendix 2).

3.2.2 Azimuth and Elevation Angle of Received Signal

These parameters are indirectly obtained by determining the phase difference between the signals arriving at the three receiving antenna arrays whose layout in the receiving site is shown in Fig. 10. The geometry associated with the determination of the phase difference between the signals arriving at two antennas as a function of the incident ray direction is shown in Fig. 11. It is clear that

$$\psi = \frac{2\pi d}{\lambda} \cos \theta \qquad (3.1)$$

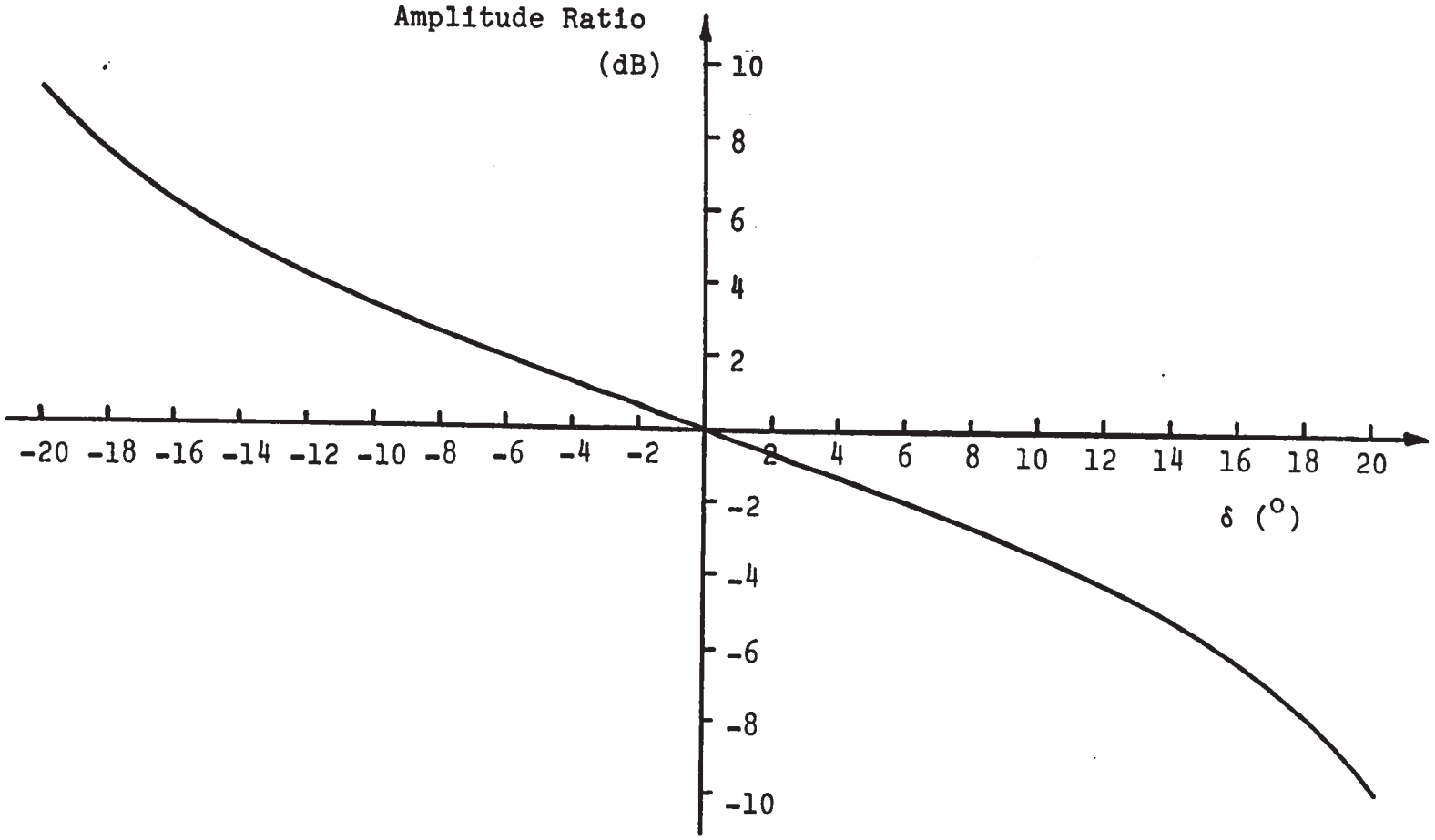

Fig. 9 Theoretical amplitude ratio as a function of transmitter azimuth

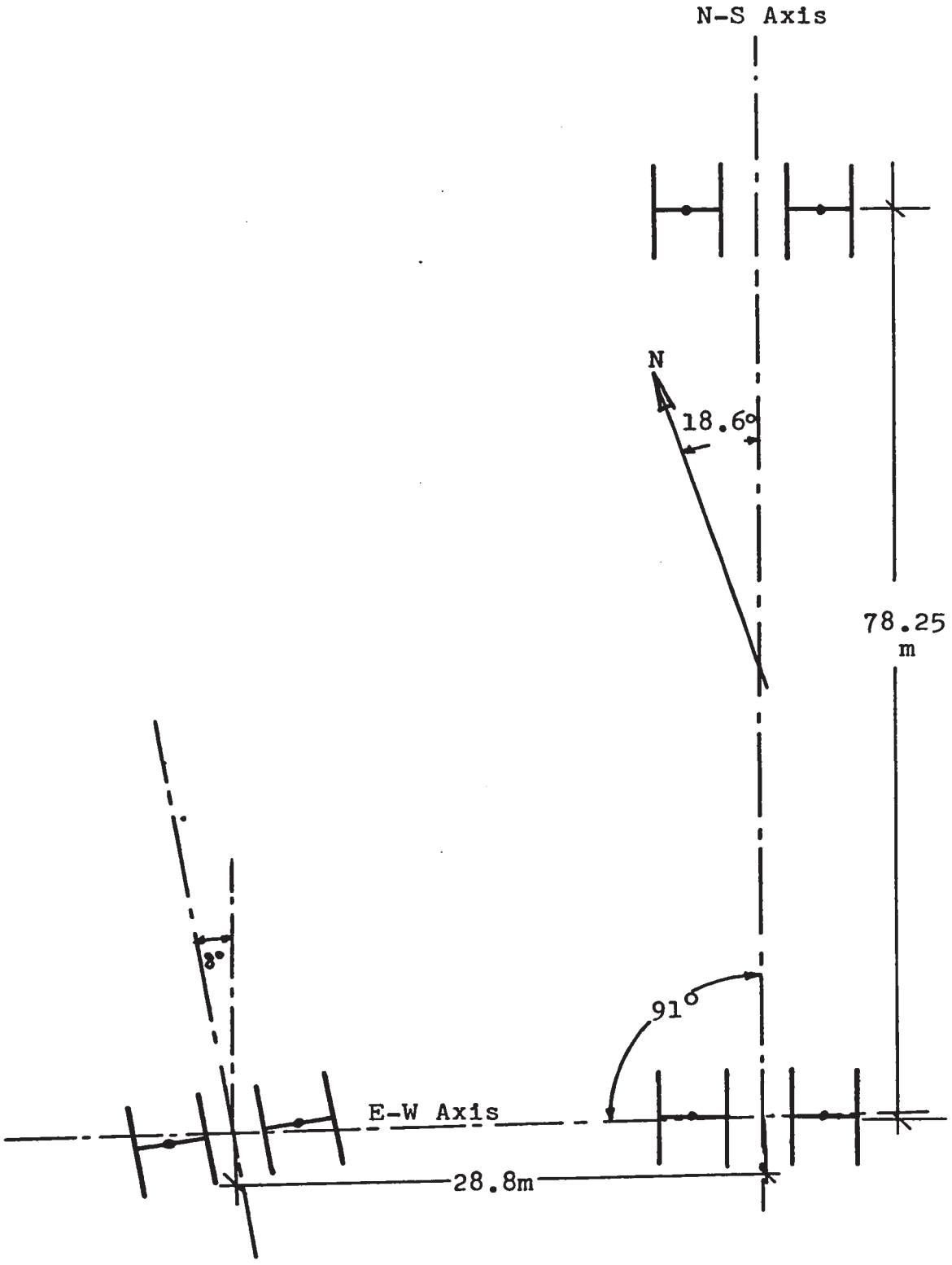

Fig. 10 Receiving antennas configuration

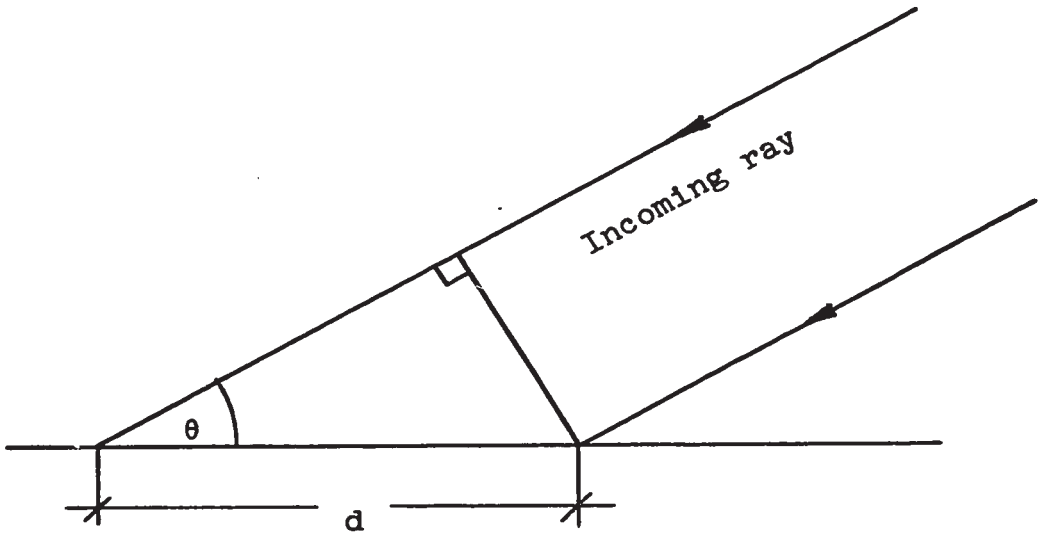

Fig. 11 Arrival angle geometry

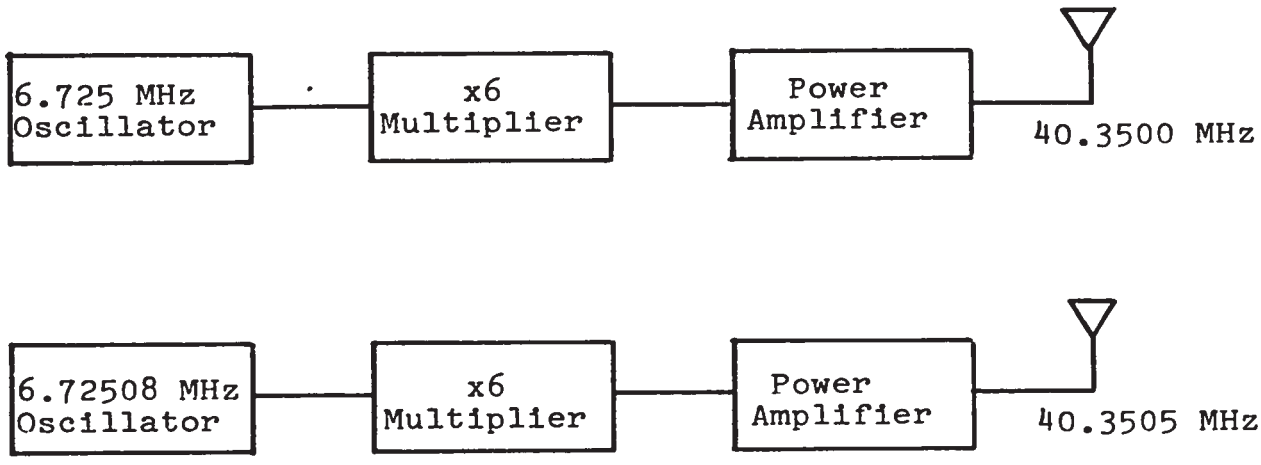

Fig. 12 Transmitting station block diagram

where:

ψ = phase difference between signals arriving at the two antennas

d = antenna separation

θ = angle between the incident ray and the axis joining the two arrays.

This expression has cylindrical symmetry about the antenna pair axis; therefore, for a given phase difference, the locus of the direction of arrival is a cone centered at the axis with semi-angle θ where

$$\theta = \cos^{-1} \frac{\lambda \psi}{2\pi d} \tag{3.2}$$

The direction of the incoming signal is defined by the intersection of the cones obtained from the application of equation (3.2) to the signals arriving at the N-S and E-W pairs. The azimuth and elevation angles are then given by (Appendix 3),

$$\alpha = \tan^{-1} \left(\frac{\cos \theta_{EW} - \cos \alpha_o \cos \theta_{NS}}{\sin \alpha_o \cos \theta_{NS}} \right) \tag{3.3}$$

$$\varepsilon = \cos^{-1} \left(\frac{\cos \theta_{NS}}{\cos \alpha} \right) \tag{3.4}$$

where:

α_o = angle between N-S and E-W array axis = 91°

θ = as defined in (3.2) for specified axis

ε = elevation angle of received signal

α = azimuth angle for received signal.

3.3 System Implementation

3.3.1 Transmitting Station

A block diagram of the transmitting station is shown in Fig. 12. It consists of two simple continuous wave transmitters each of which contains a high stability crystal controlled oscillator which is necessary in obtaining the desired accuracy in the measurement of wind velocities. The outputs of the transmitters are radiated by means of two arrays of four vertically polarized yagi antennas separated by half a wavelength. The arrays transmitting the 40.3500 and 40.3505 MHz signals are beamed at azimuths of 291 and 283 degrees respectively.

3.3.2 Receiving Station

A block diagram of the receiving system is shown

in Fig. 13, further details are given in Appendix 8. Antenna preamplifiers are required to offset the degradation in signal-to-noise ratio caused by the attenuation in the long transmission lines between the antennas and the receivers. As the two received signals must be separated for further processing, it is desirable to convert them to a lower frequency such that the separation can be achieved with fairly simple filters. Triple conversion receivers are used which provide outputs at 4.5 and 5 kHz corresponding to the received 40.3505 and 40.3500 MHz respectively. These signals are separated by means of m-derived passive filters each designed with a notch frequency to coincide with the frequency of the signal to be eliminated (Appendix 8).

(a) Direction finding

The direction finding is accomplished by comparing the phase between the 4.5 kHz outputs from the three receivers, which, as a result of the use of common local oscillators, preserve the relative phase difference between the received signals.

(b) Transmitter azimuth determination

The two signals used to determine the amplitude

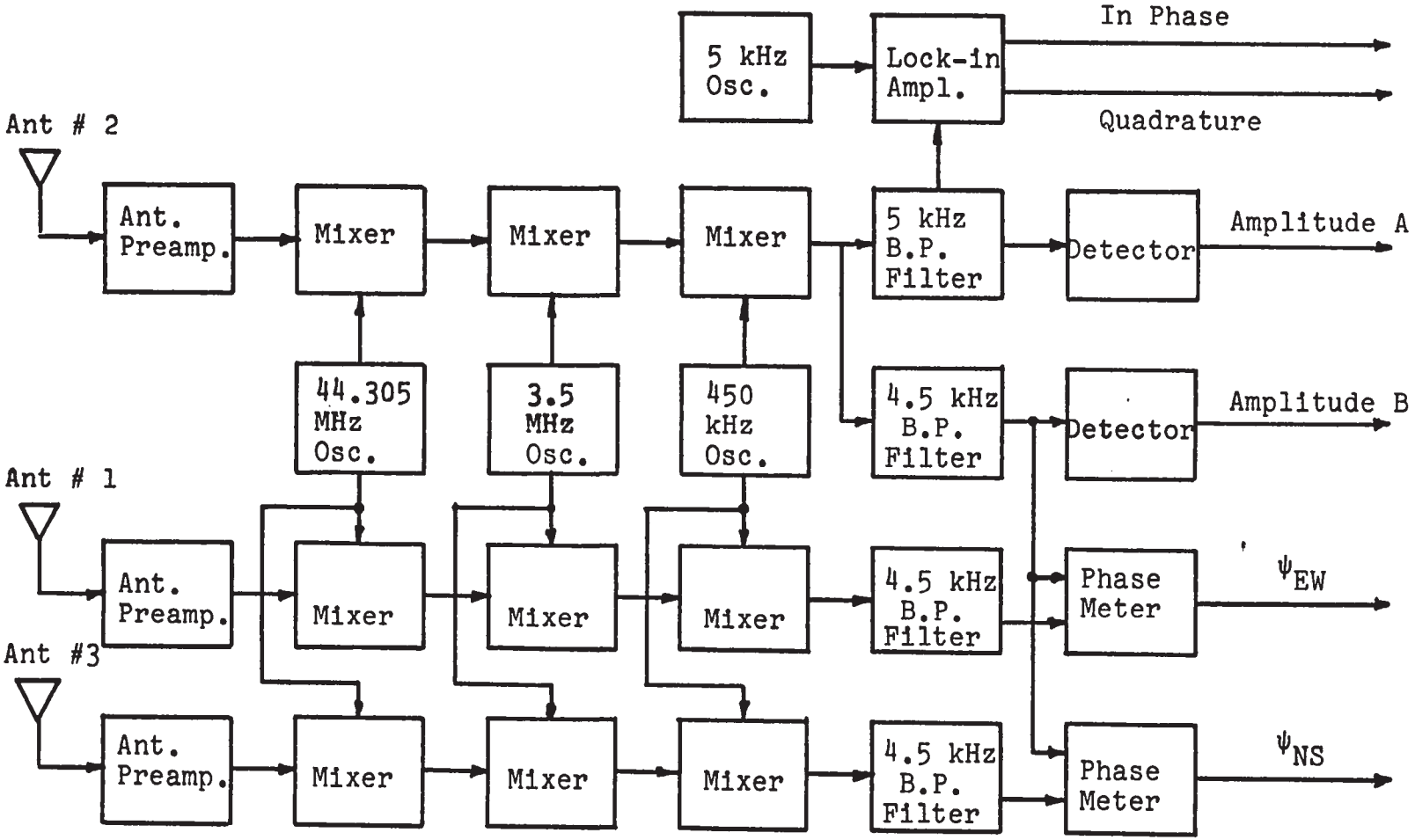

Fig. 13 Receiving system block diagram

ratio which in turn defines the transmitter azimuth, are processed by the same receiver to avoid errors due to receiver gain instability.

(c) Doppler measurements

The Doppler shift is obtained by comparing the 5 kHz receiver output with a 5 kHz reference signal in a lock-in amplifier whose output frequency is equal to the difference in frequency between the two input signals. The sense of the Doppler shift, necessary to establish whether the target is approaching or receding, is determined by the phase relationship between the "in phase" and "quadrature" outputs from the lock-in amplifier (Appendix 4).

The six outputs from the receiving system are fed into a paper chart recorder which displays them on individual channels except for the E-W phase difference which shares one channel with the IRIG C time code. The time code is disabled when a signal exceeding a threshold level is detected. A sample record is shown in Fig. 14.

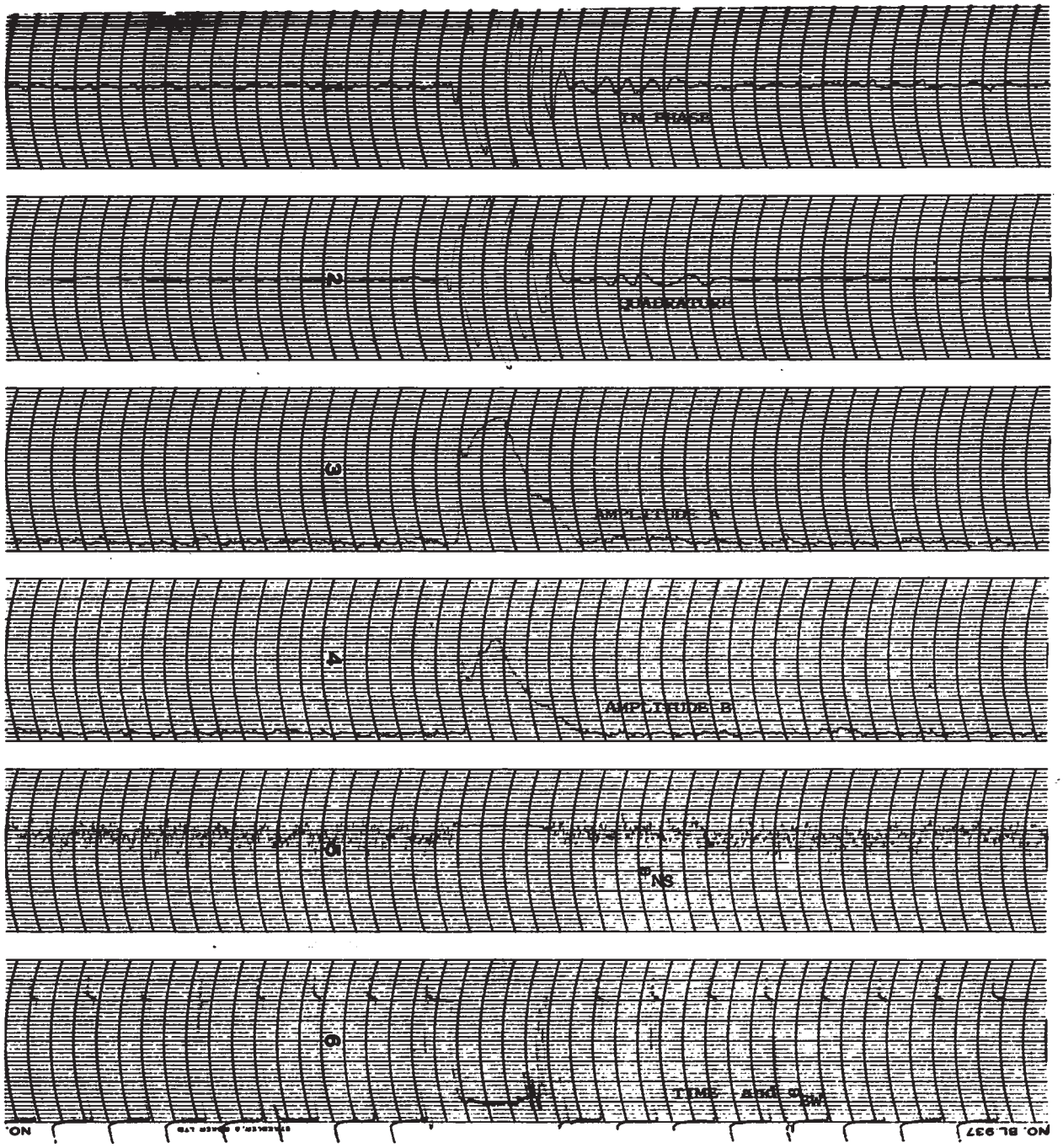

Fig. 14: Sample record

CHAPTER 4

PROTOTYPE SYSTEM PERFORMANCE

The main aspects of the performance of the prototype system are presented; these are the sensitivity, frequency stability, and accuracy in the determination of the height of the reflection point.

4.1 System Sensitivity

The sensitivity of the system determines the minimum electron line density that can be detected which in turn affects the number of meteors that can be observed in a given period of time. The electron line density required to obtain an echo with a given signal-to-noise ratio at the receiving station is a function of system and geometrical parameters as well as the noise power of the system. Equation (2.4) defines the received power in terms of the relevant system and geometrical

parameters for an underdense trail. Overdense meteors due to their very high electron line density need not be considered in the present discussion. In addition the received noise power is given by

$$P_N = k\, T_{SN}\, B \qquad (4.1)$$

where

k = Boltzman's constant = 1.38×10^{-23} joules/^{o}K

T_{SN} = system noise temperature (^{o}K)

B = system bandwidth in Hz.

The system noise temperature is approximately 7,300 ^{o}K (Appendix 5) and the predetection bandwidth 800 Hz. The bandpass characteristics for the subsystems that process both frequencies are depicted in Fig. 15. The rather unusual shapes are due to the use of m-derived filters with their notches at the undesired frequencies. The frequency response of the paper chart recorder used to display the output signals from the receiving system introduces a post detection bandwidth of approximately 100 Hz. An exact knowledge of the equivalent noise bandwidth of the receiving system is not necessary, therefore

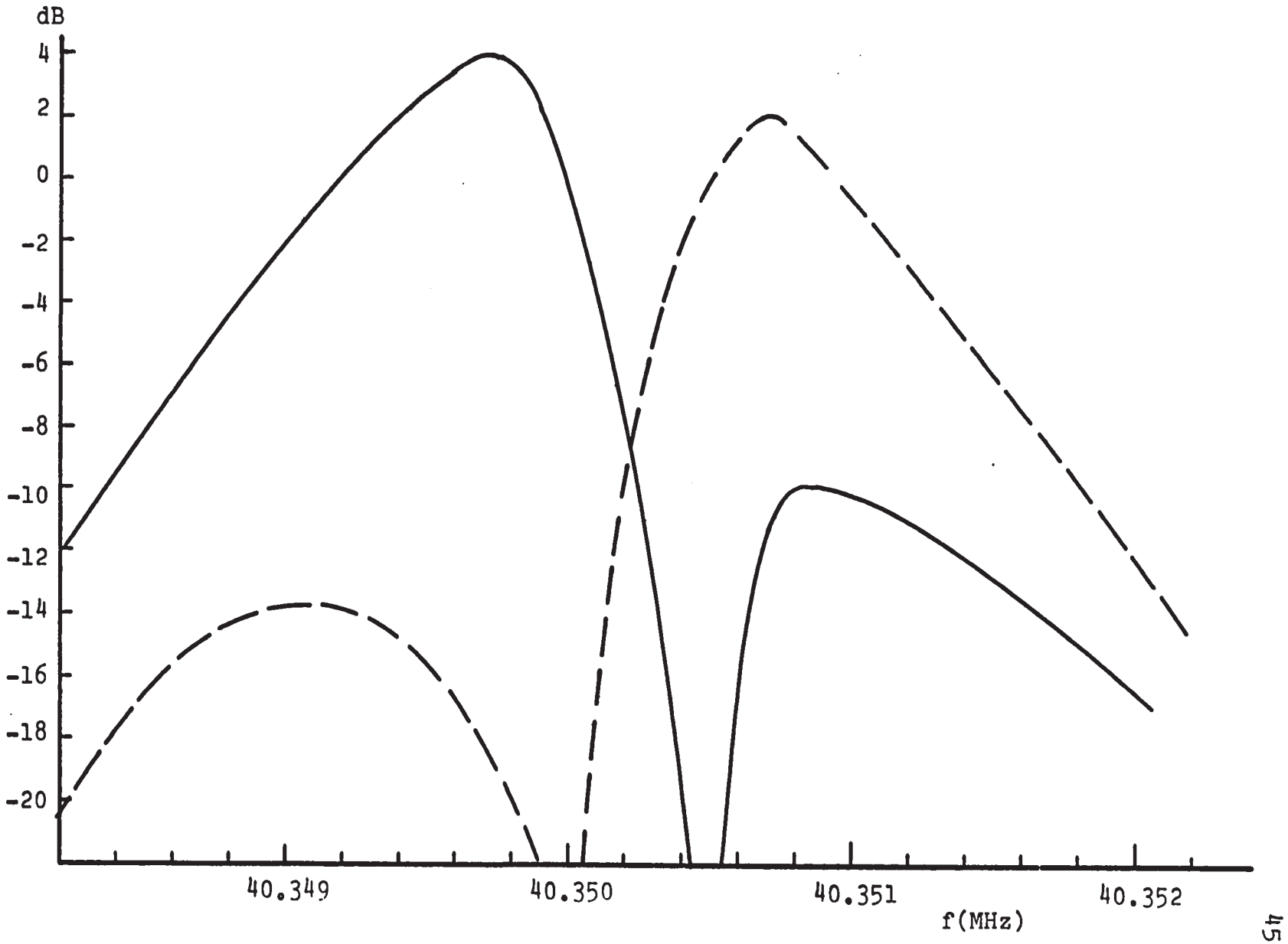

Fig. 15 Receiver frequency response

a rigorous determination, which is very complex, is not required; instead an approximate value is obtained by using the geometric mean of the pre- and post-detection bandwidths (Tiuri, 1964). Using these values in equation (4.1) leads to a noise power, $P_N \approx 3.0 \times 10^{-17}$ watts which is in fair agreement with the measured noise power of approximately $6 - 9 \times 10^{-17}$ watts. Typical echoes with S/N of 20 dB were used, thus requiring a received signal power of about 8×10^{-15} watts. Substituting this value in equation (2.4) leads to an electron line density of approximately 0.5×10^{14} m^{-1} which is about one half of the critical density. This suggests that underdense echoes are very unlikely to exceed a S/N of 26 dB which is corroborated by the observations.

4.2 Frequency Stability

The frequency stability of the system is the limiting factor (insofar as equipment is concerned) in the attainable accuracy of the wind velocity measurements. The required accuracy of 2 m/sec (Chapter 2) corresponds to a permissible error in frequency of approximately 0.5 Hz

(Appendix 3). It should be noted that this value applies to frequency shifts more than to absolute frequency errors which can be detected from long term wind results.

Periodic measurements prior to the experiment showed that after months of continuous operation, the transmitter and receiver oscillators stabilized sufficiently for the frequency drift not to exceed the above figure over periods of several days. As is shown in the subsequent discussion on the wind results, it was found that the absolute error in frequency probably did not exceed 2 Hz.

Figures 16, 17 and 18 show scatter diagrams for the wind speed observed through individual echoes during several days. The necessity of regular recalibrations of the receiving system and constant attendance of the chart recorder impeded a continuous monitoring of the winds.

The prevailing and tidal components of the wind velocity, computed by means of Fourier analysis using hourly wind averages within a 24 hour period between August 20 and 21, are shown in Fig. 19 where hourly wind averages obtained for other days are superimposed for comparison. A good correlation is evident between the experimental points and the semidiurnal sinusoid, in fact, the correlation coefficient between it and the

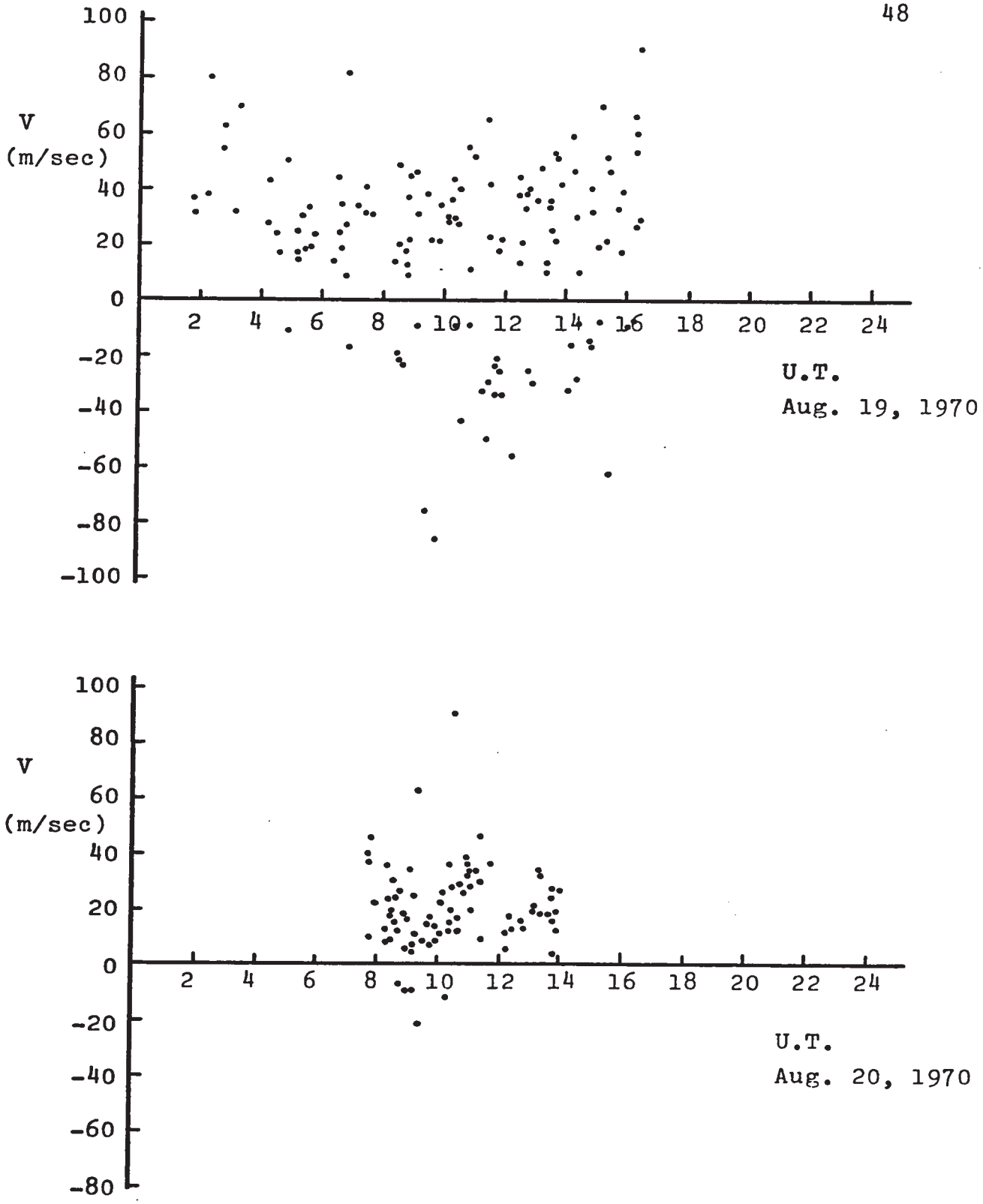

Fig. 16 Wind velocity scatter diagram

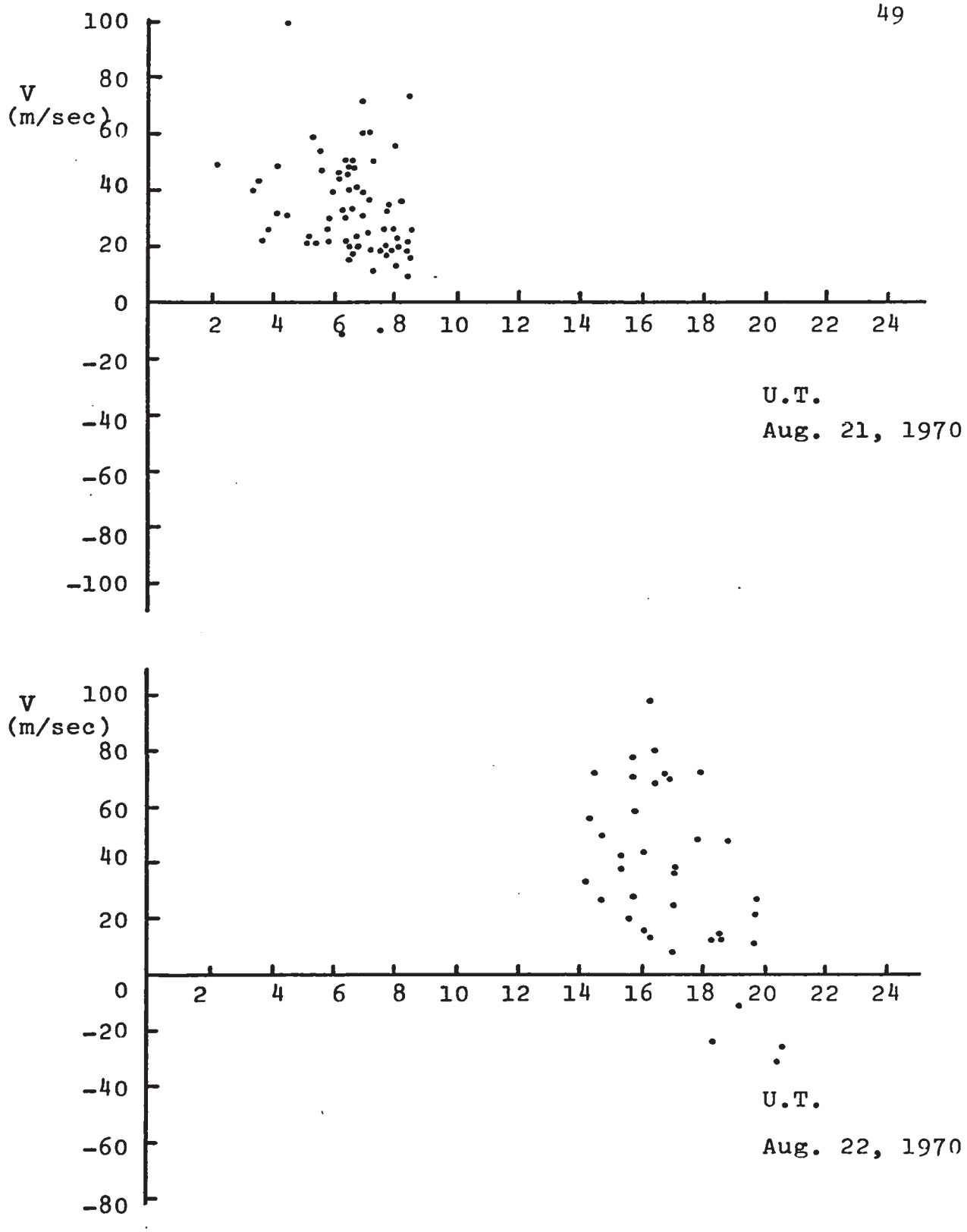

Fig. 17 Wind velocity scatter diagram

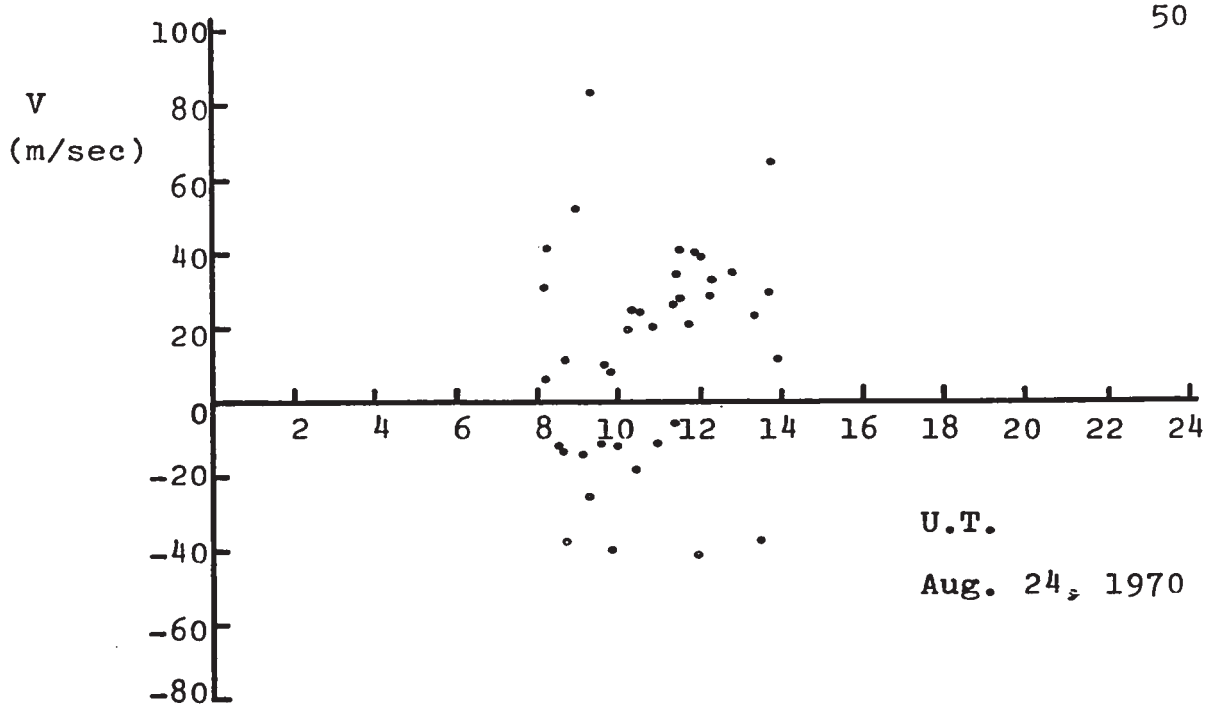

Fig. 18 Wind velocity scatter diagram

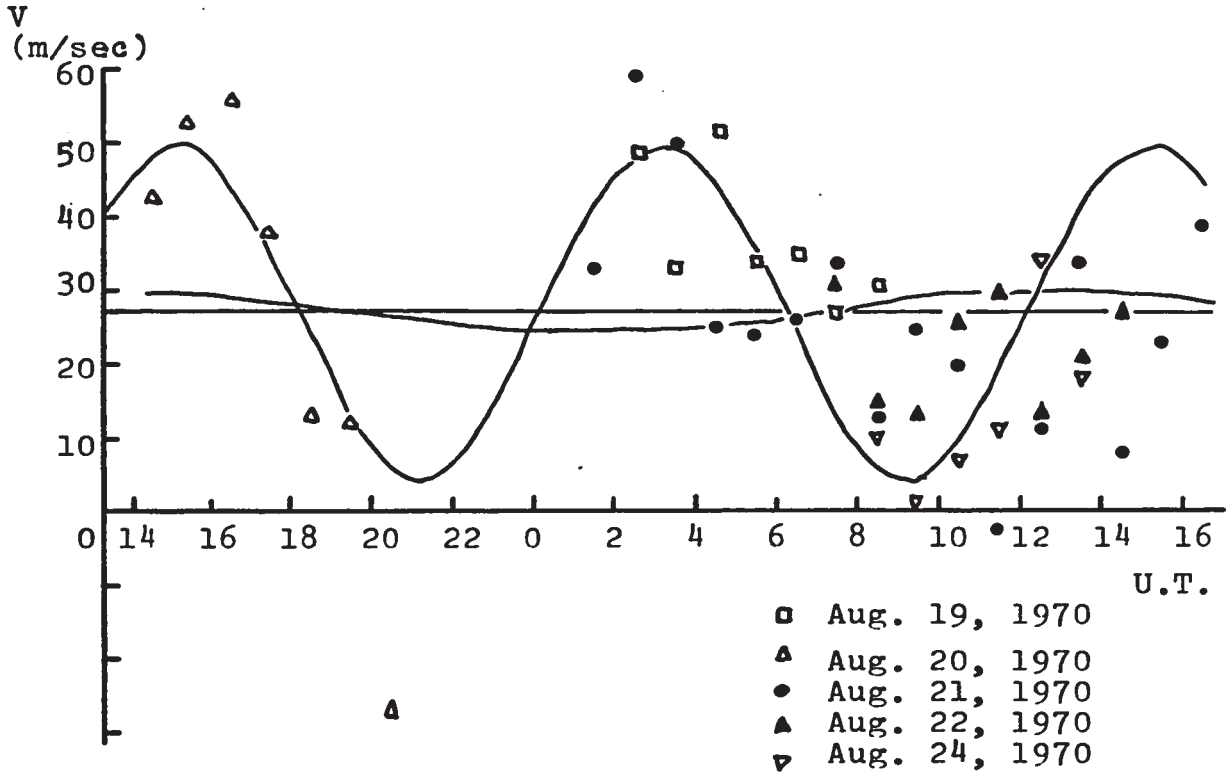

Fig. 19 Prevailing and tidal wind components

points used to compute it is 0.8 (Chapman and Bartels, 1940).

These results are in good agreement with those obtained at Jodrell Bank (53°N) by Greenhow and Neufeld (1955b, 1956), who for the month of August, report a prevailing wind directed toward the southeast of about 24 m/sec compared to 27 m/sec in these measurements. In addition, the semi diurnal component amplitude was approximately 25 m/sec as compared to 22.5 m/sec in the present work. The directions of the semidiurnal wind vector also agree; Greenhow and Neufeld's results indicate that the vector is directed at 150° azimuth (corresponding to the Ottawa-London scattering angle bisector) at 0915 and 2115 hours local time, whereas in this work the maximum positive winds, which occur when directed at 150° azimuth, were present at 1000 and 2200 L.T. The difference is small and it can partly be explained by assuming a latitude wind velocity distribution similar to that described by Kato (1956) for the dynamo region.

The agreement between the diurnal components is not as good; Greenhow and Neufeld obtained an amplitude of approximately 10 m/sec compared to 3 m/sec in this work. There is also a time difference of 11 hours in

the orientation of the diurnal wind vector; however as the observed data covered 270° of the diurnal cycle only, the result may not be reliable. More observations would provide more reliable results which might be in better agreement with other investigations.

In view of the generally good wind results it can be stated that the prototype system can be used to measure winds. Some fixed frequency displacement may have been present, but the results for the prevailing wind indicate that it is unlikely to exceed the Doppler shift equivalent to wind velocities of 8 - 10 m/sec.

4.3 Location of Reflection Point

The reflection point is located by determining its transmitter azimuth and the direction of arrival of the received signal (Appendix 3), the former being obtained from the theoretical amplitude ratio as a function of transmitter azimuth and the latter from the phase relationship of the signals arriving at the three receiving antenna arrays. Since the phase between the received signals is measured at the end of the receiving system, the physical difference between the various channels

introduce a constant differential phase shift on the output signals, thereby altering their absolute phase relationship. It is therefore necessary to determine the constant phase shift (phase constant) for both direction finding subsystems. The procedure to achieve this is explained in detail in Appendix 6.

A computer program was developed to calculate the position of the reflection point using the theory presented in Appendix 3; a detailed error analysis is given in Appendix 7. The histogram shown in Fig. 20 corresponds to the measurements whose height is physically possible when the errors are considered, leading to 352 solutions out of 418 echoes used. The unacceptable heights may be attributed to side lobe transmissions (mainly southern transmitting secondary lobes) which introduce an error in the assumed transmitter azimuth. This appears to be confirmed by an approximate calculation on the expected relative number of echoes due to side lobe propagation that leads to 5 - 5.5 main lobe solutions out of 6 observations.

The range of the side lobe echoes is sufficiently small to cause considerable ambiguities in the determination of the position of the reflection point due to ambiguities

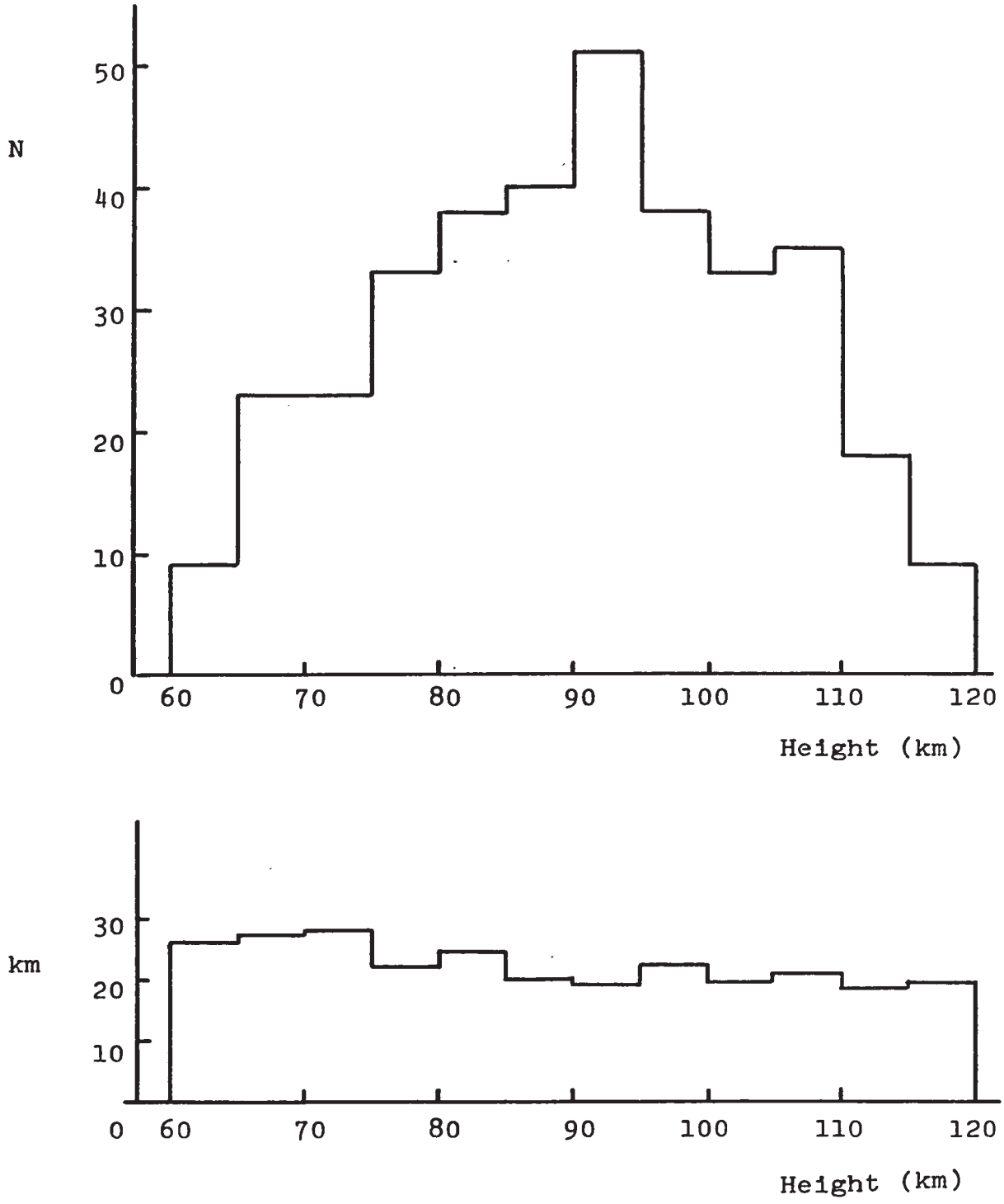

Fig. 20 Measured height distribution and associated approximate peak error (1.5 σ)

in θ_{EW} resulting from the observation of an azimuth range covering at least two complete revolutions in ψ_{EW}. The difficulty of resolving the ambiguities prevents the use of these solutions, however their small number makes their elimination unimportant and there is no reason to assume that they would provide notably different wind information from that obtained from the main lobe solutions. It is possible that the apparently main lobe propagation echoes are contaminated with side lobe ones, however it is not possible to identify them with the available evidence; in addition the relative number of main and side lobe echoes is such that a significant contamination is unlikely.

In order to confirm the ability of the system to determine reflection point heights, it is sufficient to make a comparison between the distribution of heights obtained for underdense meteors by triangulation and decay times. Figures 21 and 22 show the triangulated and diffusion heights respectively; the good agreement in the distribution shape and mode indicates that the system can determine heights even though the results have excessive errors that lead to the very large dispersion of the triangulated height distribution compared to that for diffusion heights, which resembles the true distribution

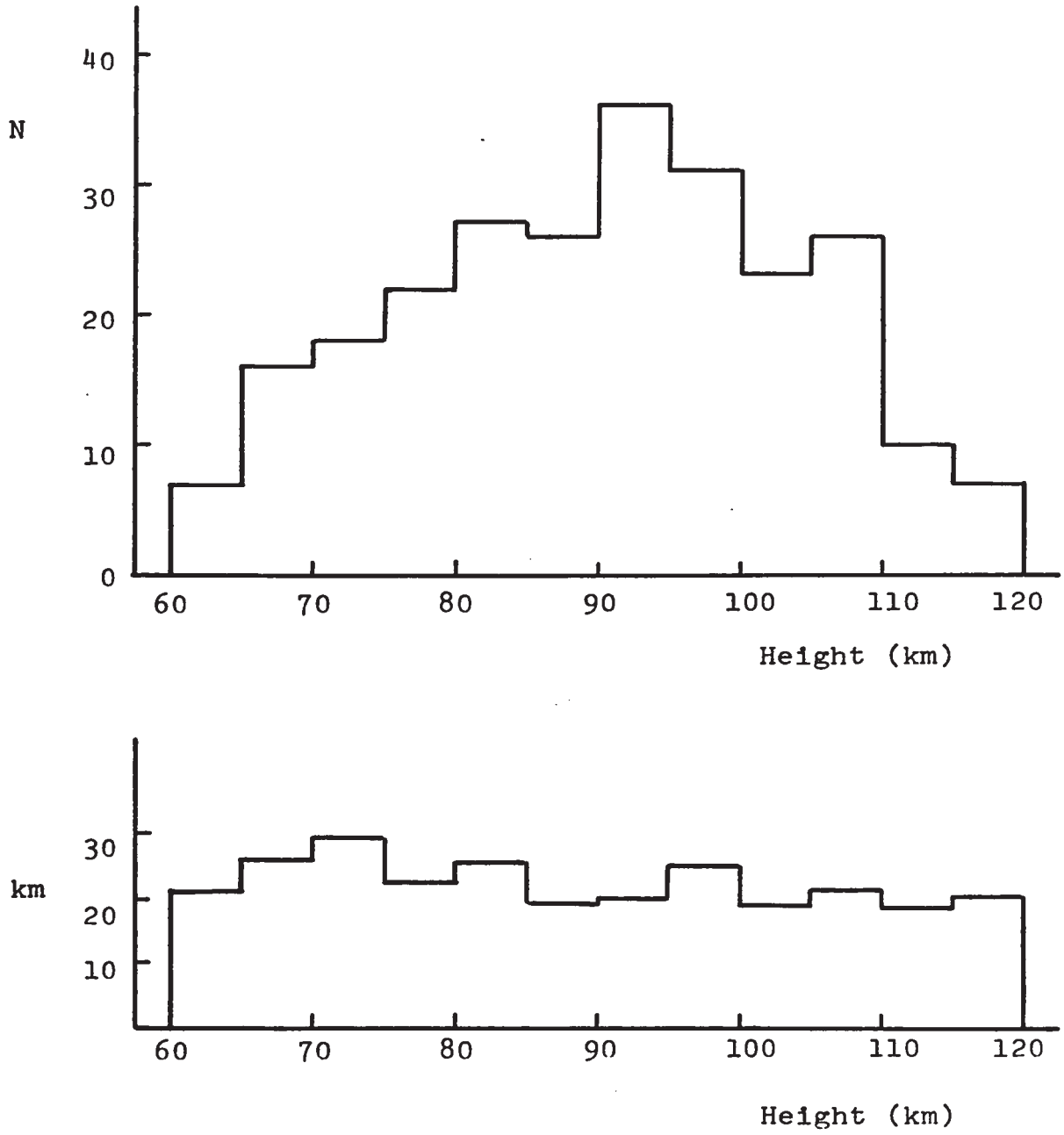

Fig. 21 Measured height distribution of underdense meteors and approximate peak errors (1.5 σ)

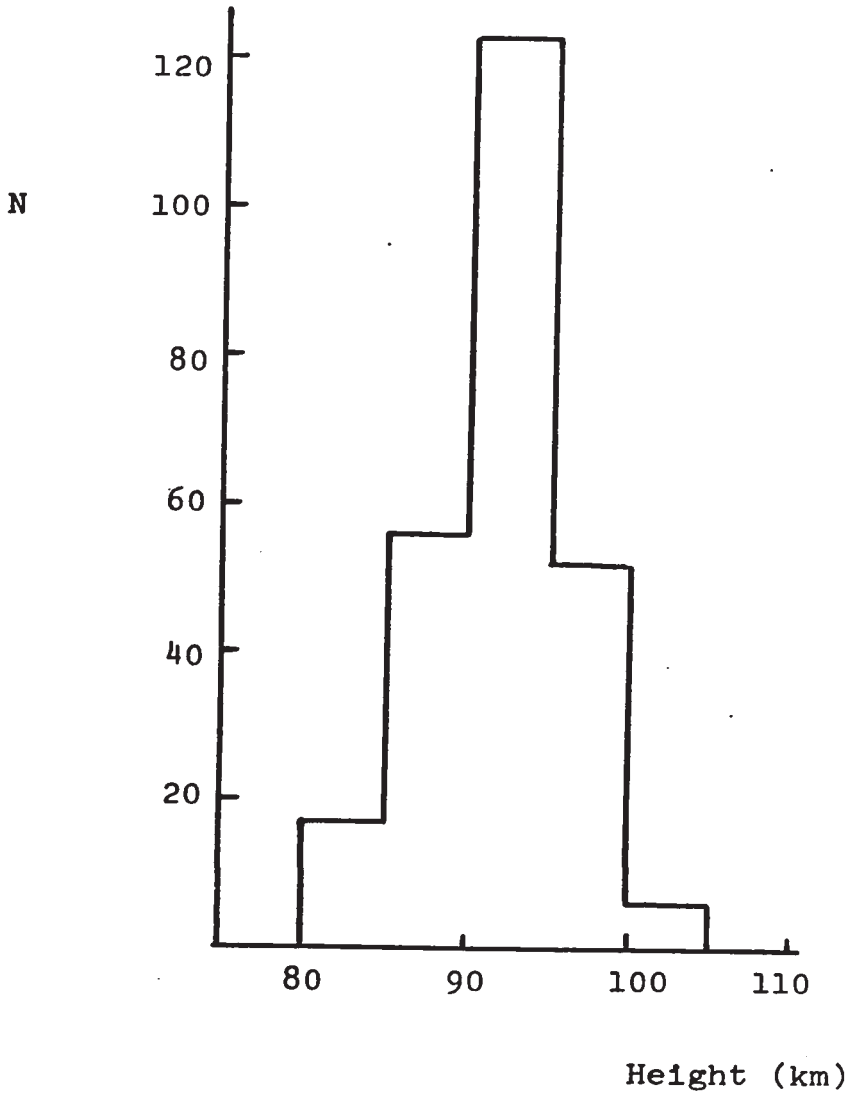

Fig. 22 Height distribution of underdense echoes obtained from decay times

more closely. Some truncation is present at the high end as a consequence of the bias in the selection process which favours longer echoes because of their better wind information content.

The correlation between the heights obtained through both methods is virtually zero, which is to be expected from the large errors associated with the height determinations. No strict selection was performed of echoes with nearly ideal exponential decay, and an important contamination of near critical meteors is probably present due to the relatively low system sensitivity. Under these conditions errors of about 5 km in the decay heights are possible, and these in conjunction with the much larger errors in the triangulated heights render a good correlation impossible.

In summary, the performance of the prototype model, while not being entirely satisfactory, confirms the feasibility of using an orthogonal forward scatter geometry for the measurement of winds in the meteor region.

CHAPTER 5

NEW SYSTEM PROPOSAL

5.1 General

The results obtained with the prototype model can be used as a basis for the determination of the design parameters of a definitive working system. It is desirable that such a system be automated and preferable that the data be handled in digital form to simplify its processing. The measurements are to be taken within 0.1 seconds after the formation of the trail to avoid distortions due to winds (Greenhow, 1952) and errors in height as a consequence of motions of the reflection point because of wind shears (Roper, 1966).

An overall design of a system that is expected to meet the specifications established in Chapter 2 is presented beginning with some necessary properties of the transmitted signal, followed by the determination of the parameters required for the location of the reflection

point. Subsequently the transmitter power needed for the observation of the necessary number of echoes per hour is found, and finally the Doppler measuring subsystem is obtained.

5.2 Frequency and Polarization of the Transmitted Signal

The frequency used in meteor radars is not very critical, in fact, the various systems listed in Table 2 cover a range of over one octave; higher frequencies are unattractive because of the associated increased scattering loss (equations 2.4 and 2.10). The disadvantages of lower frequencies are discussed by Peterson (1968), the most important being the presence of atmospheric noise which may hinder observations over prolonged periods. In the case of systems that require high directivity, the increase in the size of the antenna arrays is also a drawback. Operation around 40 MHz is fairly common and has proven to be quite satisfactory. This was confirmed by the operation of the prototype model which, with the exception of occasional unacceptable noise levels due to atmospheric electrical activity in the vicinity of the receiving station, did not show any problems associated

with the frequencies used. It should be noted that these frequencies are in the last instance determined by the available bands in today's crowded spectrum. In the present work frequencies of 40.350000 and 40.350500 MHz are used. The small separation between the signals is required in order to have nearly identical propagation paths at both frequencies, as well as by the need to process both signals with a common receiver for the amplitude ratio measurements.

A second scattering system with an additional two closely spaced frequencies is required to measure the second orthogonal component of the wind velocity. Economic considerations suggest the use of frequencies that can be processed by the same receivers as for the first system, therefore the difference between the extreme frequencies should be in the order of 2 - 3 kHz to fit into the bandpass of typical receivers. The four frequencies can be separated fairly easily after they have been converted to approximately 5 kHz.

The signal polarization to be used is determined by the electron scattering mechanism at the trail. An electron under the influence of an electromagnetic wave oscillates in the direction of the applied electric field

vector, its radiation pattern being like that of a dipole with axis parallel to the field; i.e., a closed toroid with maximum and zero radiation in directions perpendicular and parallel to the axis respectively. As the transmitted signal is scattered by electrons in the trail, it is clear that in an orthogonal scattering geometry the transmitted signal should be polarized in the vertical direction for most efficient operation. This has the added advantages of reducing ground reflections as well as diminishing the probability of plasma resonance at the trail since in most cases its direction tends to have a large vertical component.

5.3.1 Location of Reflection Point

By far the most difficult specification to meet is the required accuracy of $\pm$ 1 km in the determination of the reflection point height. The permissible error is due to inaccuracies in the direction finding and in the transmitter azimuth. For practical receiving antenna separations (in the order of 100 m) it can be shown that the former is approximately four times larger than the latter. Therefore errors of 0.8 and 0.2 km due to

inaccuracies in direction finding and transmitter azimuth respectively are specified.

5.3.2 Receiving Antenna Separations

It is clear that for a given signal-to-noise ratio the main parameters determining the direction finding accuracy are the antenna separations and the angle between the incoming signal and the antenna axes. Differentiating equation (3.1) we obtain

$$\frac{d\psi}{d\theta} = - \frac{2\pi d}{\lambda} \sin \theta \qquad (5.1)$$

Therefore for improved accuracy it is convenient to increase d and θ. In the E-W pair $\theta \simeq 90^{o}$ which is optimum and for the N-S pair it implies that echoes with high elevation angles are desirable. However, this has the following drawbacks:

(a) Winds are essentially horizontal, therefore the wind component parallel to the scattering angle bisector would be reduced, with the consequent decrease in

wind speed accuracy.

(b) The observation at high elevation angles requires trails with larger zenith angles. As these trails are not as numerous as are those with smaller angles, the increase in accuracy would also be accompanied by a decrease in the observation rate.

To avoid the necessity of excessively large antenna separations, the observations are limited to a minimum elevation angle of 12.5° which defines the maximum observable range at about 320 km (Fig. 23). The measured height of echoes originating at longer distances have more error due to the increased range as well as lower elevations. An observed volume 70 km deep is chosen as a convenient size to be obtained with reasonable transmitter radiation patterns, resulting in a minimum range of 250 km where the maximum elevation angle is approximately 22 degrees. It should be noted that the observed elevation angles are near the pseudo-Brewster angle for a typical ground, thus reducing the effect of ground reflections (Appendix 2).

The maximum error in height due to elevation errors occurs at the largest range, i.e. 320 km where a change of 0.8 km in height corresponds to 0.13° change in elevation.

Fig. 23 Maximum and minimum elevation of reflection point as a function of range

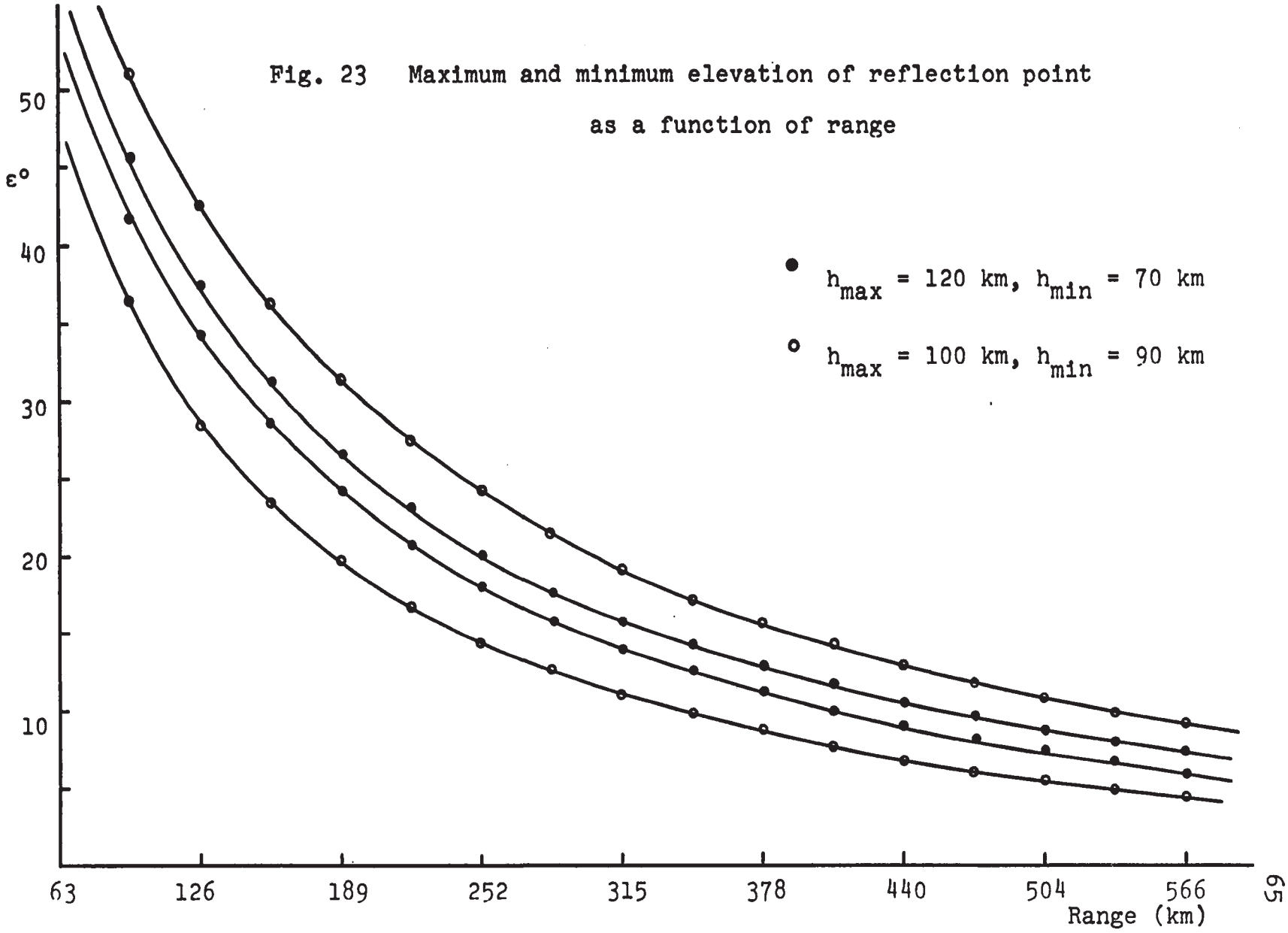

The error in elevation is the result of errors in both θ_{NS} and θ_{EW}.

$$d\varepsilon = \frac{\partial \varepsilon}{\partial \theta_{NS}} d\theta_{NS} + \frac{\partial \varepsilon}{\partial \theta_{EW}} d\theta_{EW}$$

Inspection of the geometry associated with the direction finding leads to the approximate expression

$$\Delta\varepsilon = \frac{\Delta\theta_{NS}}{\sin\eta} + \frac{\Delta\theta_{EW}}{\tan\eta} \qquad (5.2)$$

where

η = angle between the two direction cones at their intersection.

Therefore the maximum error in elevation for a given $\Delta\theta_{NS}$ and $\Delta\theta_{EW}$ occurs at the edges of the observed volume as seen from the receiving station. Assuming a maximum azimuth range of $\pm 10^{o}$ to obtain a volume width of approximately 70 km, the value of η at the edges is about 45^{o}.

Inasmuch as θ_{NS} and θ_{EW} are obtained from the phase differences ψ_{NS} and ψ_{EW} between the signals arriving at the

$$\frac{\sigma}{S} = \frac{1}{\sqrt{1000}} = 0.032 \text{ rad} = 1.8^{o}$$

and the total RMS error due to both signals is

$$\Delta\psi = \sqrt{1.8^2 + 1.8^2} = 2.6^{o}$$

Allowing 0.4^{o} for errors due to quantization, system limitations, etc. the final value for the acceptable error in the phase measurements becomes

$$\Delta\psi = 3.0^{o}$$

Also, from equation (3.1)

$$\psi = \frac{2\pi d}{\lambda} \cos\theta$$

and

$$\psi - \Delta\psi = \frac{2\pi d}{\lambda} \cos(\theta + \Delta\theta)$$

eliminating ψ it is found that

$$d = \frac{\Delta\psi^{o} \cdot \lambda}{360} \quad \frac{1}{\cos\theta - \cos(\theta + \Delta\theta)} \qquad (5.3)$$

The values of $\Delta\theta$ are obtained from (5.2) where in order to obtain similar separations for both pairs, the following restrictions are imposed

$$\frac{\Delta\theta_{NS}}{\sin\eta} = 0.75\ \Delta\varepsilon$$

$$\frac{\Delta\theta_{EW}}{\tan\eta} = 0.25\ \Delta\varepsilon$$

Substituting the appropriate values in (5.3) leads to the antenna separations for both direction finding systems

$$d_{NS} = 150\ \text{m}$$

$$d_{EW} = 115\ \text{m}$$

both of which are reasonable.

A simple calculation shows that there is no possibility of ambiguities in θ_{NS} due to multirevolution measurements of ψ_{NS}. This is not the case however for the E-W pair where ambiguities are certain. It is

therefore necessary to resolve this ambiguity and it appears that the best method is by using a second E-W direction finding antenna pair with much smaller separation not simply related to 115 m so that a given pair of ψ_{EW} corresponds to one value of θ_{EW} only.

The results obtained with the prototype model show that most echoes having ψ within 10 - 20 ^{o} from 0 or 360^{o} cannot be used because of the very noisy phasemeter outputs. This is an inherent property of instruments that operate on the principle of comparing the zero crossings of two signals, and assuming a uniform phase distribution, approximately 10% of the echoes are lost, which would be reduced by using signals with higher S/N. Nevertheless if a maximum number of echoes are to be used, it is recommended to employ two phasemeters for the measurement of each phase difference as shown in Fig. 24, in which case always one of the units will read between 90 and 270° which corresponds to the region of better phasemeter performance. A simple logic circuit can be used to select and identify the appropriate output.

The outputs from the phasemeters are pulse trains with PRF equal to the frequency of the signals being compared, and duty cycle proportional to the phase differ-

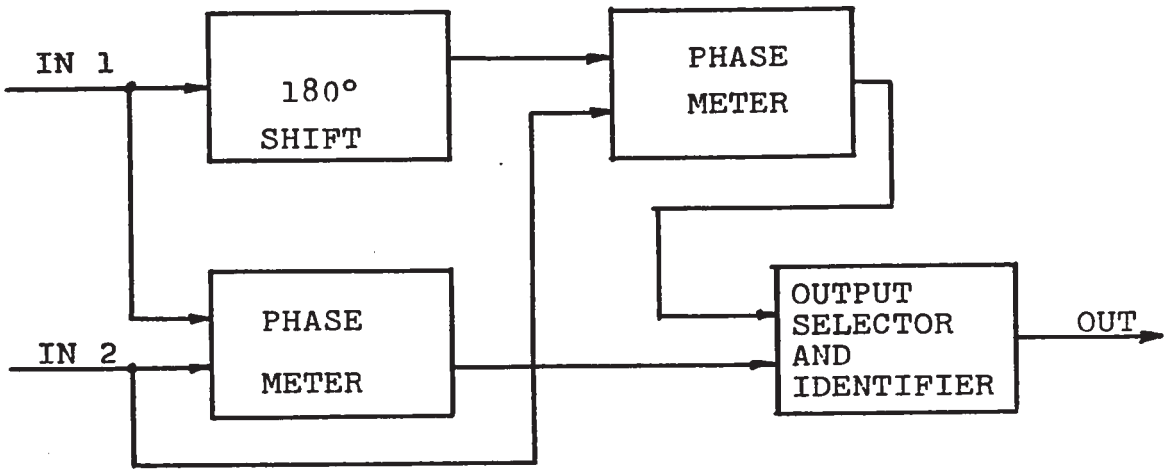

Fig. 24 Proposed phase measuring subsystem

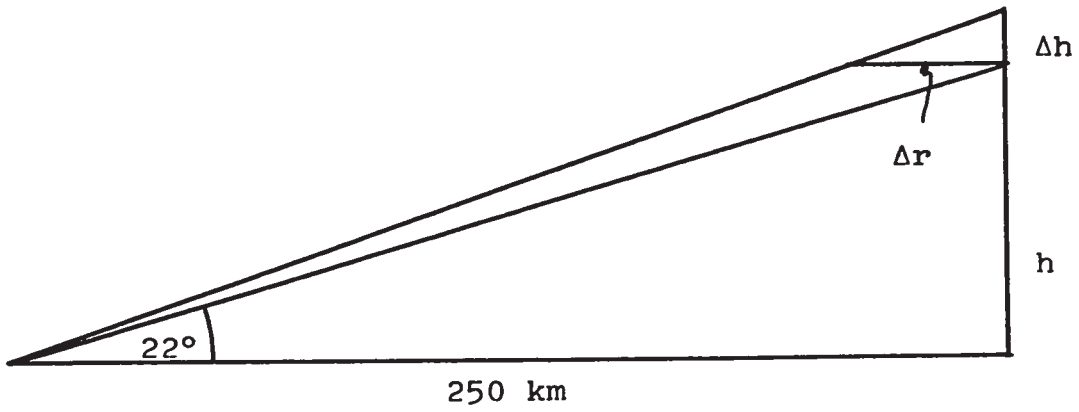

Fig. 25 Effect of range error on height determination

ence between the input signals. Therefore the average value of the output (DC component) is also proportional to the phase difference. The nature of the phasemeter outputs suggests a direct digital processing, but in view of the possible 0.6% variation in the PRF due to Doppler shift it is not possible to obtain the desired accuracy of 0.4° by simply determining the duration of the pulses with a clock and gated counter. Therefore it is also necessary to know the PRF which is available from the wind information. Alternatively, the duration of the ON and OFF sections of the output waveform can be measured by the same method and their ratio, which is only a function of the phase difference, determined by a ratio counter or in the subsequent processing. The clock frequency that drives the gated counter is obtained on the basis of the desired accuracy of 0.4° which requires each period to be divided in about 1000 intervals. Assuming the PRF to be similar to that in the prototype model, a clock frequency of 4.5 MHz would be required. It is advisable to perform several phase measurements for each echo so that fast changing phases indicating some anomaly can be detected.

5.3.3 Transmitting Antennas Radiation Patterns and Divergence Angle

The maximum allowable height error due to inaccuracy in the transmitter azimuth determination is $\pm$ 0.2 km (section 5.3.1). In a worst case design this error must not be exceeded at a point with longest transmitter and shortest receiving range, i.e. 320 and 250 km respectively. Under these circumstances the elevation of the incoming signal is 22° and the change in height due to an increment in range resulting from transmitter azimuth errors is (Fig. 25)

$$\frac{\Delta h}{\Delta r} = \tan 22° = 0.405$$

Therefore

$$\Delta r = \frac{0.2}{0.405} = 0.5 \text{ km}$$

and the permissible error in transmitter azimuth is

$$\Delta\delta \simeq \frac{0.5}{320} = 0.09°$$

Assuming the S/N to be 30 dB (section 5.3.2) the amplitude error is

$$\Delta A = \pm \frac{S+N}{S} = 10 \log \frac{1001}{1000} = 0.043 \text{ dB}$$

Allowing 0.05 dB to include all errors not due to noise, the RMS error in the amplitude ratio becomes

$$\Delta R = \sqrt{0.09^2 + 0.09^2} = 0.13 \text{ dB}$$

Therefore the necessary variation of amplitude ratio as a function of transmitter azimuth is

$$\frac{dR}{d\delta} = \frac{0.13 \text{ dB}}{0.09^\circ} = 1.4 \text{ dB/}^\circ$$

This is not difficult to obtain; as an example which has no side lobe problems, two arrays consisting of 14 elements (monopoles) separated by one half wavelength and with a binomial amplitude distribution is suggested. The radiation pattern of one of such array is shown in Fig. 26 and the amplitude ratio as a function of transmitter azimuth for two beams with a divergence angle equal to one beamwidth is depicted in Fig. 27 where it is shown that the required slope is obtained. As accuracy considerations dictate that echoes with ranges

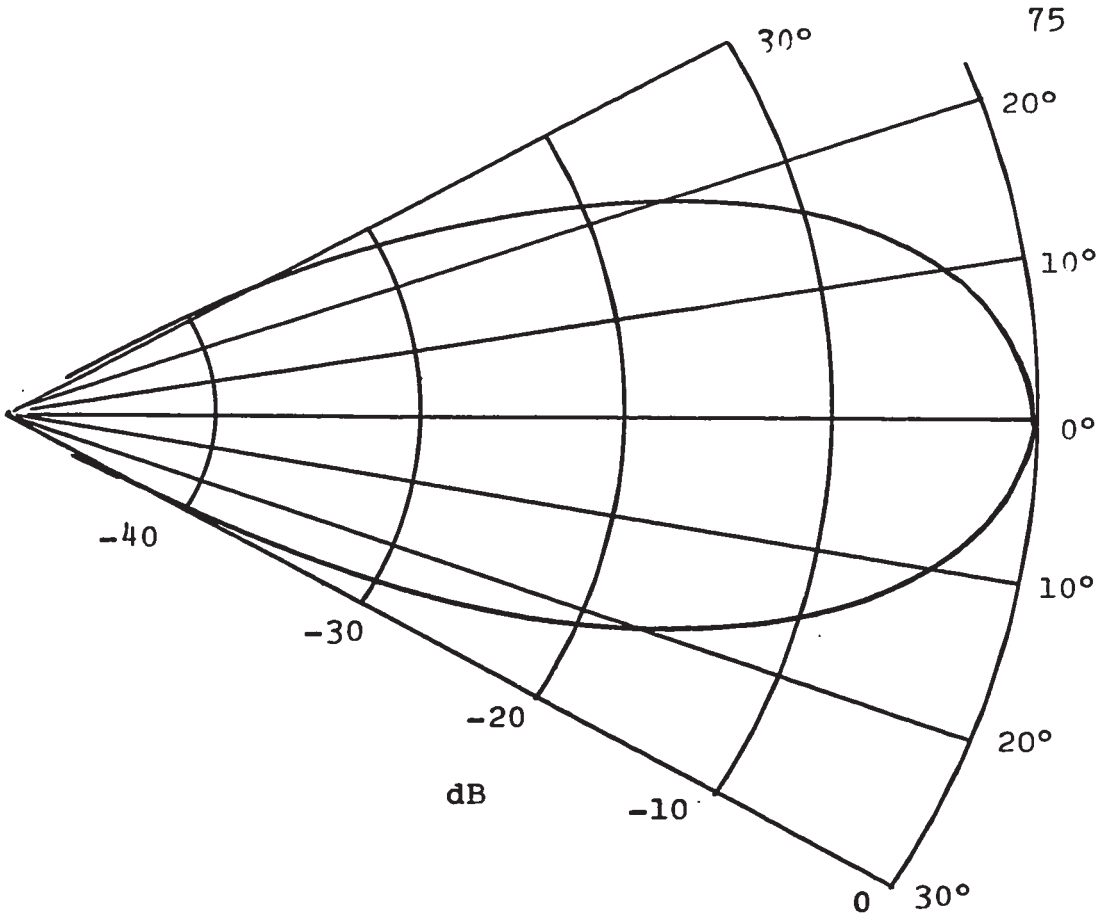

Fig. 26 Radiation pattern of proposed antenna arrays (see text)

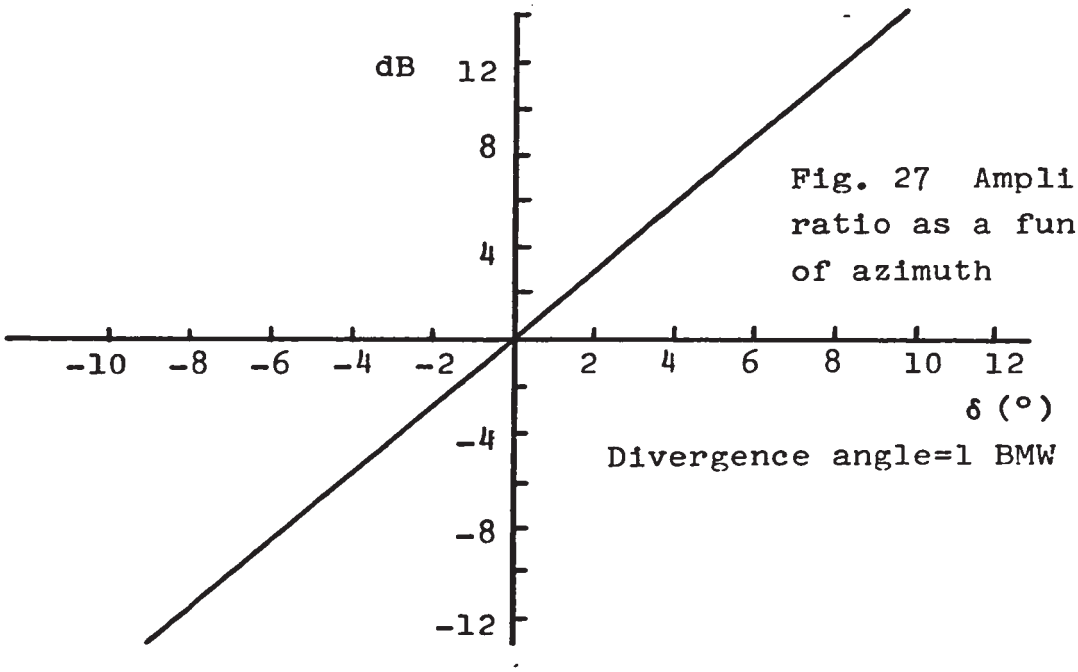

Fig. 27 Amplitude ratio as a function of azimuth

below 250 km or above 320 km not be used (section 5.3.2), it is necessary to restrict attention only to those echoes with amplitude ratios between ± 10 dB.

The relative amplitudes of the two signals used in the amplitude ratio measurement must be accurately preserved. This may be accomplished by using a linear receiver common to both signals thus avoiding errors due to non linearity and changes in receiver gain. After separation of the two frequencies by means of filters, the signals may be processed by precision logarithmic converters whose outputs are proportional to signal strength in decibels, a convenient feature when large dynamic ranges are used. The logarithmic converter outputs may then be applied to a differential amplifier which provides the amplitude ratio in dB to an analogue to digital converter. The individual amplitudes may also be recorded if desired.

5.4.1 Necessary Observation Rate

The necessary number of useful echoes per hour is determined by the desired spatial and temporal wind

resolution, which in turn is a function of the wind properties. As stated in Chapter 2, the irregular wind component imposes the most stringent requirements on the measuring system, therefore its characteristics are used to establish the required observation rate.

The irregular winds are very anisotropic, with horizontal and vertical correlation lengths of approximately 150 and 6 km respectively (Chapter 2); consequently the vertical wind sampling must be much finer than the horizontal. It is thus necessary to divide the volume under observation in compartments of sizes suitable to provide the required sampling and impose the condition that at least one meteor be observed inside each compartment within a period defined by the temporal wind autocorrelation function which leads to approximately one hour (Chapter 2). The sides of the volume under observation have been defined as 70 km long (sections 5.2.2 and 5.2.3), which is substantially smaller than the horizontal correlation length, therefore it does not appear to be necessary to compartamentalize the volume horizontally. Along the vertical direction the division is essential due to the much shorter vertical correlation length. The thickness of the slices is limited by the accuracy in

the height measurements which leads to the selection of 2 km corresponding to approximately twice the length of the vertical component of the principal Fresnel zone. The necessary number of slices is defined by the meteor height distribution, assumed to be approximately Gaussian. The mode of the distribution is arbitrarily set at 93 km and the standard deviation, on the basis of Kaiser's results (1954), at 1.3 scale heights corresponding to approximately 8 km. For this distribution, ten slices covering 20 km and centered at 93 km would account for 80% of all meteors. If a trail is produced, the probability of its maximum ionization point being at any level is shown in Fig. 28. Since an enormous number of meteors would be required to have near certainty of observing at least one echo per compartment per hour, a 90% probability is selected for this event to occur. The average number of echoes per hour required to obtain the desired probability is computed as follows

$$P = 1 - (1 - p)^n$$

where

P = probability of at least one meteor being produced at a given level provided a trail is created

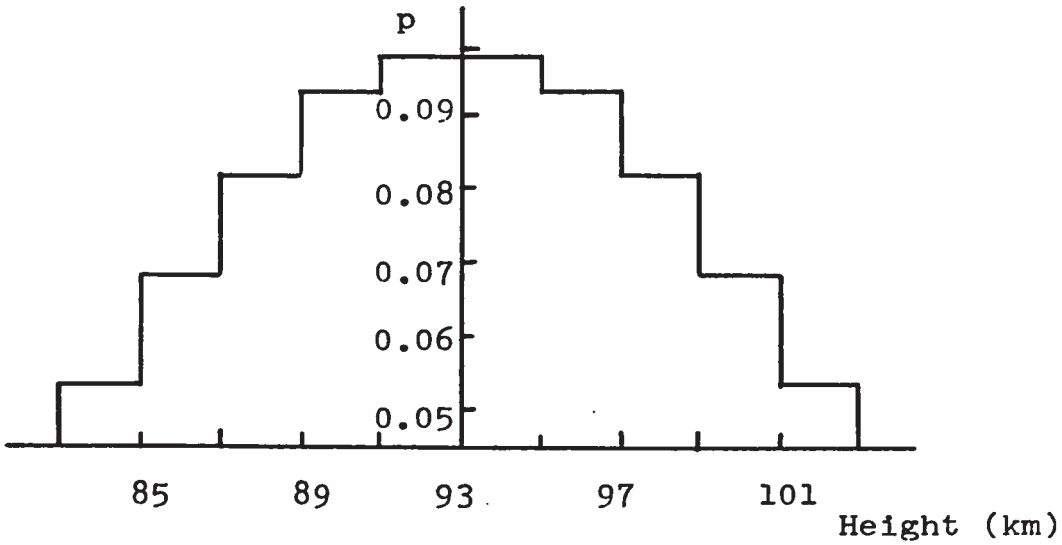

Fig. 28 Probability of one meteor occupying given level (provided a meteor is produced)

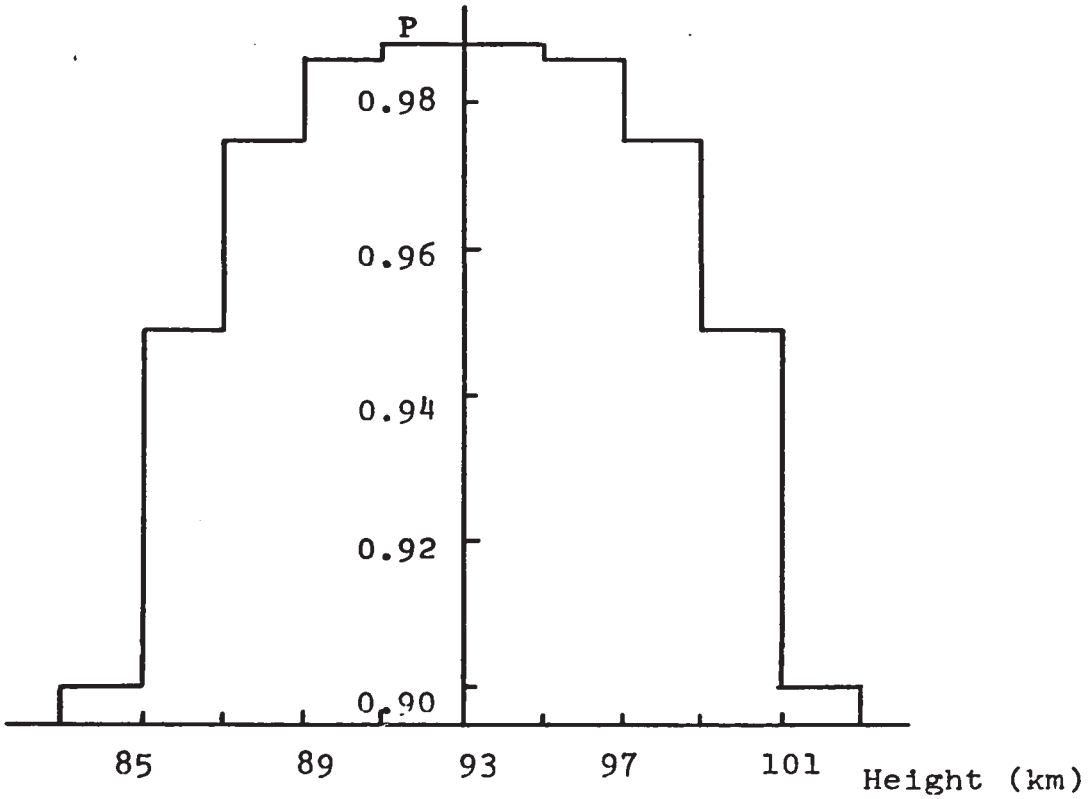

Fig. 29 Probability of at least 1 meteor (out of 42) occupying given level

p = probability of a meteor being produced at a given level provided a trail is created

n = total number of meteors produced.

By letting P = 0.9 and using the values of p shown in Fig. 28 we obtain n = 42. Fig. 29 shows the value of P at the various levels for n = 42.

Summarizing, the volume to be observed is 70 x 70 x 20 km and approximately 40 echoes with signal-to-noise ratio exceeding 30 dB are required per hour.

5.4.2 Transmitter Power

The observation rate obtained with the prototype model serves as a basis for the determination of the required transmitter power, which as will be shown, is the main parameter that determines the number of echoes observed per hour. Since the geometry of the proposed system is nearly equal to that of the prototype, the geometrical parameters influencing the rate of observation need not be taken into consideration.

The peak received power is approximately given by equation (2.5) which after lumping the geometrical

parameters into a constant becomes,

$$P_R = K \times P_T \times G_T \times G_R \times q^2 \qquad (5.3)$$

and the amplitude of the received signal

$$A = \sqrt{KP_TG_TG_R}\ q \qquad (5.4)$$

The gain of the antennas can be approximated by 41250/ab (Kraus, 1950) where a and b are the E and H plane beamwidths respectively. Substituting these values for the prototype and proposed antennas it is found that both have substantially the same gains, therefore it is unnecessary to consider them further and the transmitted power becomes the chief factor in the change in the received power for a given trail.

The prototype model is able to observe about four echoes exceeding 20 dB S/N per hour during low activity periods; this number can be increased by a factor of approximately four by improving the data processing so that no echoes are lost due to incomplete Doppler information or noisy phase data. The latter case was discussed in section 5.3.2 and the former is mentioned in section 5.5.

Therefore by improving the data processing, approximately 16 echoes with S/N of 20 dB would be observed. This figure can be improved further by reducing the receiver bandwidth and increasing the transmitted power.

It is found in section 4.1 that the equivalent noise bandwidth of the receiver was approximately 360 Hz. The peak Doppler shift of less than 30 Hz permits the reduction of the bandwidth by a factor of six which in conjunction with a 70% increase in the transmitted power results in an improvement of 10 dB in the received S/N. Therefore by increasing the transmitted power to 30 watts (18 watts in the prototype) and using a receiver bandwidth of 60 Hz, it would be possible to observe 16 echoes per hour with S/N of 30 dB. To obtain the power required to observe 40 echoes per hour, it is necessary to find the dependency of the number of echoes exceeding an arbitrary amplitude on the transmitted power. The following disgression is necessary to establish such a relationship.

The number of sporadic meteoroids with mass exceeding an arbitrary mass m_o is (Browne et al, 1956)

$$N \propto (m_o)^{-1}$$

From (2.1) and (2.2)

$$N \propto (q_o)^{-1} \tag{5.5}$$

where

q_o = arbitrary electron line density.

Also from (5.4)

$$q \propto \frac{A}{\sqrt{P_T}}$$

and substituting in (5.5)

$$N \propto \frac{\sqrt{P_T}}{A_o}$$

which states that the number of echoes exceeding an arbitrary amplitude A_o is proportional to the square root of the transmitted power and it follows that

$$\frac{N_1}{N_2} = \frac{\sqrt{P_{T_1}}}{\sqrt{P_{T_2}}}$$

leading to a necessary transmitted power of 190 watts.

5.5 Wind Measuring Subsystem

Many echoes with durations comparable to the Doppler period could not be used because of insufficient wind information; obviously higher echoes (with shorter durations) in the presence of slow winds are more affected by this limitation in the system, resulting in a bias against them in the selection of useful echoes. In addition when very fast Doppler frequencies were present it was impossible to determine the phase relationship between the outputs of the lock-in amplifier which define the Doppler sense and consequently some echoes had to be discarded.

To overcome the limitations inherent in the Doppler measuring subsystem of the prototype model, a digital displaced method is proposed for the new system (Fig. 30). A reference frequency (f_o) is used to measure the time required by two complete Doppler cycles by means of a gated counter. In order to have at least two cycles within the 0.1 second observation time, a minimum Doppler frequency of 20 Hz is required. Assuming

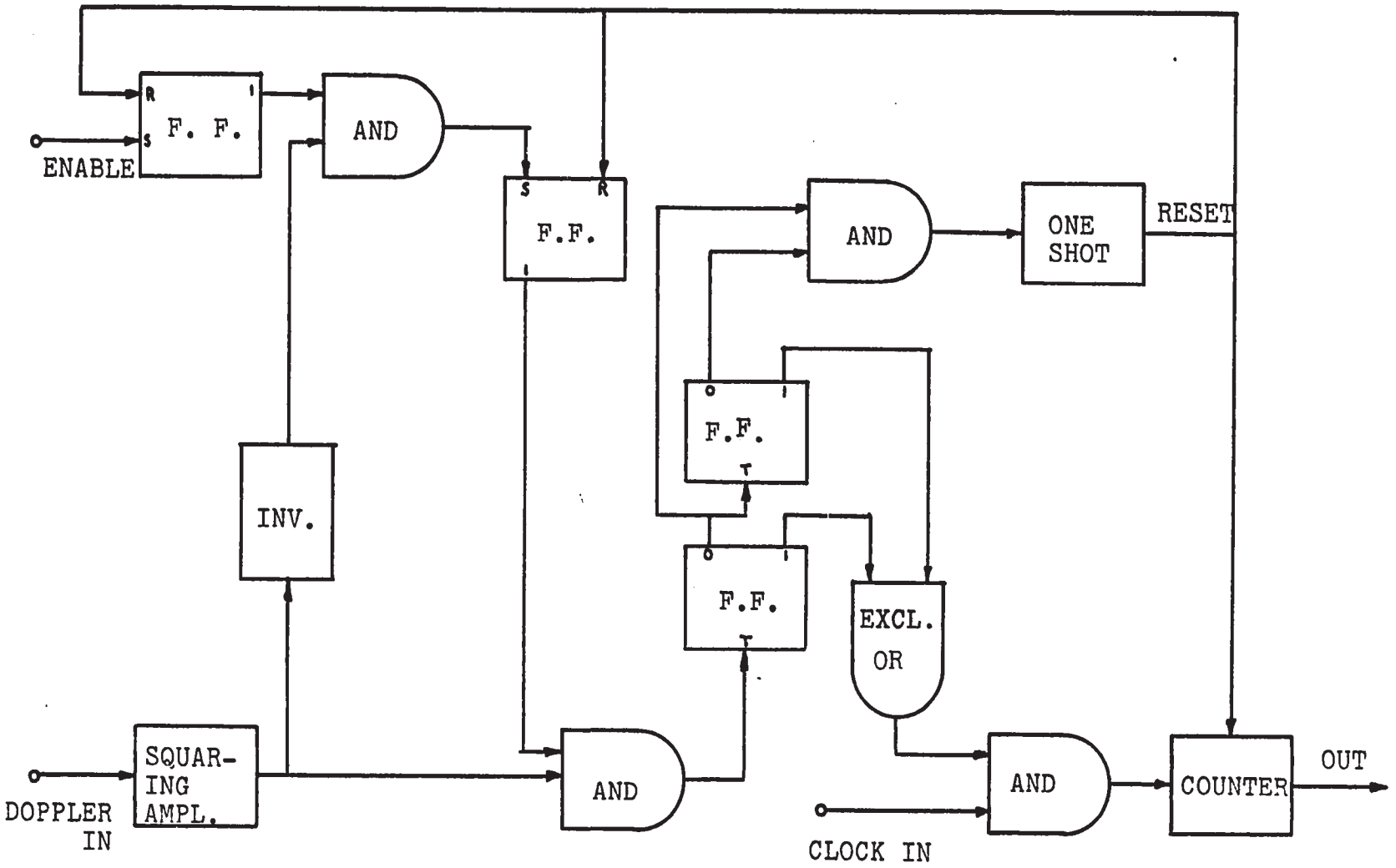

Fig. 30 Proposed Doppler Measuring Subsystem

maximum wind speeds of 150 m/sec with associated frequency shifts of 30 Hz leads to the selection of a displacement of 50 Hz which results in a maximum Doppler frequency of 80 Hz. Under these circumstances the times required for two cycles are

$$T_{max} = 0.1 \text{ sec}$$

$$T_{min} = 0.025 \text{ sec.}$$

Letting the reference frequency produce 250 counts in 0.1 sec leads to $f_o = 2500$ Hz. An eight bit system with 256 quantization levels appears to be adequate although the following check on the attainable resolution is necessary.

In T_{min} there are $0.025 \times 2500 = 63$ counts, therefore the quantization errors correspond to

$$\frac{150 \text{ m/sec} - (-150 \text{ m/sec})}{250 - 63} = 1.6 \text{ m/sec}$$

which is acceptable on the basis of the considerations presented in Chapter 2.

5.6 Summary

The results obtained with a prototype model based on an orthogonal forward scatter geometry show the feasibility of such configuration for the measurement of wind velocity in the meteor region (Chapter 4). Appropriate modifications are proposed and a definitive working model of a system that will meet the necessary specifications has been presented (Chapter 5). Such a system is characterized by its simplicity and economy, making it suitable for routine measurement of winds in the meteor region.

APPENDIX 1

EVALUATION OF EXISTING RADIO METEOR WIND SYSTEMS

A thorough evaluation of the various radio meteor systems now available is beyond the scope of this work. However their most relevant features are briefly mentioned; the reader is referred to the original sources for further details.

Since all systems fall broadly within two categories in regards to transmission method and scattering geometries, their main characteristics are listed so they can be used as a frame of reference in the subsequent evaluation of the different systems.

A. Transmission method

(i) Pulsed

Advantages:

- Accurate ranging
- Convenient for back scatter systems where transmitter is not isolated from receiver

(use receiver muting)

- Enables back scatter stations to eliminate unwanted echoes e.g. from airplanes, by using range thresholds.

Disadvantages:

- More complex transmitter
- High range resolution demands the generation of a large number of harmonics which can interfere with adjacent equipment and communications at other frequencies, a likely event in view of the crowding in the electromagnetic spectrum
- Requires large receiver bandwidths for good range resolution, thereby reducing the signal-to-noise ratio.

(ii) Continuous wave

Advantages:

- Narrow band transmission and reception
- Improves the signal-to-noise ratio
- Simpler transmitters
- Permits the observation of the echo amplitude fine structure.

Disadvantages:

- Cannot be used in monostatic systems
- Requires isolation precautions in closely spaced multistatic systems
- Susceptible to spurious reflections in back scatter system.

B. Scattering geometry

(i) Back scatter

Advantages:

- The proximity between transmitter and receiver permits easy access to the transmitted frequency which is required to determine the Doppler shift of the received signal
- Maintenance of equipment is simplified by the proximity of transmitter and receiver
- Allows relatively easy location of reflecting point.

Disadvantages:

- Produces highest signal scattering loss and shortest echo duration
- It may be subject to spurious reflections from

flying objects

- Two ways of obtaining two wind components are possible:

  i) Meteors at two different azimuths are observed, thus obtaining two radial components (Robertson et al, 1953; Greenhow and Neufeld, 1960). This method is inadequate because in order to obtain two distinct components, the volumes under observation must be separated by an undesirably great distance.

  ii) Two widely separated backscatter systems can be used to observe the same volume. The disadvantage of this method is basically economic since two complete systems are required.

(ii) Forward scatter

Advantages:

- Smaller scattering signal loss with the associated rise in underdense echo ceiling
- Longer echo durations
- Permits the use of CW transmissions
- Two transmitting and one receiving station are required for two wind components measurements,

however the very simple CW transmitting stations are economical and require little maintenance, thus partially nullifying the objections to a multistatic system.

Disadvantages:

- In the absence of direct links between widely separated installations, which is generally impractical, the detection of the extremely small Doppler shift requires highly stable transmitter and receiver oscillators. Such units have become available at reasonable cost, thus minimizing the objections to their use.
- Location of scattering point is more complex than in the backscatter case.

Following is a brief description of some of the current meteor wind systems which should be viewed in terms of the features described above and the accuracies determined in Chapter 2. The height accuracies shown below are generally poorer than those claimed by the sources quoted. They are obtained from Barnes (1969) and probably represent revisions over previous estimates.

1. The Adelaide system. (Robertson et al, 1953; Elford, 1968)

This multistatic backscatter system consists of one transmitting and four receiving stations, whose small separation makes it essentially a single wind component system; it is, however, suitable to measure wind shears through the observation of the trail motion at the points that satisfy the condition of specularity for the various transmission paths.

Ranging is obtained with a pulse system and the Doppler shift is derived from a CW signal at a different frequency. The sense of the Doppler shift is determined by phase modulating the CW transmission.

The direction of arrival is determined from the phase relationship between the Doppler signals obtained by mixing the direct and sky waves at several antennas. This is a drawback of the system, since for accurate direction finding it is necessary to have at least two complete Doppler cycles, which in a non displaced Doppler case imposes a considerable restriction on the number of usable echoes.

Accuracy:

Range: 2 km

Direction of arrival: 1 degree

Height: 2 km

2. The Stanford System. (Peterson and Nowak, 1968)

This is a rather unusual system designed to operate under adverse conditions including noise and spurious reflections. It uses a monostatic radar that transmits 28 bit random phase coded pulses, each bit being 10 microseconds long. A good range resolution is obtained by matching the transmitted with the received pulse.

The elevation angle of the reflection point is obtained from the amplitude ratio between the signals received at two antennas with different vertical radiation patterns. This method has since drawn some criticism (Frost et al, 1970). The azimuth of the received signal is not determined, which rules out this system because of insufficient spatial accuracy. The wind is measured with a 40 Hz displaced Doppler by

alternately observing two volumes separated in azimuth by approximately 90 degrees with the consequent loss of correlation between the winds in the two volumes under observation.

Accuracy:

Range: 0.75 km

Height: 2.5 km

Wind speed: 5 m/sec

3. The Garchy, France system. (Spizzichino et al, 1965; Revah, 1968)

Bistatic backscatter system using C.W. transmission at three closely spaced frequencies. The direction of arrival is obtained from the phase relationship between the signals arriving at three antennas. Ranging is performed by an ingenious mixing of the various components of the ground and sky wave.

The main shortcoming of this system is that four stations would be required for the measurement of two wind components.

Accuracy:

For S/N = 25 dB

Direction of arrival: 1.5 degrees

Height: 3 km

Wind speed: 1 m/sec.

It should be feasible to improve the height accuracy by modifying the system. A displaced Doppler would also be an asset.

4. The Havanna, Ill. system. (Grossi, 1968; Southworth, 1968)

Multistatic system consisting of one main transmitting and receiving site and seven remote receiving stations separated from the main one by up to 30 miles and connected to it by telephone and microwave links.

Ranging can be performed from the main as well as peripheral stations by means of a pulse system. Direction finding is done by multiple ranging and phase direction finding at the main site in conjunction with information obtained from the diffraction echo.

This is a very sophisticated system that provides other information besides three dimensional winds. The high cost due to its complexity makes it very unattractive for wind measurements for which much simpler methods are

acceptable.

Accuracy:

Height: 3 km

Wind velocity: 3 - 12 m/sec depending on geometry.

5. The AFCRL system.(Ramsey and Myers, 1968; Pazniokas, 1968; Frost et al, 1970)

Monostatic system where ranging is done by pulse method and the direction finding is performed by a phase sequence interferometer that is shared for azimuth and elevation determinations.

Two Doppler systems are available for wind measurements, a non displaced one for fast moving targets and a 25.6 Hz displaced one for slow winds.

Accuracy:

Direction finding: 1 degree

Height: unavailable.

The inherent disadvantages of two back scatter systems for the measurement of two wind components are

not offset by any particularly outstanding feature of this system.

Table 2 summarizes some parameters of a number of meteor wind systems (Barnes, 1969).

Table 2 Data on Some Operating Meteor Trail Wind Sets (Feb. 1969) (After Barnes,1969)

Station	Power	Frequency (MHz)	Approx. Location	Minimum Hourly Rate	Cost Ratio	Height Accuracy (km)
Havana Ill., U.S.	3 MW pulse	40.92	40°N,90°W	(500)	10+	± 3
Adelaide S. Australia	1.5 kW cw	26.8	35°S,139°E	30	2	± 2
	65 kW pulse	27.5				
Garchy Cher, France	5 kW cw	29.7968 29.7976 29.7920	47°N, 3°E	10-20	1.5	± 3
Sheffield Yorkshire, Eng.	20 kW pulse	25	53°N, 1°W	20	0.3	Density
Durham, N.H., U.S.	30 kW pulse	36.8	43°N,71°W	15	1	± 3
Stanford Calif., U.S.	5 kW pulse	30.14	37°N,122°W	20	0.5	± 2.5
Khar'kov Ukrainian, USSR	75 kW pulse	36.9	50°N, 36°E	50		± 4
Kazan R.S.F.S.R.,USSR	100 kW pulse	72	56°N, 49°E			
Moscow P.S.F.S.R.,USSR	100 kW pulse	33	59°N, 37°E			
Fairbanks Alaska, U.S.	2 kW cw	30.2	65°N,148°W			± 8

APPENDIX 2

THEORETICAL DETERMINATION OF ANTENNA RADIATION PATTERN

All transmitting and receiving antenna arrays consist of four vertically polarized five element yagi antennas separated by half a wavelength (Fig. 31). The radiation pattern is obtained by multiplying the array factor by the pattern of an individual yagi antenna. The vertical plane array factor is equal to unity and the horizontal one is given by (Kraus, 1950),

$$E = \frac{1}{n} \frac{\sin(n\psi/2)}{\sin(\psi/2)} \qquad \text{(A2.1)}$$

where

E = electric field strength

$\psi = \pi \sin \phi$

ϕ = azimuth measured from the broadside array axis

n = 4.

In addition Crysdale and Olive (1956), report

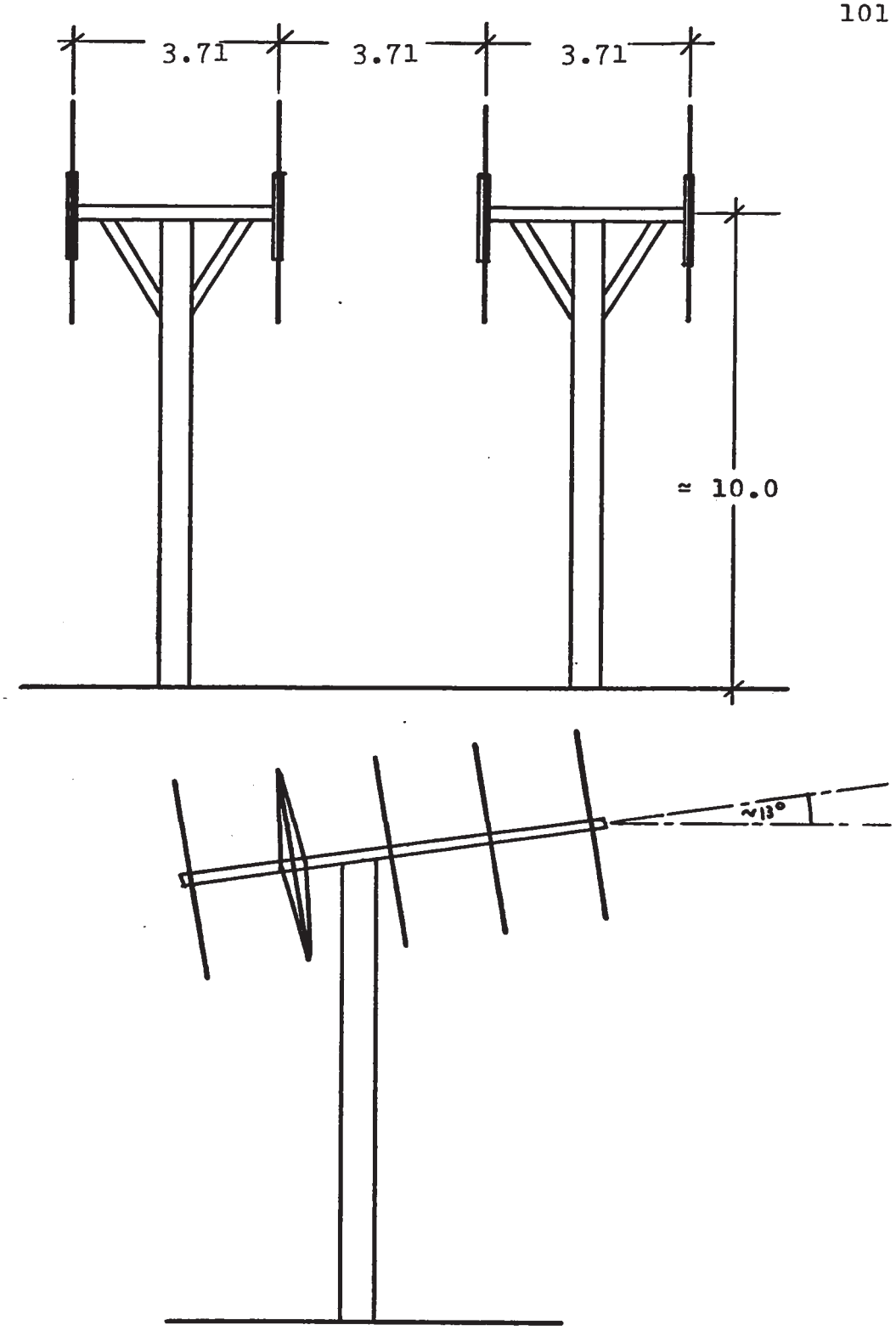

Fig. 31 Antenna array (dimensions in m)

that testing of a scaled model of the yagis used, yielded an H and E plane beamwidth of 60° and 50° respectively and a gain of approximately 10 dB. The radiation patterns can be determined by assuming the antenna to have a rectangular effective aperture A,

$$A = \frac{\lambda^2}{4\pi} g = 0.8 \lambda^2 \qquad \text{(A2.2)}$$

where

g = numerical gain

λ = wavelength.

In which case the antenna lobes correspond to the intensity diffraction pattern of a rectangular slit which in the main planes is given by

$$I = \left(\frac{\sin(\pi d \sin\theta)/\lambda}{\pi d \sin\theta/\lambda}\right)^2 \qquad \text{(A2.3)}$$

where

d = slit width

θ = angle between the observed direction and the perpendicular to the slit plane.

The sides of the slit are found from the beam-widths leading to 0.85 and 0.96 wavelengths for the horizontal and vertical sides respectively and the array radiation patterns are therefore found to be

$$P_{HOR} = K \left[\frac{\sin(2\pi\sin\phi)}{\sin(\frac{\pi}{2}\sin\phi)} \times \frac{\sin(0.85\pi\sin\phi)}{0.85\pi\sin\phi}\right]^2 \qquad \text{(A2.4)}$$

$$P_{VERT} = K \left[\frac{\sin(0.96\pi\sin\phi)}{0.96\pi\sin\phi}\right]^2 \qquad \text{(A2.5)}$$

where K = constant.

The horizontal radiation pattern is shown in Fig. 32, the vertical one, however, needs to be modified due to the effect of ground reflections which are computed for typical local ground electric properties (Jordan, 1950). The reflection coefficient for a vertical polarized signal is

$$R = \frac{(\varepsilon_R - jX)\sin\varepsilon - \sqrt{(\varepsilon_R - jX) - \cos^2\varepsilon}}{(\varepsilon_R - jX)\sin\varepsilon + \sqrt{(\varepsilon_R - jX) - \cos^2\varepsilon}} \qquad \text{(A2.6)}$$

where

ε = elevation angle

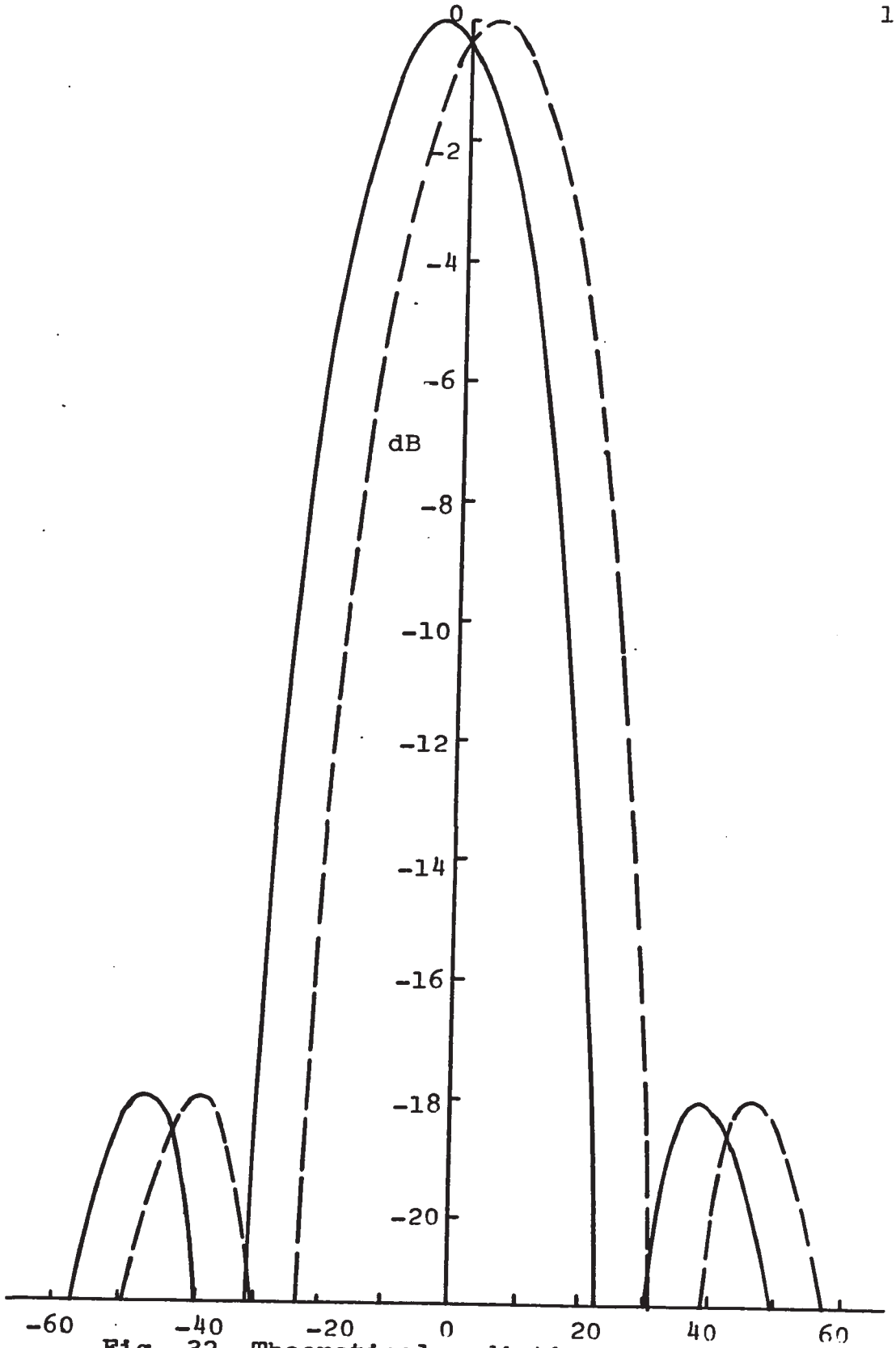

Fig. 32 Theoretical radiation patterns

ε_R = relative ground permitivity (15)

σ = ground conductivity (12×10^{-3} mho/m)

ε_V = permitivity of air

$\omega = 2\pi f$

$$X = \frac{\sigma}{\omega \varepsilon_V} .$$

Fig. 33 shows the magnitude and phase of the reflection coefficient as a function of incoming signal elevation, for the electric values shown above. However, only minor changes are produced when other values are used. From equations (A2.5) and (A2.6) in conjunction with geometrical considerations, the vertical radiation pattern shown in Fig. 34 is obtained.

Fig. 33 Reflection coefficient of typical ground for vertical polarization

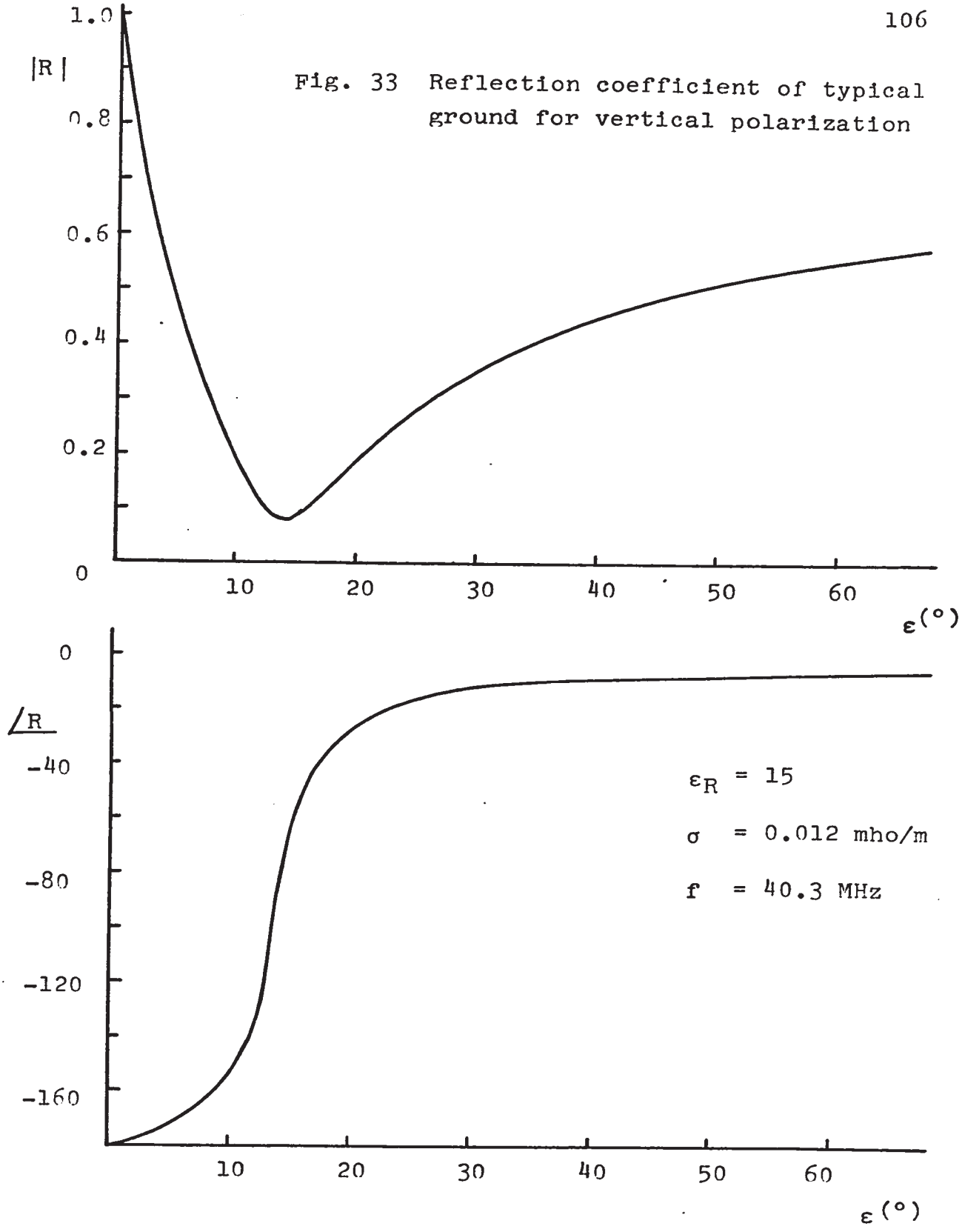

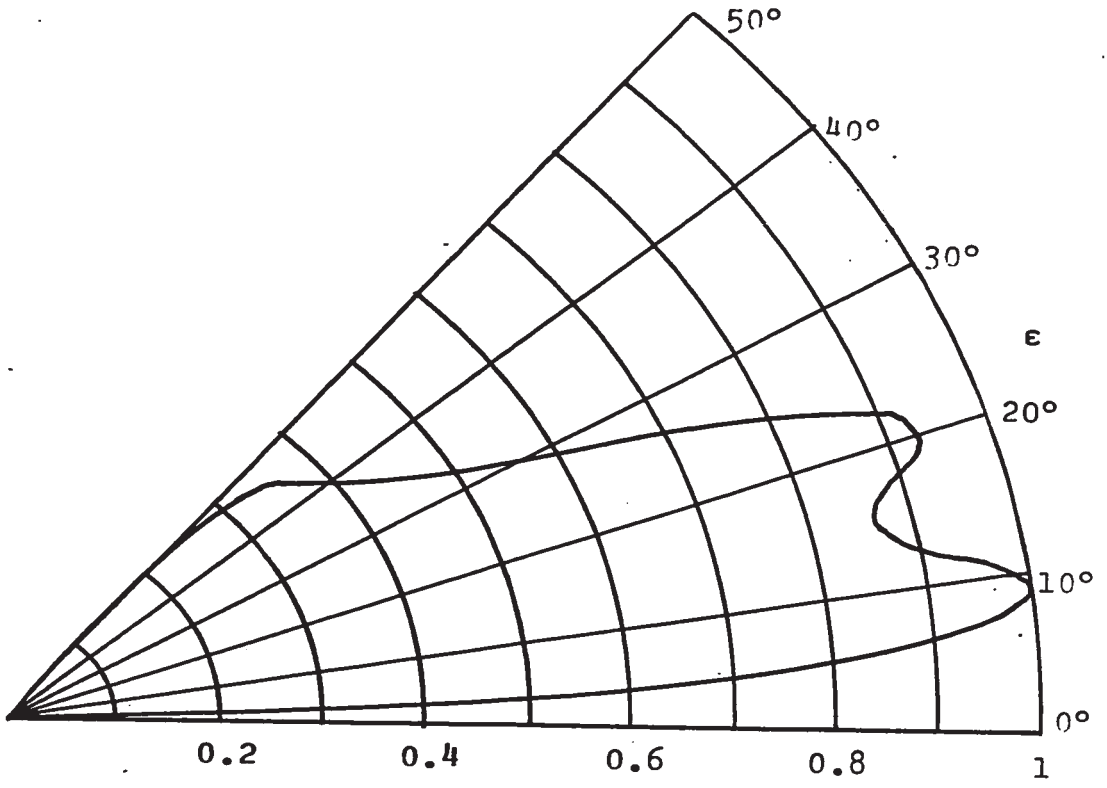

Fig. 34 Vertical plane radiation pattern (relative numerical gain)

APPENDIX 3

DETERMINATION OF THE POSITION AND MOTION OF THE SCATTERING POINT

A3.1 Location of Scattering Point

The scattering point can be located by knowing its receiving station azimuth and elevation as well as its transmitting station azimuth. The first two are obtained with the direction finding systems and the last one from the amplitude ratio between the signals received at the two frequencies.

A3.1.1 Determination of Elevation and Azimuth

Fig. 35 shows the geometry associated with the direction finding, where

P = scattering point

L = receiving station (Delaware)

θ_{NS} = angle between incident ray and N-S antenna axis

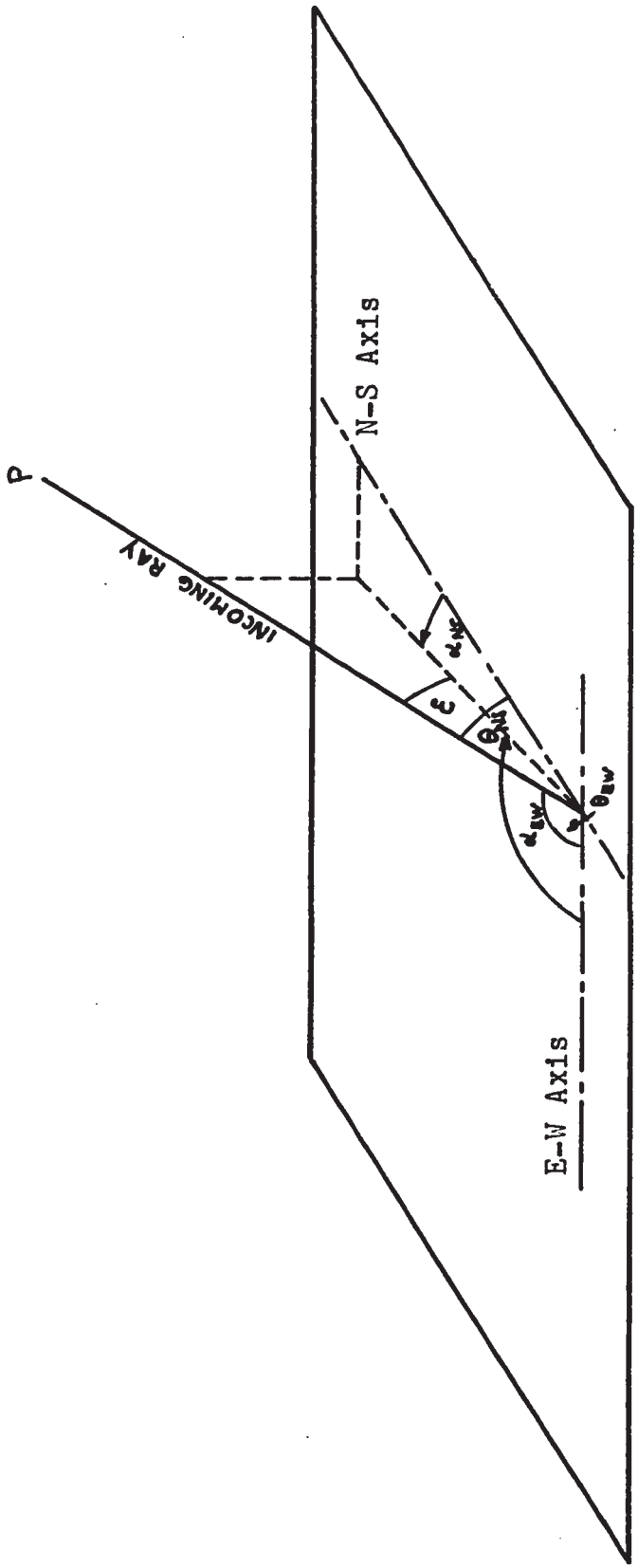

Fig. 35 Direction finding geometry

θ_{EW} = angle between incident ray and E-W antenna axis

ε = elevation of scattering point

α_{NS}, α_{EW} = azimuths scattering point measured from the N-S and E-W antenna axis.

From equation (4.2)

$$\theta = \text{arc cos } \frac{\psi \lambda}{2\pi d}$$

and from Fig. 35 it can be shown that

$$\cos \theta_{NS} = \cos \alpha_{NS} \cos \varepsilon \qquad \text{(A3.1)}$$

$$\cos \theta_{EW} = \cos \alpha_{EW} \cos \varepsilon \qquad \text{(A3.2)}$$

also

$$\alpha_{NS} = \alpha_o - \alpha_{EW}$$

where $\alpha_o = 91°$ = angle between N-S and E-W antenna axes.

Therefore

$$\cos \theta_{NS} = \cos \alpha_{NS} \cos \varepsilon \qquad \text{(A3.3)}$$

$$\cos \theta_{EW} = \cos(\alpha_o - \alpha_{NS}) \cos \varepsilon \qquad \text{(A3.4)}$$

from (A3.3) and (A3.4) we obtain

$$\cos\theta_{EW} = \frac{\cos(\alpha_o - \alpha_{NS})\cos\theta_{NS}}{\cos\alpha_{NS}}$$

expanding

$$\cos\theta_{EW} = (\cos\alpha_o + \sin\alpha_o \tan\alpha_{NS})\cos\theta_{NS}$$

solving for α_{NS}

$$\alpha_{NS} = \arctan\left(\frac{\cos\theta_{EW} - \cos\alpha_o\cos\theta_{NS}}{\sin\alpha_o\cos\theta_{NS}}\right) \qquad (A3.5)$$

from (A3.3)

$$\varepsilon = \arccos\frac{\cos\theta_{NS}}{\cos\alpha_{NS}} \qquad (A3.6)$$

Equations (A3.5) and (A3.6) define the elevation and azimuth in terms of known parameters.

A3.1.2 Determination of Ranges and Height

Fig. 36 shows a spherical triangle on the surface

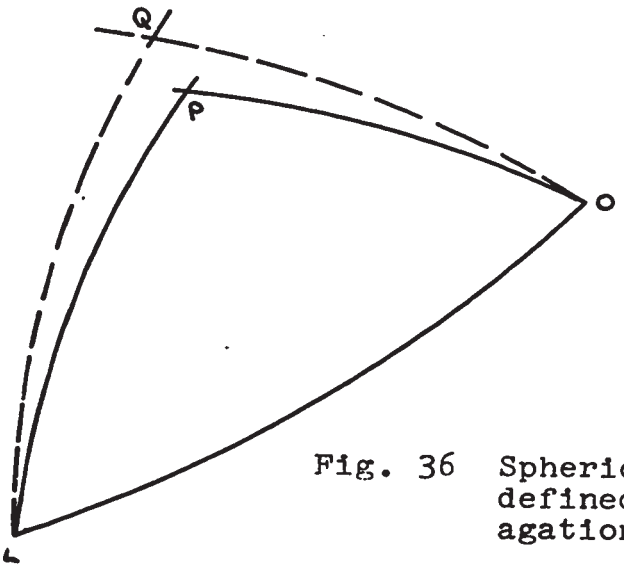

Fig. 36 Spherical triangle defined by propagation path

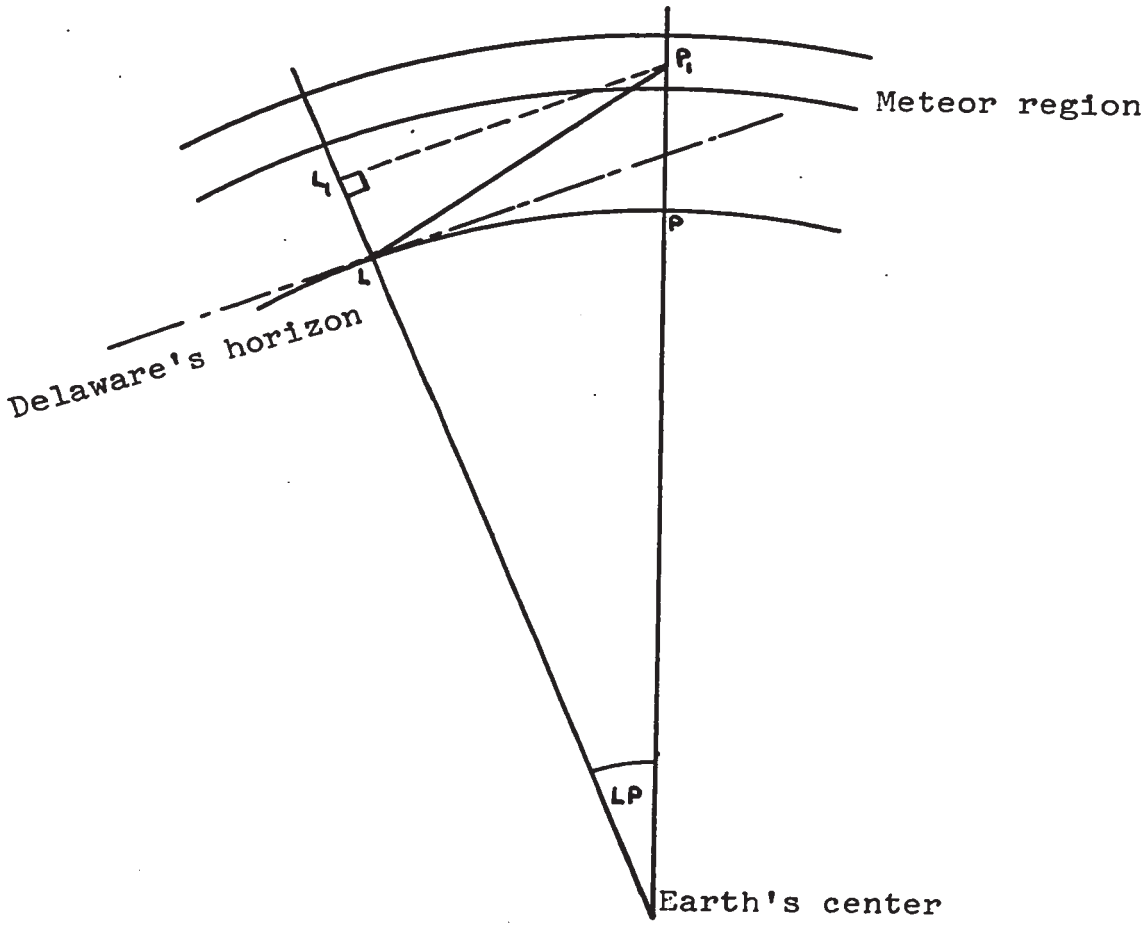

Fig. 37 Height determination geometry

of the earth defined by:

O = transmitting station (Ottawa)

L = receiving station (Delaware)

P = projection of scattering point

also

Q = intersection of transmitting and receiving antenna axis.

The following angles are known:

LO = 4.58°

QLO = 37.47°

QOL = 47.06°

QLP = receiver azimuth

QOP = transmitter azimuth

also

PLO = QLO - QLP

POL = QOL + POQ.

The projection of the scattering angle is

$$\cos(LPO) = -\cos(POL)\cos(PLO) + \sin(POL)\sin(PLO)\cos(LO)$$

let

$$S = 0.5\ (LPO + POL + PLO)$$

then

$$\cos \frac{LP}{2} = \sqrt{\frac{\cos(S-LPO)\cos(S-PLO)}{\sin(LPO)\sin(PLO)}}$$

Similarly

$$\cos \frac{OP}{2} = \sqrt{\frac{\cos(S-LPO)\cos(S-POL)}{\sin(LPO)\sin(POL)}}$$

Assuming a spherical earth with radius of 6370 km the receiver the transmitter ranges are

$$R_2 = 6370\ LP \quad km$$

$$R_1 = 6370\ OP \quad km.$$

The height of the scattering point can be determined with the assistance of Fig. 37 which depicts the great circle containing the receiving station and reflection point.

$$P_1L_1 = 6370\ \frac{\sin LP \sin(90° - \varepsilon)}{\sin(90° - \varepsilon - LP)}$$

and the height of the reflection point is

$$P_1P = \frac{P_1L_1 - 6370\sin LP}{\sin LP}$$

which completes the location of the reflection point.

A3.2 Determination of wind velocity

The wind is assumed to be horizontal and therefore only the component parallel to the horizontal projection of the bisector of the scattering angle can be observed. Fig. 38 shows a flat earth approximation for the scattering geometry which is sufficiently accurate for the wind calculations.

The Doppler shift of the received signal results from variations in the propagation path length ($OP_1 + P_1L$) as a function of time due to trail drift. For a horizontal displacement PP' of the reflection point we have (Fig. 39),

$$\Delta OP_1 = OP_1 - OP_1' = (OP - OP')\cos \varepsilon_T = \Delta OP \cos \varepsilon_T$$

Similarly

$$\Delta LP_1 = LP_1 - LP_1' = (LP - LP')\cos \varepsilon_R = \Delta LP \cos \varepsilon_R$$

where

ε_R, ε_T = receiver and transmitter elevation angle of reflection point.

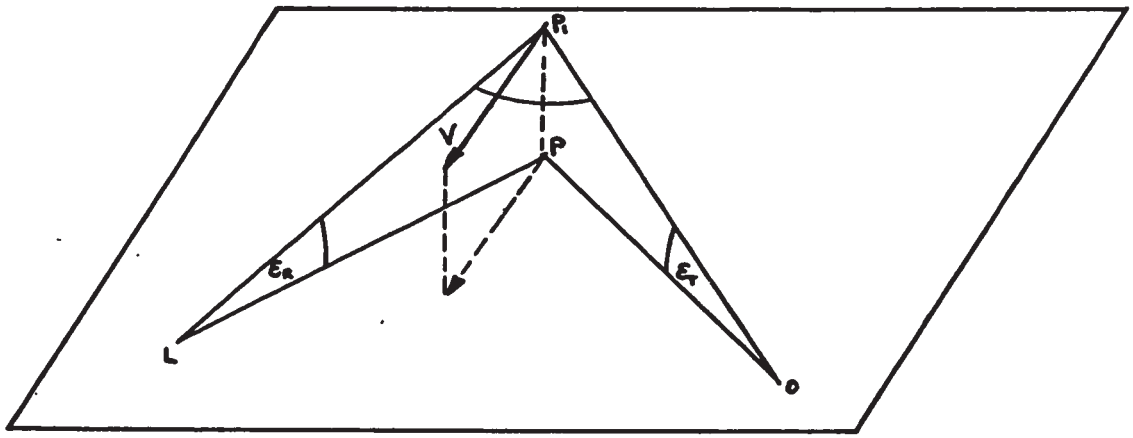

Fig. 38 Geometry for the determination of wind velocity

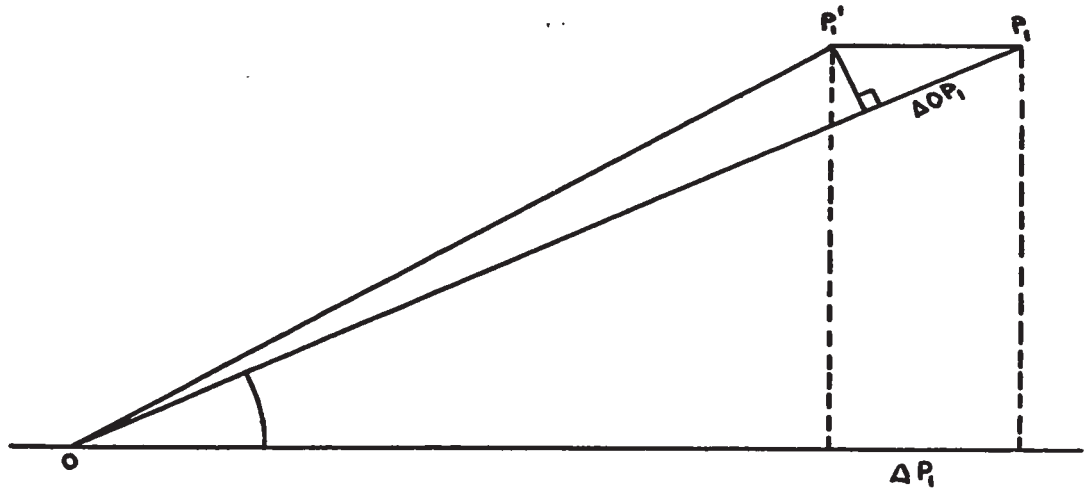

Fig. 39 Geometry associated with wind measurements

Therefore the change in propagation path length is

$$\Delta(OP_1 + LP_1) = \Delta OP \cos \varepsilon_T + \Delta LP \cos \varepsilon_R$$

and from the symmetry in the geometry

$$\frac{\Delta OP_1}{\Delta t} = \frac{\Delta LP_1}{\Delta t} = |V| \cos \frac{LPO}{2}$$

where $|V|$ is the magnitude of the desired wind component. Since the Doppler frequency is given by,

$$\Delta f = \pm \frac{\frac{d(OP + PL)}{dt}}{\lambda} \quad \text{Hz}$$

the wind component becomes

$$|V| = \frac{\Delta f \cdot \lambda}{\cos \frac{LPO}{2} (\cos \varepsilon_T + \cos \varepsilon_R)} \quad . \qquad \text{(A3.7)}$$

APPENDIX 4

DETERMINATION OF DOPPLER SHIFT OF RECEIVED SIGNAL

Since the conversions in the receiver do not affect the frequency changes of the received signal, the Doppler shift can be measured at a low frequency (4500 Hz) by means of a lock-in amplifier (Fig. 13) consisting of two phase sensitive detectors into which the converted and a reference signal are applied (Fig. 40). The received signal going into the "quadrature" detector is shifted by 90° as opposed to the one fed into the "in phase" detector which is not altered. The two systems are necessary to determine the sense of the Doppler shift which establishes whether the target under observation is approaching or receding.

The output from the phase sensitive detectors is equal to the product of the two input signals.

Let

$$A \sin \omega t$$

and

$$B \sin(\omega_o t + \alpha)$$

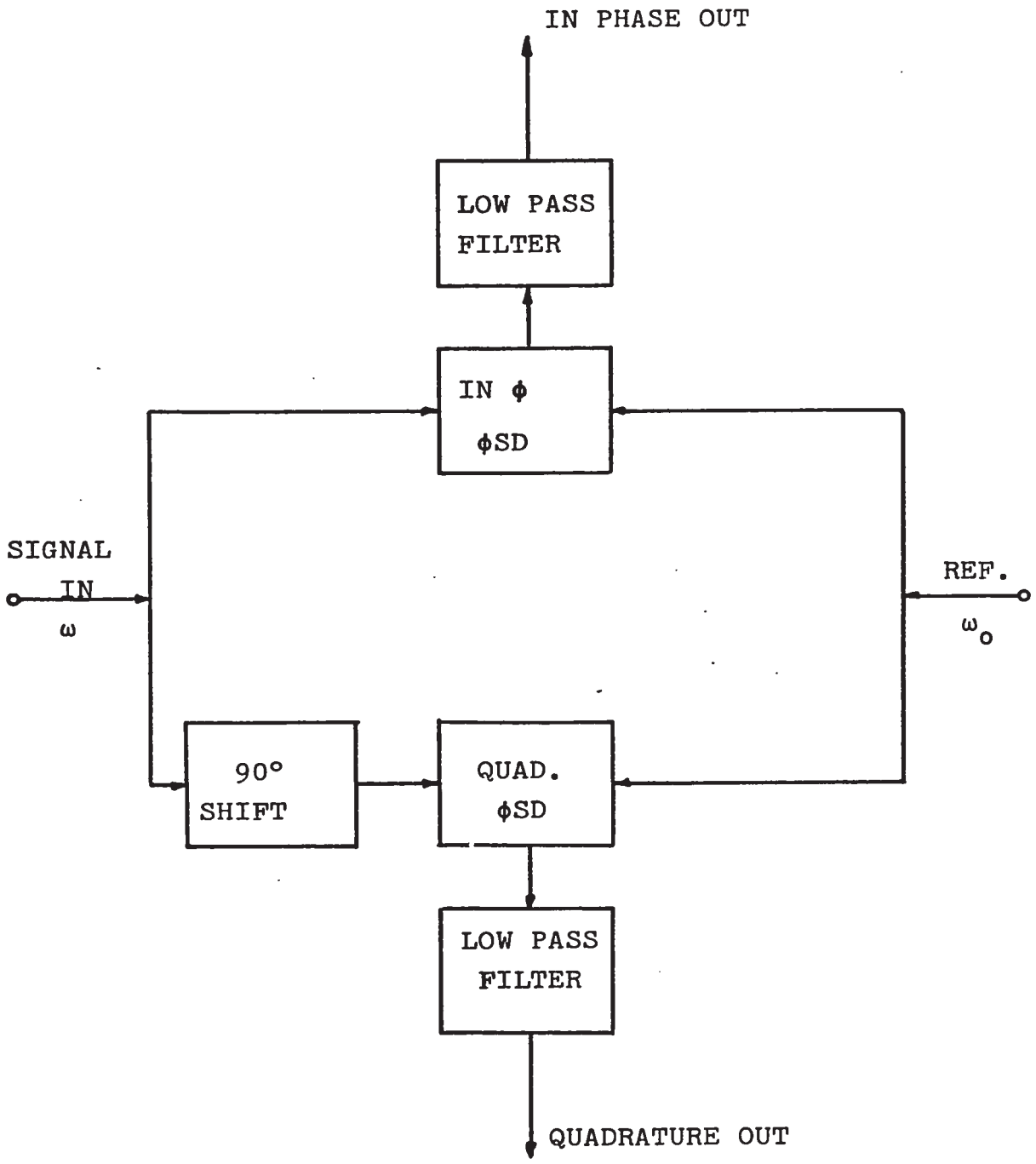

Fig. 40 Lock-in amplifier block diagram

be the input and reference signals respectively. In the system under discussion $\omega_o = \omega$ when no Doppler shift is present, thus yielding a "non displaced" Doppler output. Therefore, the outputs from the "in phase" and "quadrature" phase sensitive detectors are:

$$V_{in\ \phi} = K\ [\cos\{(\omega - \omega_o)t - \alpha\} - \cos\{(\omega + \omega_o)t + \alpha\}]$$

$$V_{quad} = K\ [\cos\{(\omega - \omega_o)t - \frac{\pi}{2} - \alpha\} - \cos\{(\omega + \omega_o)t - \frac{\pi}{2} + \alpha\}]$$

where K = constant.

Low pass filters eliminate the higher frequency components leading to

$$V_{in} = K \cos\{(\omega - \omega_o)t - \alpha\}$$

$$V_{quad} = K \cos\{(\omega - \omega_o)t - \frac{\pi}{2} - \alpha\}$$

which can be represented by the following phasor diagram

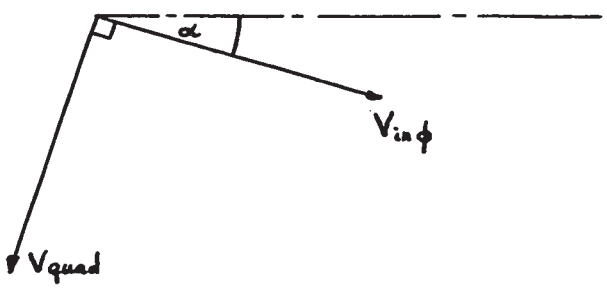

For ω greater than ω_o the phasors rotate counter clockwise and the "in phase" output signal leads the "quadrature" output. If $\omega_o > \omega$ the phasors rotate in the opposite direction with the "quadrature" output leading by 90°. It is therefore apparent that the phase relationship between the two outputs from the lock-in amplifier provides the sense of the Doppler shift.

APPENDIX 5

SYSTEM NOISE TEMPERATURE

The noise power generated by a receiver is

$$P_{NR} = k T_R B \qquad \text{(A5.1)}$$

where

k = Boltzman's constant = 1.38×10^{-23} joules/°K

B = receiver bandwidth

T_R = noise temperature of the receiver referred to the antenna terminals and given by,

$$T_R = T_F + \frac{T_{RF}}{G_F} + \frac{T_M}{G_F G_{RF}} + \ldots \qquad \text{(A5.2)}$$

where

T_F = noise temperature of the antenna feed line

T_{RF} = noise temperature of RF amplifier

G_F = power gain of the antenna transmission line (attenuation $L_F = \frac{1}{G_F}$)

T_M = noise temperature of the first mixer and IF amplifier

G_{RF} = power gain of RF amplifier.

If G_{RF} is sufficiently high only the first two terms of (A5.2) need to be considered. The noise temperature of the transmission line is,

$$T_F = (L_F - 1)\, T_{FP} \qquad \text{(A5.3)}$$

where

T_{FP} = physical temperature of the transmission line.

The system noise temperature is the sum of the receiver and antenna noise temperature

$$T_{SN} = T_R + T_A \qquad \text{(A5.4)}$$

In the case being considered the transmission lines are 500 feet of RG-8 coaxial cable with a total attenuation of 6 dB. To avoid the degradation of the signal-to-noise ratio associated with such a loss, antenna preamplifiers with noise figure of approximately 3 dB and gain of 32 dB

are inserted at the base of the antennas. Since noise temperature is related to noise figure by

$$T_{RF} = (F - 1)\, T_o$$

where

$$T_o = 290°K.$$

The receiver noise temperature becomes

$$T_R = (1.1 - 1)290 + (2.0 - 1)\cdot 290 \cdot 1.1$$
$$= 346°K.$$

The average sky noise temperature at 40 MHz is about 7000°K (Pawsey and Bracewell, 1955); assuming the antenna noise temperature to be equal to it, the system noise temperature T_{SN} is found to be (from A5.4)

$$T_{SN} = 7000 + 346 \simeq 7350°K.$$

APPENDIX 6

DETERMINATION OF PHASE CONSTANTS OF RECEIVING SYSTEM

A6.1 General

Since the direction of arrival of the received signal is obtained from the absolute phase relationship between the signals arriving at the receiving antennas (equations 3.2, 3.3 and 3.4), it is necessary to determine the constant differential phase shifts added by the receiving system due to the dissimilarity between the various channels. These phase constants are obtained by dividing the system in two subsystems comprising

(1) complete receivers

(2) antennas, preamplifiers and transmission lines

leading to partial phase constants ψ_{c1} and ψ_{c2} respectively. The total phase constant is then

$$\psi_c = \psi_{c1} + \psi_{c2} \qquad \text{(A6.1)}$$

A6.2 Determination of ψ_{c1}

The phase constants corresponding to subsystem (1)

are obtained directly by feeding signals with known phase relationship to the receivers in question. The output phase difference in conjunction with the input relationship provide the necessary information. It was found that

$$\psi_{c1_{NS}} = 55° \text{ (channel 2 leading 3)}$$

$$\psi_{c1_{EW}} = 3° \text{ (channel 1 leading 2).}$$

A6.3 Determination of ψ_{c2}

The second phase constant, ψ_{c2} is obtained by operating the system as a phase switched interferometer to observe the radio star Cassiopeia A, whose known position permits a theoretical determination of the interferometer output as a function of ψ_{c2}. The actual value of the phase constant is then found by matching the experimental and theoretical interferometer outputs.

A6.3.1 Description of Interferometer

In order to operate as a phase switched interferometer, the system was connected as shown in Fig. 41. The

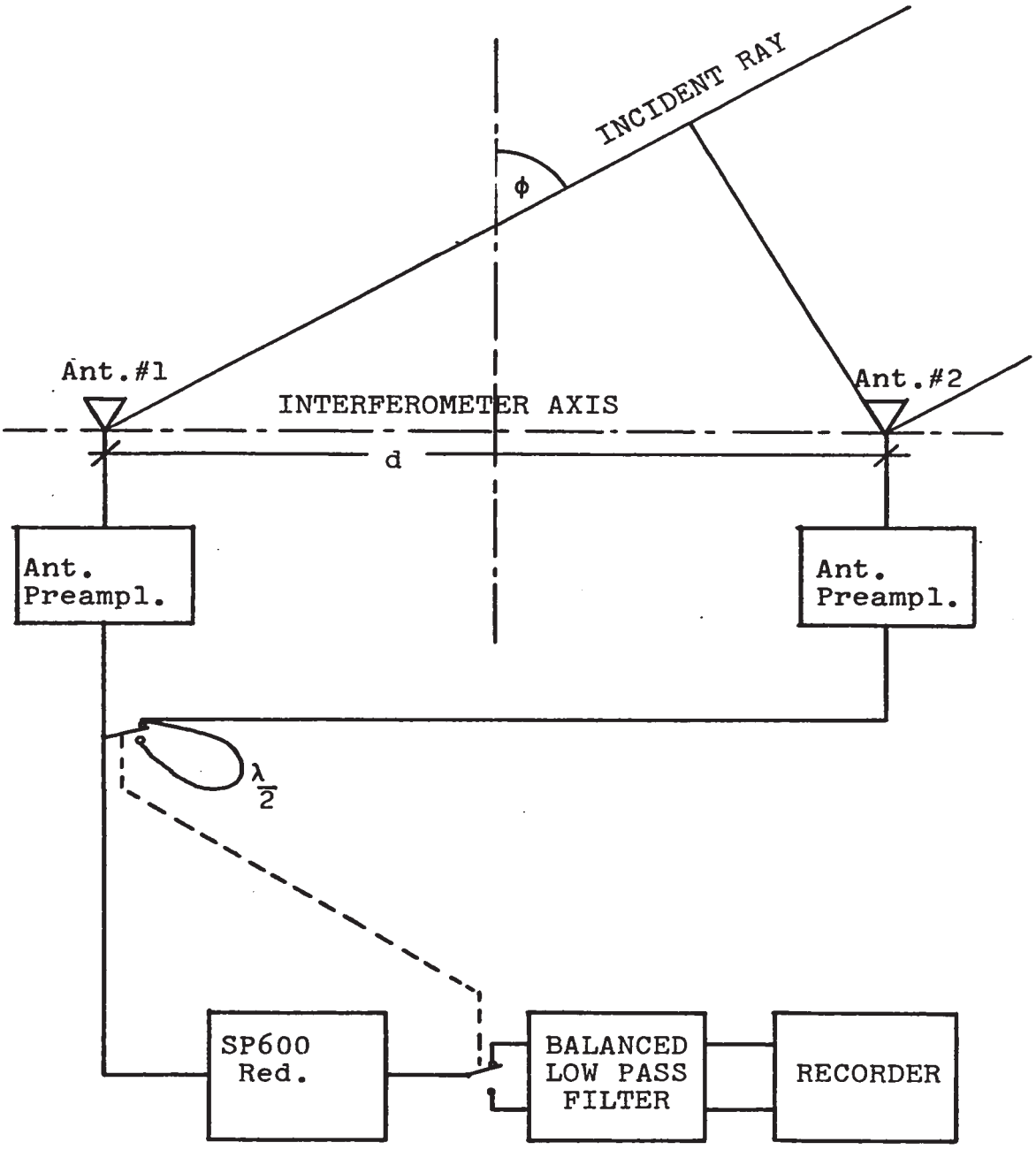

Fig. 41 Interferometer block diagram

components preceeding the coaxial relay are the ones used under normal operation and the receiver is one of the siamesed SP 600's whose "diode output" is used to drive a low speed paper chart recorder via a low pass filter and DC amplifier. Phase switching is done by means of the coaxial relay operating at about 1 Hz which switches one half wavelength in and out of one of the transmission lines. Another relay contact operating in synchronism, switches the receiver output between the two low pass filter inputs. The interferometer was operated for about two weeks in the determination of each the N-S and E-W phase constants.

A6.3.2 Brief Theory on Interferometer Operation

Consider the interferometer shown in Fig.41. The phase difference between the signals arriving at the two antennas is

$$\psi = \frac{2\pi d}{\lambda} \sin \phi \qquad \text{(A6.2)}$$

where

ϕ = angle between incoming ray and a plane perpendicular to the interferometer axis.

In the following analysis it is assumed that the two arrays have diverging radiation lobes, which is true in the case of the E-W pair. The simpler configuration of coincident patterns (in the N-S pair) is obtained from the more general case.

Let $E_1(\phi)$ and $E_2(\phi)$ be the normalized gain of each array as a function of ϕ. When the relay is in the "in phase" ($\lambda/2$ removed) position, the signal amplitude at the receiver input is (Kraus, 1966)

$$E(\phi)_i = E_1(\phi) + E_2(\phi)e^{j(\psi + \psi_{c2})} \tag{A6.3}$$

where

ψ_{c2} = unknown phase constant.

The preamplifier gains and transmission line losses have been disregarded because they do not affect the final result. When the relay is in the "out of phase" position, the signal amplitude at the receiver input is

$$\begin{aligned} E(\phi)_o &= E_1(\phi) + E_2(\phi)e^{j(\psi + \pi + \psi_{c2})} \\ &= E_1(\phi) - E_2(\phi)e^{j(\psi + \psi_{c2})} \end{aligned} \tag{A6.4}$$

and the corresponding powers are

$$P(\phi)_i = E(\phi)_i \quad E(\phi)_i^*$$

$$P(\phi)_o = E(\phi)_o \quad E(\phi)_o^*$$

By substitution it is found that

$$P(\phi)_i = |E_1(\phi)|^2 + |E_2(\phi)|^2 + E_1(\phi)E_2(\phi)^* e^{-j(\psi+\psi_{c2})} + \\ + E_1(\phi)^* E_2(\phi) e^{j(\psi+\psi_{c2})}$$

$$P(\phi)_o = |E_1(\phi)|^2 + |E_2(\phi)|^2 - E_1(\phi)E_2(\phi)^* e^{-j(\psi+\psi_{c2})} \\ - E_1(\phi)^* E_2(\phi) e^{j(\psi+\psi_{c2})}$$

Due to the synchronism in the switching, the signal fed to the low pass filter and recorder is proportional to the difference in the input powers

$$P(\phi) = P(\phi)_i - P(\phi)_o$$

$$P(\phi) = 2E_1(\phi)E_2(\phi)^* e^{-j(\psi+\psi_{c2})} + E_1(\phi)^* E_2(\phi) e^{j(\psi+\psi_{c2})}$$

However, for the arrays in question $E(\phi)$ is real and therefore

$$E_1(\phi) = E_1(\phi)^*$$

$$E_2(\phi) = E_2(\phi)^*$$

and

$$P(\phi) = 2E_1(\phi)E_2(\phi)(e^{j(\psi+\psi_{c2})} + e^{-j(\psi+\psi_{c2})})$$

$$= 4E_1(\phi)E_2(\phi)\cos(\psi+\psi_{c2})$$

By virtue of (A6.1) the output power becomes

$$P(\phi) = 4E_1(\phi)E_2(\phi)\cos\left(\frac{2\pi d}{\lambda}\sin\phi + \psi_{c2}\right) \qquad \text{(A6.5)}$$

Similarly in the case of the N-S pair, where the radiation patterns are coincident

$$P(\phi) = 4E(\phi)^2 \cos\left(\frac{2\pi d}{\lambda}\sin\phi + \psi_{c2}\right) \qquad \text{(A6.6)}$$

Equations (A6.5) and (A6.6) describe the interferometer output as a function of the direction of the incident ray

and system phase constant. Therefore $P(\phi) = 0$ for

$$\frac{2\pi d}{\lambda} \sin\phi + \psi_{c2} = n \frac{\pi}{2} \qquad n= 1, 3, 5, \ldots$$

and if the arrays were isotropic $P(\phi)$ would have extreme values for

$$\frac{2\pi d}{\lambda} \sin\phi + \psi_{c2} = n \frac{\pi}{2} \qquad n= 0, 2, 4, \ldots$$

However, due to the directivity of the arrays, this is not true although near the array axis the error is not very important. Therefore within these limitations

$$\frac{2\pi d}{\lambda} \sin\phi + \psi_{c2} = n \frac{\pi}{2} \qquad n= 0, 1, 2, \ldots \quad (A6.7)$$

correspond to zero and extreme values of the interferometer output. Consequently, the locus for the position of the radio source that provides either extreme or zero output from the interferometer lies on a family of cones centered at the interferometer axis with semi angles equal to α.

The position of the interferometer axis in celestial coordinates must be determined so that the location of the circles produced by the projection of the cones on the celestial sphere is known. The intersection

of these circles with the orbit of Cassiopeia A correspond to the locations of the star that provide the interferometer outputs defined by (A6.7). Fig. 42 shows the geometry associated with the determination of the points of intersection.

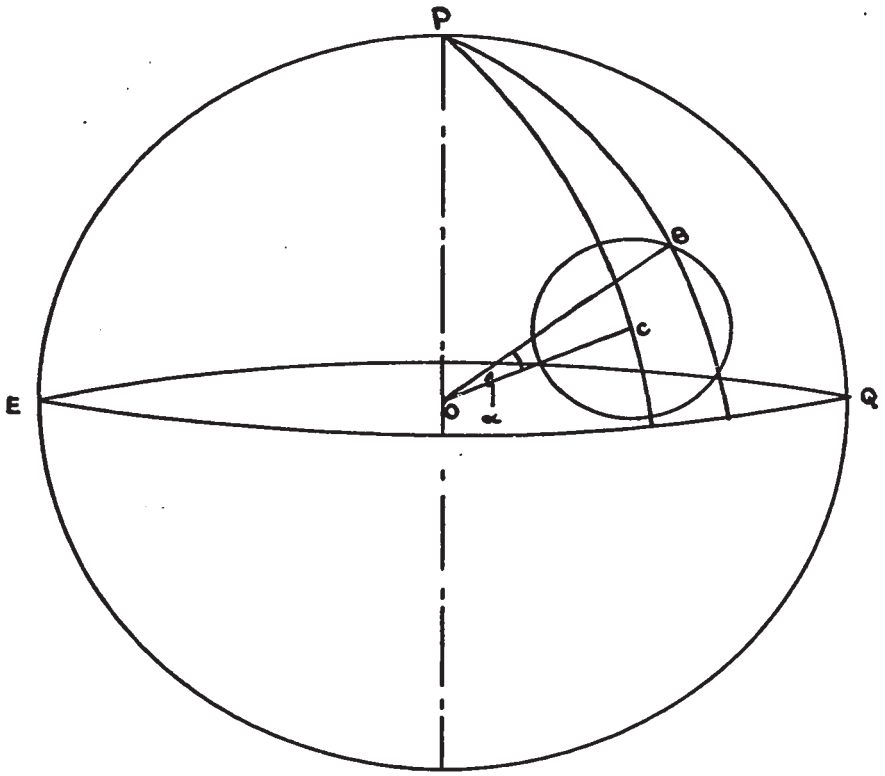

Fig. 42 Geometry associated with interferometer operation

where

P = celestial north pole

O = earth's center

PEQ = meridian through receiving station

C = projection of interferometer axis on celestial sphere

α = semi angle of cone centered at interferometer axis = BC

B = point on circle produced by the projection of cone on the celestial sphere.

In ΔPCB

$$\cos\alpha = \cos PC \cos PB + \sin PB \sin PC \cos(CPQ-BPQ) \qquad (A6.8)$$

In the case of the N-S axis (section A6.4)

$$PC = 45.09^\circ$$

$$CPQ = 26.76^\circ$$

Therefore

$$\cos\alpha = \cos 45.09^\circ \cos PB + \sin 45.09^\circ \sin PB \cos(26.76^\circ - BPQ) \qquad (A6.9)$$

Since

$$\alpha = \frac{\pi}{2} - \phi \qquad (A6.10)$$

and the points of interest are the intersections with the orbit of Cassiopeia given by

$$PB' = 31.45°$$

(A6.9) can be rewritten

$$\cos(26.76° \pm BPQ) = \frac{\cos\alpha - \cos 45.09° \cos 31.45°}{\sin 45.09° \sin 31.45°} \qquad \text{(A6.11)}$$

which gives the values of $\Psi(=BPQ)$ for the desired intersections. The times corresponding to the various intersections can be found by Cassiopeia's orbital parameters.

A6.3.3 Interferometer Results

A computer program was developed to determine the times of the events as a function of the system phase constant (equations A6.7, A6.10, A6.11). It can be shown that due to the geometry and the directivity of the antennas, the radio star could be observed near its lower transit only, which is in agreement with the experimental results.

Figs. 43 and 44 show contours of times of events as a function of phase constant for the N-S and E-W pairs respectively. The average times of the experimental events (normalized to the indicated date) are shown by the vertical lines. The phase constants can be obtained by fitting a horizontal line to the intersections of the theoretical and experimental results. More weight was given to the zero crossings because they are better defined and are not affected by the antenna patterns. The rather large scatter of the intersection points could probably be reduced by taking more measurements, however it appears that the results obtained are satisfactory on the basis of the meteor height distribution obtained using them.

A6.4 Interferometer Sensitivity

The sensitivity of a phase switched interferometer is (Tiuri, 1964)

$$\Delta T_{min} = 2 \frac{T_{SN}}{\sqrt{B_{HF}\tau}} \qquad \text{(A6.12)}$$

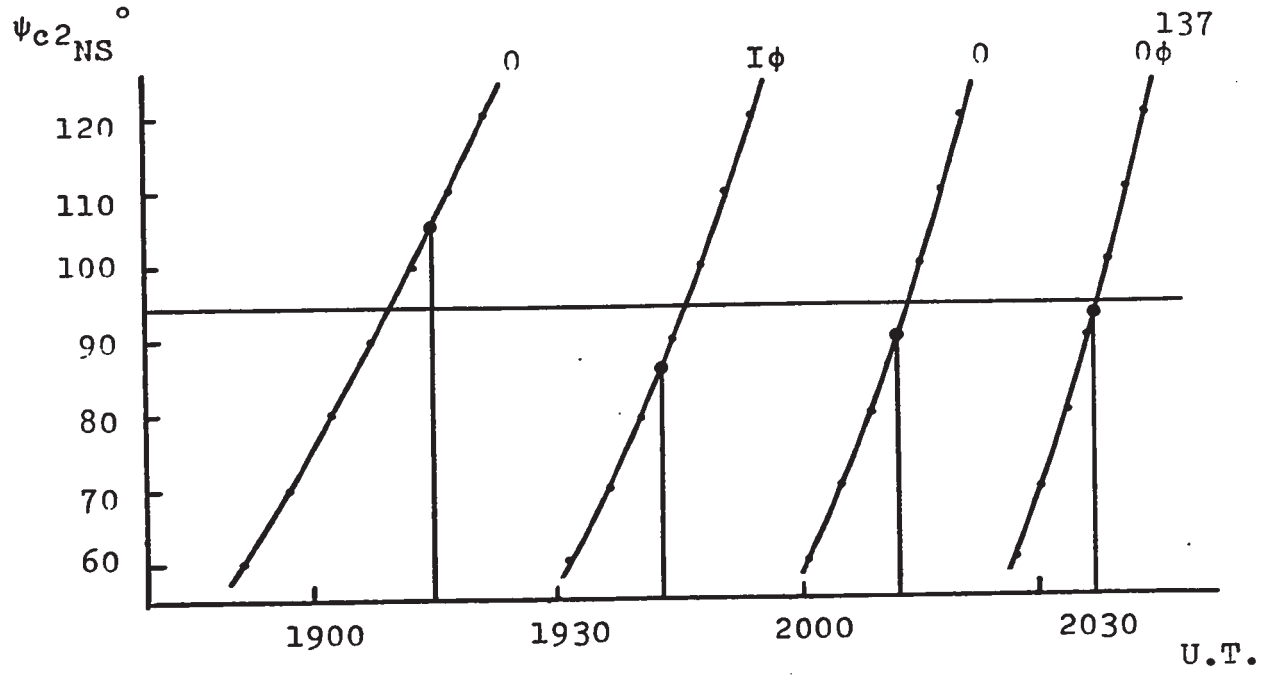

Fig. 43 Times of events as a function of phase constant for N-S interferometer (Normalized to Oct. 1, 1970; channel 3 leads 2)

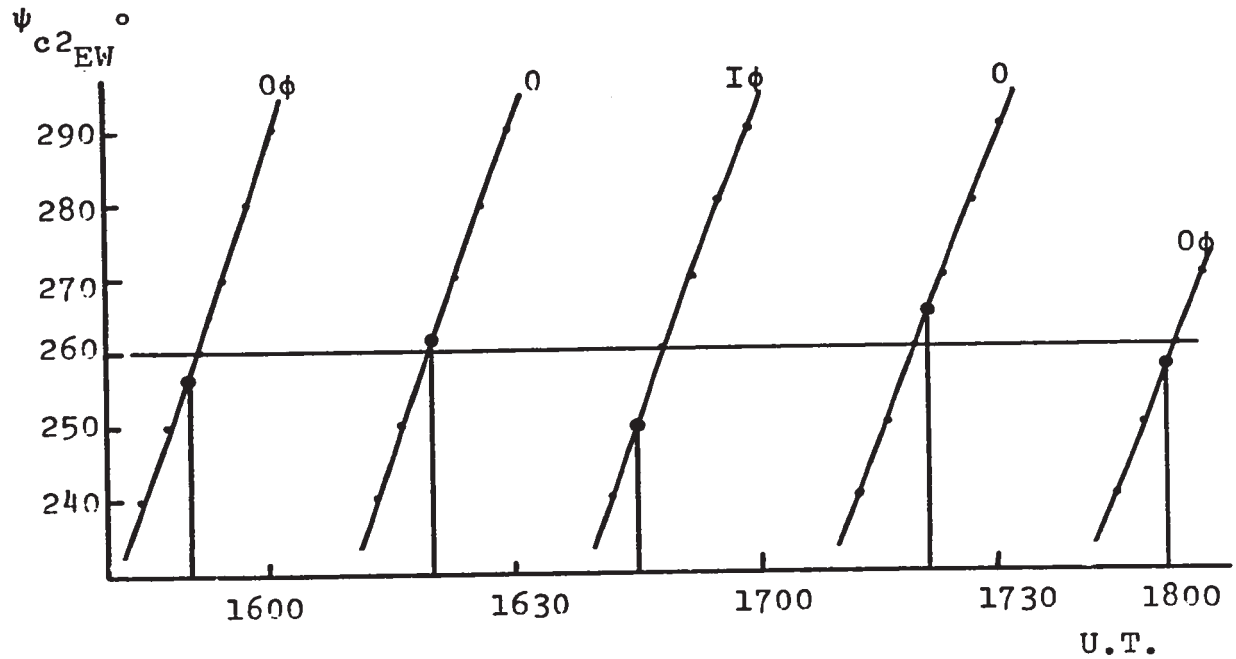

Fig. 44 Times of events as function of phase constant for E-W interferometer (Normalized to Oct. 15, 1970; # 1 leads # 2)

where:

B_{HF} = high frequency receiver bandwidth

τ = post detection integrator time constant

T_{SN} = system noise temperature.

Thus the sensitivity of the interferometer can be improved by increasing B_{HF} and τ, however the following limitations are encountered.

(1) The integration time constant cannot be increased to a point where it distorts the desired output. Therefore τ must be notably shorter than the period of the observed events. A time constant of approximately one minute was used which is well below the observed period of about two hours.

(2) The RF bandwidth cannot be increased indefinitely due to two reasons:

(a) The interferometer is used to determine the phase constants of the system, which requires an accurate knowledge of the interferometer lobe structure. The definition of this structure decreases with increasing bandwidths. In general it is sufficient for the bandwidth to be a very small percentage of the center frequency.

(b) The use of large bandwidths permits the reception of undesired signals which render useless the interferometer output. This is by far the more stringent condition, which led to the selection of a 3 kHz bandwidth.

A6.5 Determination of Celestial Coordinates of Interferometer Axes

Fig. 45 shows the geometry involved in the determination of the celestial orientation of the interferometer axis.

O = center of celestial sphere located at the earth

P = north celestial pole

ETQ = celestial equator (Q defines $\Psi = 0$)

Z = zenith of receiving station (Delaware)

EZPQ = Delaware's celestial meridian

SRN = horizon at Delaware (N = north)

OC = direction of the N-S interferometer axis

OR = projection of OC on horizon

OC' = direction of E-W interferometer

Known parameters:

PN = latitude of Delaware = 42.86°N

NR = azimuth of N-S axis = 18.6°

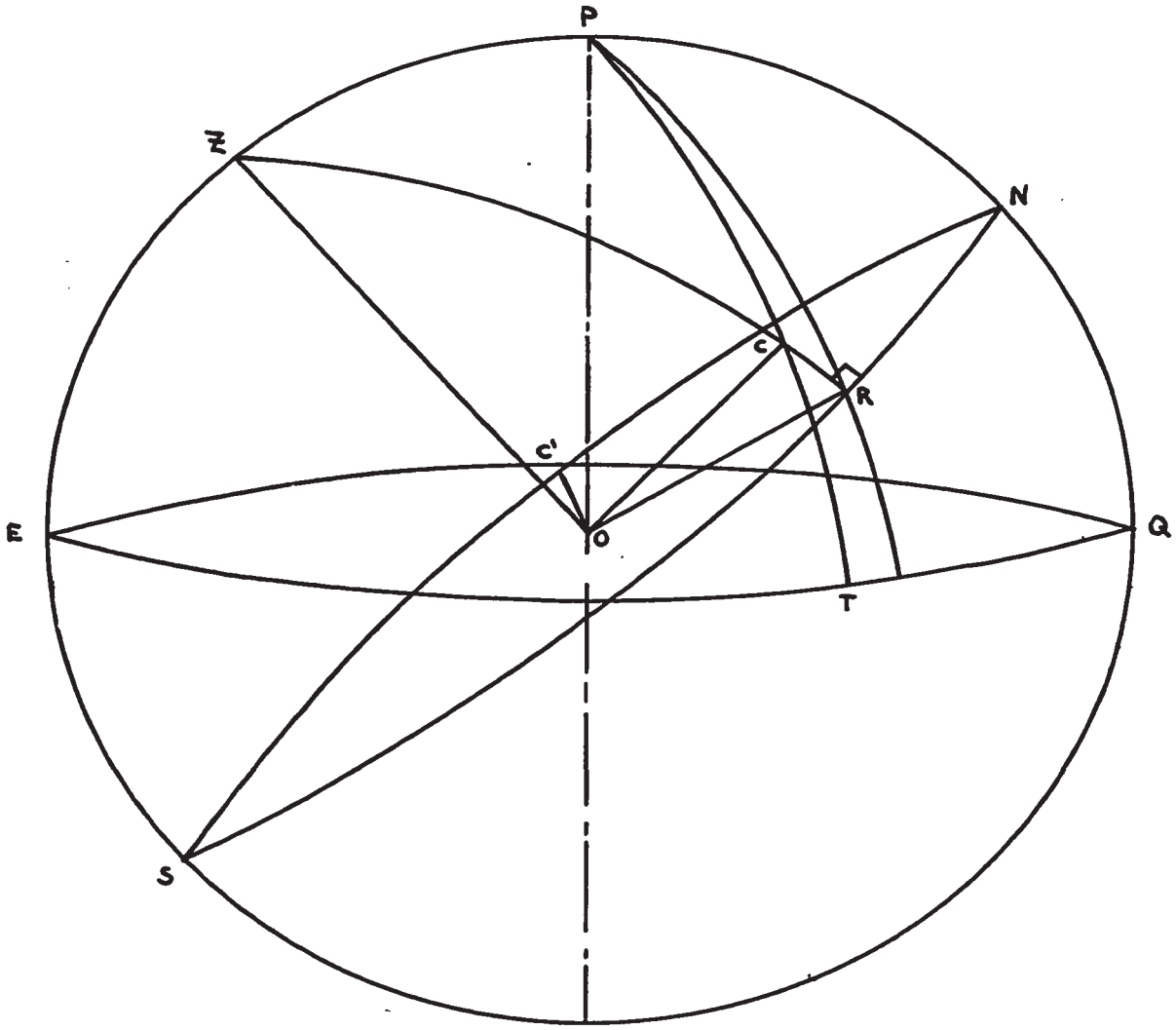

Fig. 45 Celestial orientation of interferometer axes

NC' = supplement of E-W axis azimuth = 72.4°

CR = N-S axis elevation = 57'

In ΔPNR

$$\cos PR = \cos NR \cos PN + \sin NR \sin PN \cos 90°$$

Therefore PR = 46°.

Also

$$\frac{\sin NPR}{\sin NR} = \frac{\sin 90°}{\sin PR}$$

Therefore NPR = 26.33°

In ΔNRC

$$\cos CN = \cos RC \cos RN + \sin RC \sin RN \cos 90°$$

Therefore CN = 18.62°

and

$$\frac{\sin CNR}{\sin RC} = \frac{\sin 90°}{\sin CN}$$

Therefore CNR = 2.98°

In ΔPCN

$$PNC = 90° - CNR = 87.02°$$

$$\cos PC = \cos PN \cos CN + \sin PN \sin CN \cos PNC$$

Therefore $PC = \theta = 45.09°$ (A6.13)

$$\frac{\sin CPN}{\sin CN} = \frac{\sin PNC}{\sin PC}$$

Therefore $PCN = \Psi = 26.76°$ (A6.14)

Equations A6.13 and A6.14 define the position of the N-S interferometer axis. A similar analysis for the E-W pair yields:

$$\theta' = 77.22°$$

$$\Psi' = 282.15° = -77.85°.$$

APPENDIX 7

ERROR ANALYSIS

A7.1 General

The total error associated with the measurements results from the addition of several error components, one of which is due to the noise in the received signal. Since noise can most easily be treated on an RMS basis, it is felt that the others should also be expressed in the same terms. Further it is suggested that a peak error analysis would not reflect realistically the performance of the system, particularly in view of the rather numerous and mostly independent error components to be considered. The RMS error components were estimated at the calibration points which were required regularly as a consequence of the instabilities in the paper chart recorder used to display the results.

A7.2 Amplitude Ratio

The error in the amplitude ratio is made up of the following components:

(a) Error in chart reading

This error is basically due to the thickness of the line on the chart paper and is estimated to be 0.1 dB.

(b) Calibration errors

Inasmuch as the same generator is used to calibrate both amplitude channels, the only source of error could be in the relative signal levels obtained at the various signal generator attenuator settings. However since echoes with amplitude ratios of less than 8 dB were used only, the error accumulated over that interval probably does not exceed 0.1 dB. Since the calibration levels are read off the chart, error (a) must again be considered here. Therefore, the total RMS calibration error is 0.14 dB.

(c) Error due to chart paper lateral drift

There was a considerable lateral motion of up to 1 cm of the chart paper, which in conjunction with the imperfectly logarithmic and slightly different amplitude calibrations of the two channels, leads to an estimated

error of 0.5 dB in the ratio measurement.

(d) Error due to recorder non-linearity

In order to compensate for the chart paper lateral motions it was necessary to readjust frequently the zero reference of the pens. Due to recorder non linearity, these changes produced variations in the amplitude calibration of the individual channels which resulted in errors of approximately 0.5 dB in the amplitude ratio.

(e) Error due to channel cross talk

The cross talk between the two channels is in the order of -30 dB (Fig. 15) which corresponds to an error of 0.008 dB in the ratio measurement.

(f) Error due to Doppler shift

The bandpass characteristics of the receiver have rather steep slopes at the two frequencies of interest (Fig. 15). To minimize the error in the amplitude ratio measurement resulting from Doppler shifts in the received signal, the program used to compute the position of the reflection point includes a correction for the amplitude ratio as a function of the Doppler shift, based on straight line tangents to the bandpass characteristics at the two nominal frequencies. Considering the small Doppler shifts

that are present, the straight line approximation is quite sufficient and renders the errors negligible.

(g) Errors due to post filtering receiver instability

The post filtering receiving subsystem was found to be extremely stable under normal operating conditions which included complete line voltage and power supply regulation as well as close temperature control.

(h) Error due to noise

As is shown in the following section, the error in amplitude ratio due to noise for a typical echo with S/N of 20 dB is approximately 0.06 dB.

The total RMS error in the amplitude ratio measurement is given by the sum of the components listed above.

$$\Delta A = \sqrt{2(a)^2 + 2(b)^2 + (c)^2 + (d)^2 + (e)^2 + (h)^2}$$

$$\simeq 0.75 \text{ dB}$$

A7.2.1 Effect of Noise on Amplitude Ratio Accuracy

The predetection signal consists of the desired

component with envelope amplitude S and noise which being of thermal origin has a Gaussian amplitude distribution.

$$P_n(x) = \frac{1}{\sqrt{2\pi}\,\sigma} \; e^{-\frac{x^2}{2\sigma^2}}$$

where

σ = RMS noise voltage.

To simplify the subsequent calculations, an ideal linear rectifying detector is assumed which is sufficiently accurate in the amplitude range of the signals being considered. Therefore the detector output is

$$S' + n'(x) = |S + n(x)|$$

where

S' = envelope of the detected signal in the absence of noise

$n'(x)$ = output noise voltage.

It is desired to determine the expectation and variance of the detector output signal as a function of the signal-to-noise ratio of the predetection signal. A

great simplification is achieved if a large S/N is assumed which is true in the case of useful echoes. The expectation of the envelope of the detected signal is

$$E(\ |S + n(x)|\ ) = \frac{1}{\sqrt{2\pi}\,\sigma}\int_{-\infty}^{\infty} |S + x|\ e^{-\frac{x^2}{2\sigma^2}}\ dx$$

Changing variables

$$y = \frac{x}{\sigma}$$

$$E(\ |S + n(x)|\ ) = \frac{1}{\sqrt{2\pi}}\int_{-\infty}^{\infty} |S + \sigma y|\ e^{-\frac{y^2}{2}}\ dy$$

But

$$|S + \sigma y| = S + \sigma y \quad \text{for } y > -\frac{S}{\sigma}$$

$$|S + \sigma y| = -(S + \sigma y) \quad \text{for } y < -\frac{S}{\sigma}$$

Also $\frac{S}{\sigma} = \frac{S}{N}$

Therefore the integral becomes

$$E(|S+n(x)|\ ) = \frac{1}{\sqrt{2\pi}}\left[-\int_{-\infty}^{-S/N}(S+\sigma y)e^{-\frac{y^2}{2}}\ dy + \int_{-S/N}^{\infty}(S+\sigma y)e^{-\frac{y^2}{2}}\ dy\ \right]$$

$$= S \qquad \text{(A7.2)}$$

Therefore for high S/N the mean detector output corresponds to the amplitude of the desired signal.

The variance of the detector output signal is

$$\mathrm{Var}(\,|S + n(x)|\,) = E(\,|S + n(x)|\,)^2 - (E(|S+n(x)|))^2$$

The second term is S^2 (eqn. A7.2).

Also

$$E(\,|S + n(x)|\,)^2 = E(S + n(x))^2$$

$$= E(S^2 + 2S \cdot n(x) + n(x)^2)$$

$$= S^2 + 0 + E(n(x)^2)$$

But

$$E(n(x)^2) = \mathrm{Var}\,(n(x)) + (E(n(x)))^2 = \sigma^2 + 0$$

and therefore

$$\mathrm{Var}(S + n(x)) = S^2 + \sigma^2 - S^2 = \sigma^2 \qquad \text{(A7.3)}$$

and the RMS error is σ which is equal to the RMS voltage of the noise at the detector input. It should be noted that this result only applies to large S/N.

The RMS error in the amplitude measurement is given by

$$10 \log \frac{S^2 + \sigma^2}{S^2} \quad \text{(dB)}$$

which in the case of typical echoes with S/N of 20 dB leads to 0.043 dB. Since this value applies to both amplitude measurements, the RMS error in the amplitude ratio is 0.06 dB.

A7.3 Phase Measurements

The following components contribute to the total phase errors.

(a) Error in chart reading

As in the case of the amplitude measurements, this error arises mainly from the thickness of the line on the chart paper. It is approximately 3°.

(b) Calibration errors

The two phase generator used to calibrate the phase channels has an accuracy of 1° which in conjunction with the error due to reading off the chart results in a calibration RMS error of 3.2°.

(c) Errors associated with lateral motion of paper chart are estimated at 5°.

(d) Error due to inter-receiver crosstalk

The good isolation between the receiver makes this error negligible.

(e) Error due to noise

It is shown in the next section that this error is 8° for a typical echo with S/N of 20 db.

The total RMS phase error is

$$\Delta\psi = \sqrt{(a)^2 + (b)^2 + (c)^2 + (e)^2} = 10.5°.$$

A7.3.1 Phase Errors due to Noise

The probability density function of the zero crossing shift due to the presence of narrow band Gaussian noise is (Nowak, 1968)

$$P_n(\Phi) = \frac{S \cos \Phi}{(2\pi)^{3/2}\sigma} e^{-\frac{S^2 \sin^2 \Phi}{2\sigma^2}}$$

where

Φ = zero crossing error.

For a large S/N the error is expected to be small.

Therefore

$$\cos\Phi = 1$$

$$\sin\Phi = \Phi$$

And the normalized density function becomes

$$P_n(\Phi) = \frac{S}{(2\pi)^{3/2}\sigma} e^{-\frac{\Phi^2}{2\sigma^2/S^2}}$$

which represents a Gaussian distribution with RMS error equal to $\frac{\sigma}{S}$ which for the case of S/N = 20 dB is

$$\frac{\sigma}{S} = 0.1 \text{ rad} = 5.7°.$$

This error applies to both signals, therefore the total RMS phase error due to noise is

$$\Delta_n = \sqrt{5.7^2 + 5.7^2} = 8°$$

The height errors shown in Chapter 4 are obtained by assuming errors equal to 1.5 times the RMS values in both the amplitude ratio and phase measurements. Approx-

imately 86% of the solutions have errors within these limits, which thus provide a fair measure of the peak error values.

A7.4 Wind Measurements

The following errors need to be considered:

(a) Error in Doppler period determination

The error in the determination of the Doppler period on the chart paper is approximately 0.2 mm which corresponds to 8 msec. In the case of the highest Doppler frequency this error is equivalent to 10% of the measured wind velocity.

(b) Error due to assumed reflection point position

For a given wind velocity the Doppler shift is a function of the scattering geometry (eqn. A3.7). Therefore the inaccuracy in the position of the reflection point is reflected as an error in the wind determination which is estimated at less than 5%.

(c) Error due to incomplete Doppler information

A more important source of error is present in the short duration echoes where incomplete Doppler cycles are

common. If the available information allowed it, a value of the Doppler period was estimated which could have errors of up to approximately 20%. It should be noted that this error mainly affects the low wind velocity results.

(d) Lack of Doppler sense information

In many cases when very fast Doppler frequencies are present, it is impossible to discern the phase relationship between the lock-in amplifier outputs. Inasmuch as the knowledge of the wind direction is indispensable, the echoes that presented this problem were discarded.

It is therefore estimated that the peak wind velocity error due to system limitations is about 35%, however average errors are expected to be considerably less. In addition, errors resulting from the nature of the measurements are likely to be much larger (section 2.4).

APPENDIX 8

CIRCUIT DESCRIPTIONS

A8.1 General

The block diagram of the receiving system shown in Fig. 13 is reproduced in Fig. 46 for convenience. The first two conversion stages are part of Hamarlund SP 600 communications receivers. Common local oscillators are used throughout to preserve the relative phase difference between the signals at the various channels. The lock-in amplifier is a Princeton Applied Research Mod. JB-6 unit.

A8.2 Third Conversion Stage

The second intermediate frequency signals are fed to converters as shown in Fig. 47 which includes a source follower that applies the converted signal to the subsequent

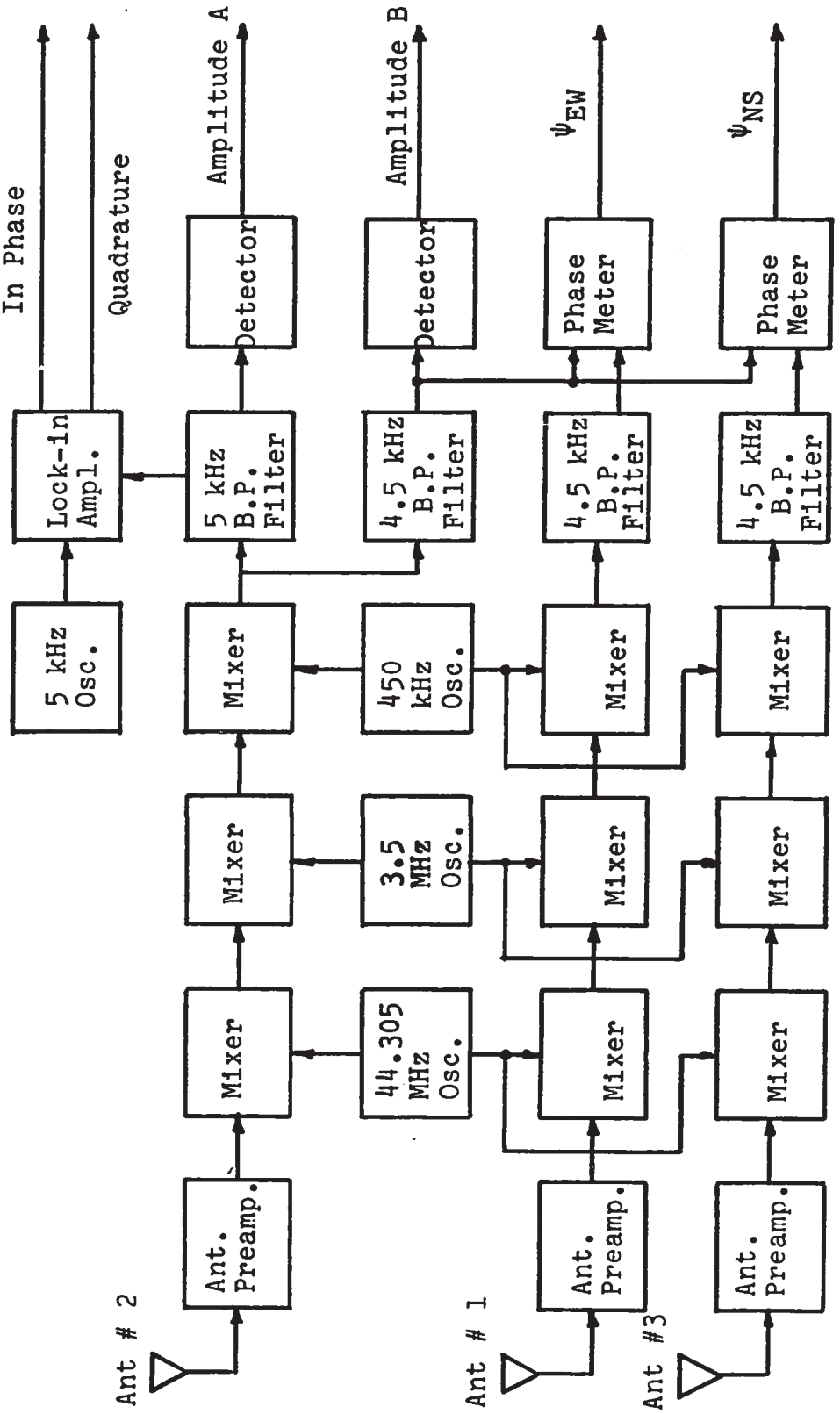

Fig. 46 Receiving system block diagram

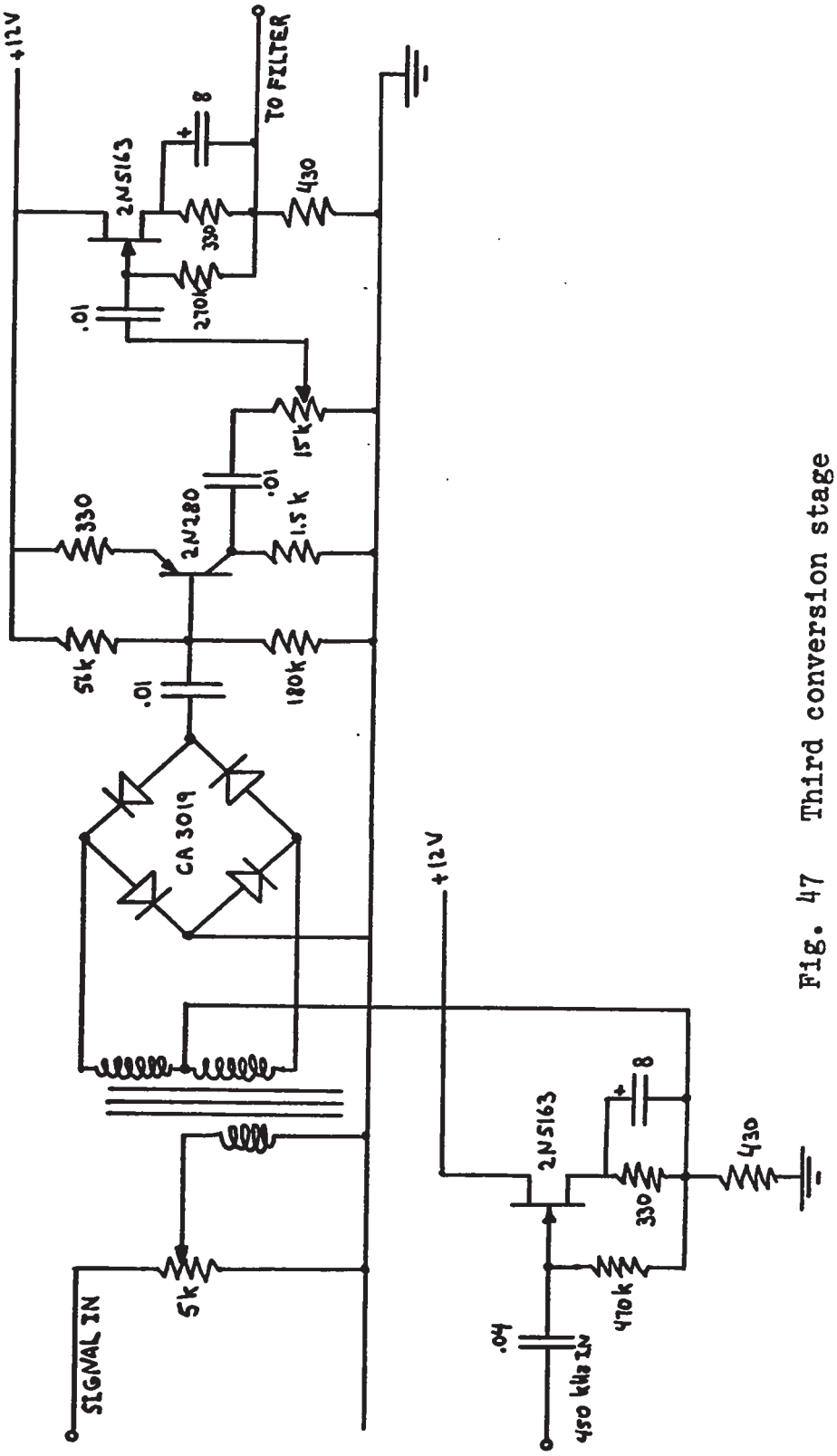

Fig. 47 Third conversion stage

filters. As can be observed in Fig. 46 channel 1 and 3 require the 5.0 kHz notch filter only (Fig. 48), whereas channel 2 must provide both frequencies, thus necessitating two source followers driving the two notch filters. Independent gain control is achieved by means of the 15 kilohm potentiometers.

The second source follower shown in Fig. 47 is an isolation stage between the local oscillator and each of the third converters.

A8.3 Post Filtering Amplifier and Detector

After filtering the signals are amplified (first stage in Fig. 49) and fed into the phasemeters. In the case of channel 2 the signals are subsequently detected (second stage, Fig. 49) in order to obtain the desired amplitude information.

A8.4 Threshold Detector for Time Signal Disabling

Inasmuch as six channels are available on the

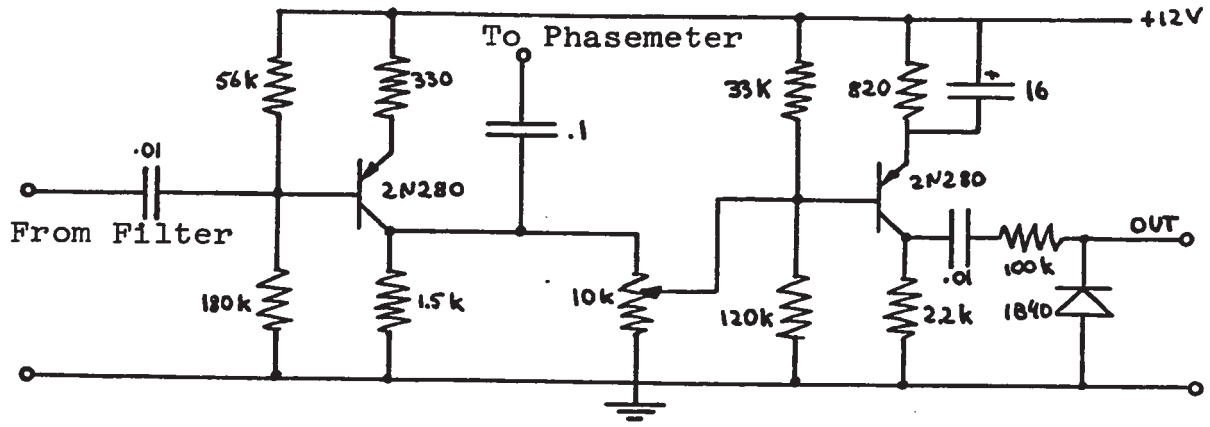

Fig. 49 Amplifier and detector

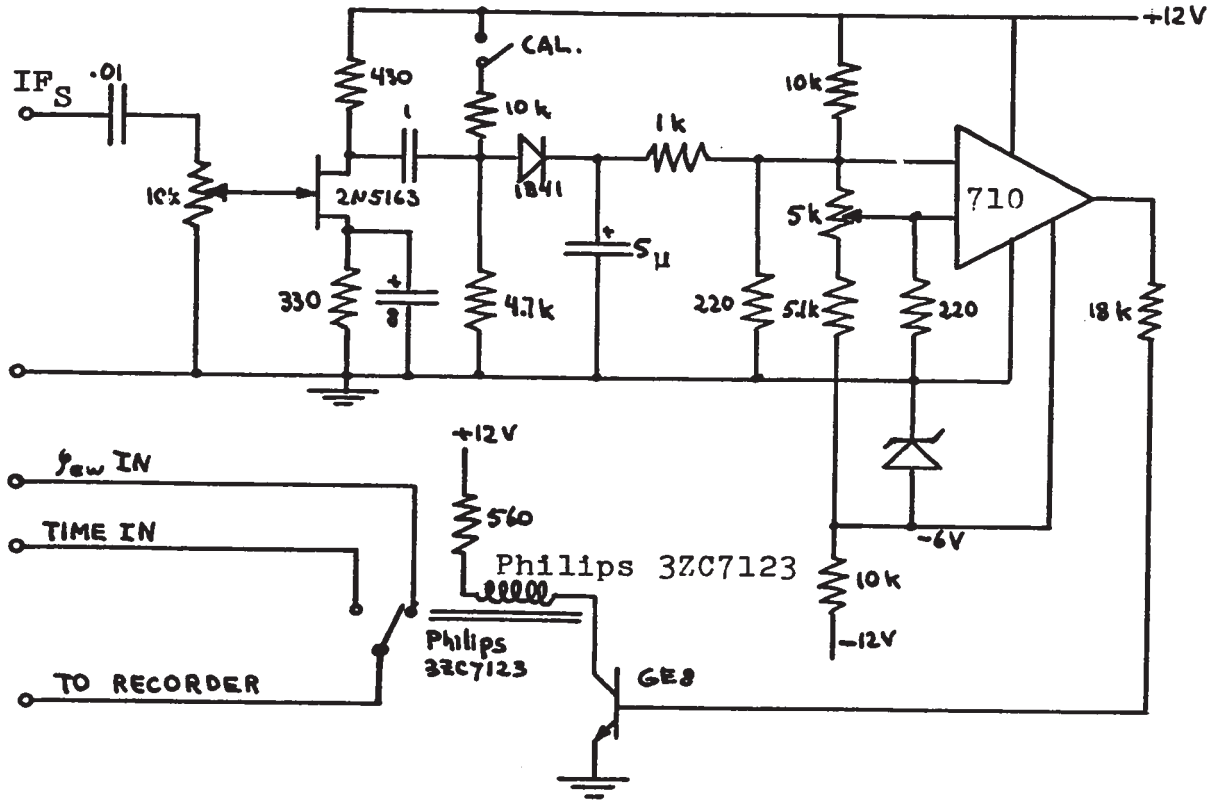

Fig. 50 Threshold detector for time signal disabling

paper chart and seven information channels must be displayed, the time signal which is not necessary on a continuous basis is disabled when a signal exceeding a certain amplitude is detected and in its stead the E-W phase information is recorded.

Fig. 50 depicts the threshold detector. The 4.5 kHZ signal from channel 1 is applied to an amplifier followed by a peak detector that drives a comparator. The gain of the amplifier is controlled by the 10 kΩ potentiometer and the threshold level by adjusting the input offset voltage of the comparator (5kΩ potentiometer). The comparator output is amplified in order to drive the reed relay that switches the recorder between the time and phase information signal. A switch is provided which forces the relay to feed the phase signal to the recorder in order to perform the necessary calibrations.

A8.5 Phase Meters

The phasemeters consist of an amplification stage for each channel followed by clipping circuits whose

outputs are fed into the R and S inputs of an edge driven flip-flop which thus produces a pulse width modulated output with duty cycle (and therefore DC component) proportional to the phase difference between the input signals.

Fig. 51 shows the amplifiers. They are non inverting with a voltage gain of 10. Provision is made for the shifting of one of the signals (A) by 180° by means of an inverter (first stage in Fig. 51). The outputs of the amplifiers are fed into comparators which can be adjusted for zero offset with the 5 kilohm potentiometers. The comparator outputs are differentiated and rectified before being applied to the flip-flop which thus operates on the positive going edges of the comparator outputs (Fig.52). The signal from the flip-flop is subsequently amplified to a suitable value for display on the chart recorder which due to its inherent response time follows the average value of the pulse train.

A8.6 Power Supplies

Fig. 53 shows the + 12 and - 12 Volt regulated power supplies necessary to operate the circuits previously described.

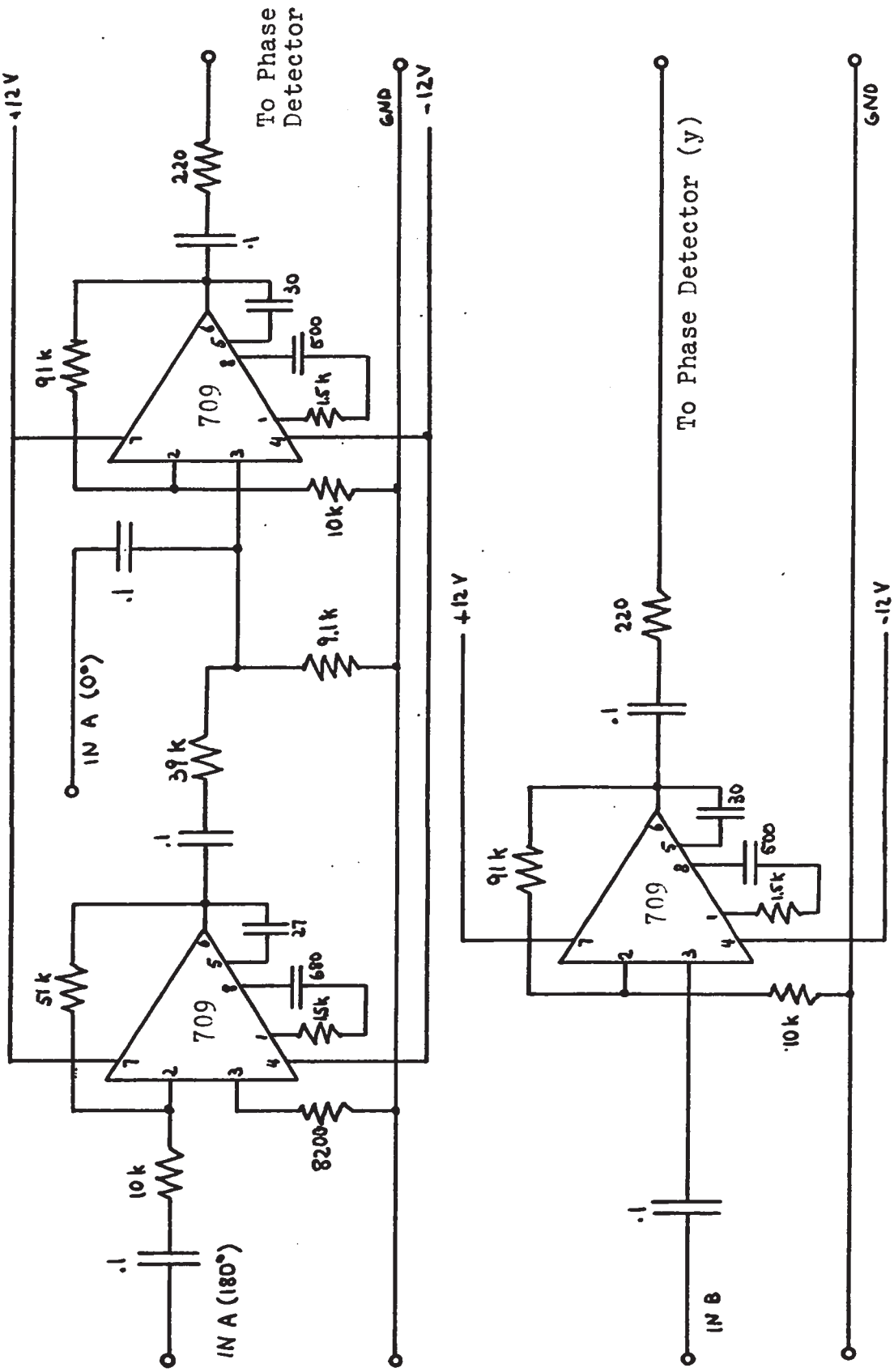

Fig. 51 Phasemeter amplifiers

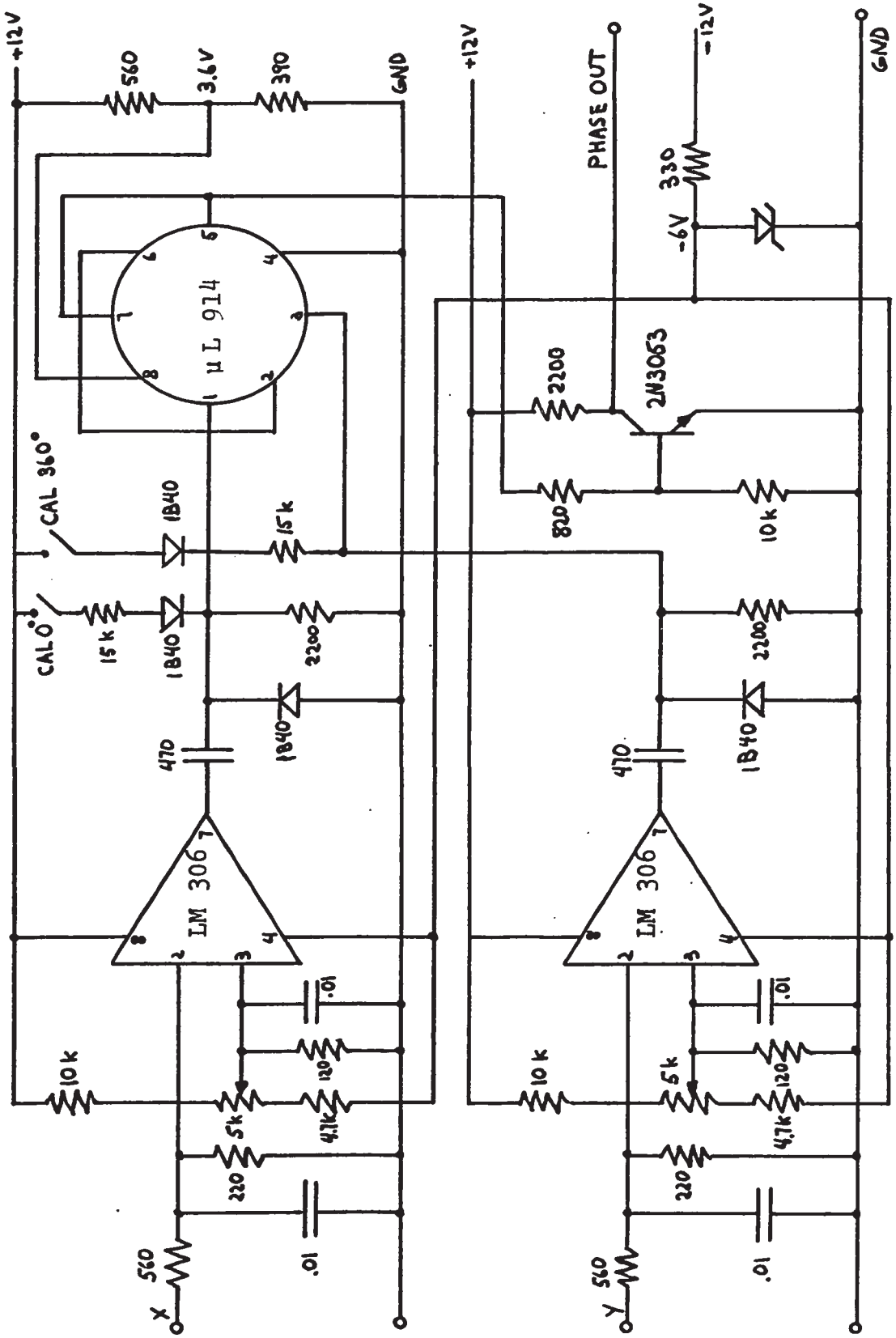

Fig. 52 Phasemeter detector

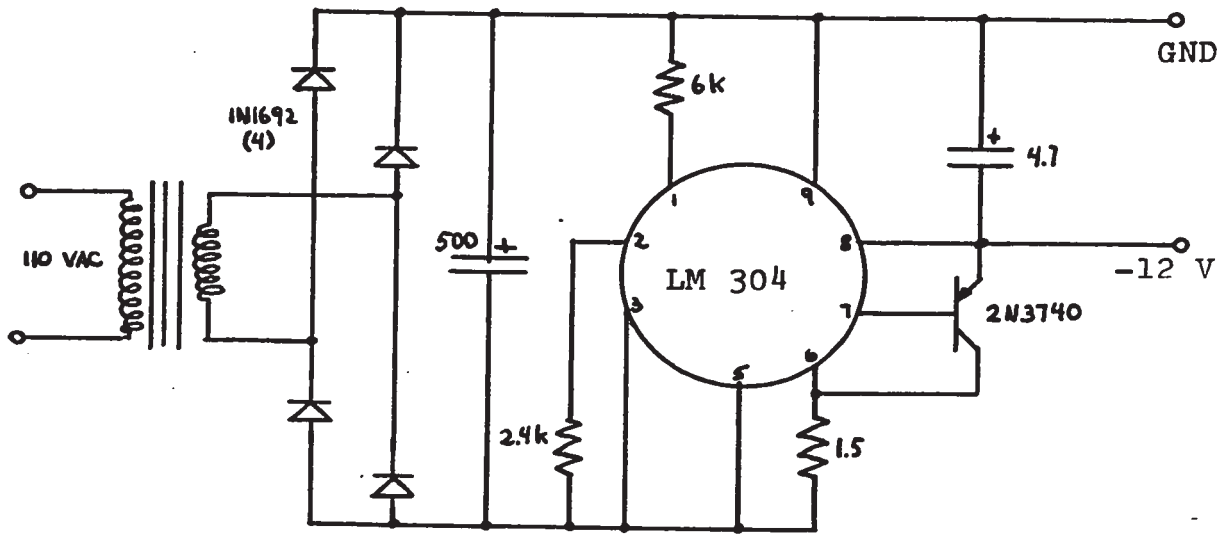

-12 V DC Regulated Power Supply

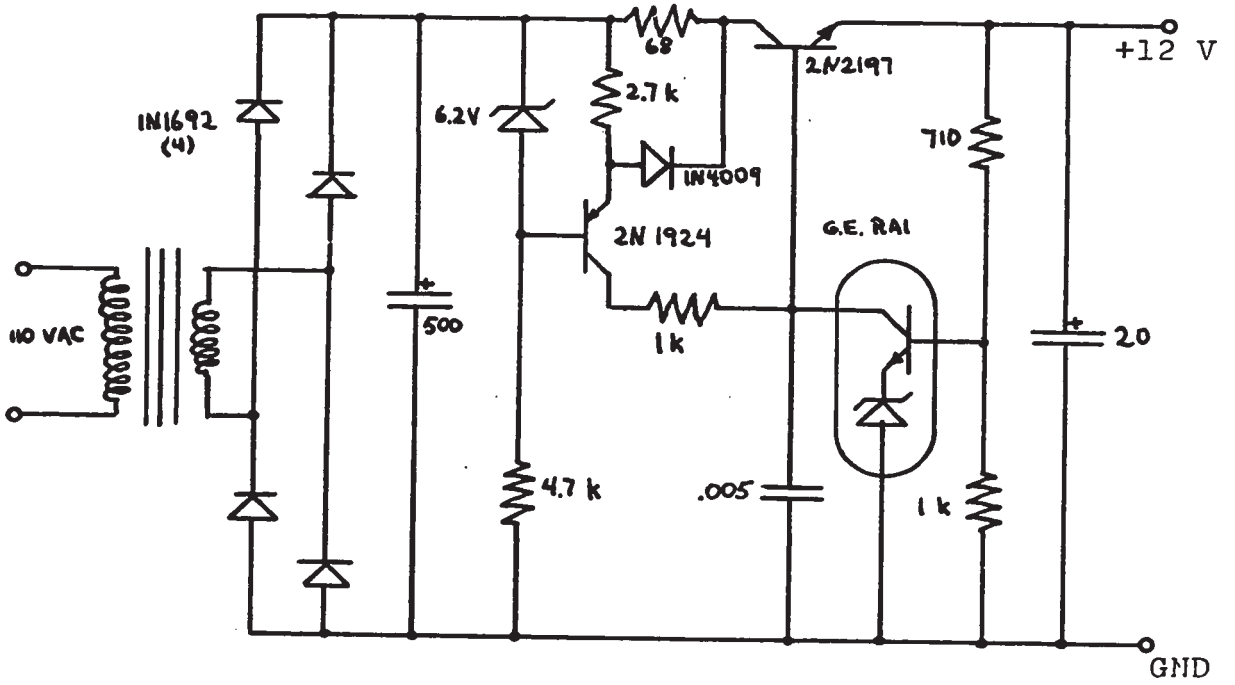

+12 V DC Regulated Power Supply

Fig. 53 Power supplies

REFERENCES

Barnes A. A.	1969	Stratospheric Circulation AIAA Prog.Ser., 22, p.575
Browne I.C., Bullough K., Evans S., Kaiser T.R.	1956	Proc.Phys.Soc., 69B, p. 83-113
Chapman S., Bartels J.	1940	Geomagnetism, 2, p. 557 Clarendon Press, Oxford.
Crysdale J.H., Olive D.J.	1956	DRTE Project Report 12-0-1
Elford W. G.	1959	Planet. Sp.Sc., 1, p. 94
	1968	AFCRL-68-0228* Rept., No. 75, p. 11
Elford W.G., Robertson D.S.	1953	J.Atmos. Terr Phys., 4, p. 271
Frost A., Clark R., Glanz F., Catala P.	1970	Final report AFCRL-70-0541
Greenhow J.S.	1952	Proc.Phys.Soc., 65B, p.169
Greenhow J.S.,Neufeld E.L.	1955a	J.Atmos.Terr.Phys., 6, p. 133
	1955b	Phil. Mag., 46, p. 549
	1956	Ibid., 1, p. 1157
	1959a	J.Geophys.Res., 64, p. 2129
	1959b	Proc.Phys.Soc., 74, p.1
	1960	Ibid., 75, p. 228
Grossi M.	1968	AFCRL-68-0228* Rept. No.75 p. 29

Hines C.O.	1960	Ibid., 38, p. 1441
	1963	Q.J.R.Met.Soc., 89,p. 1
	1965	Physics of the earth's upper atmosphere. Englewood Cliffs, N.J.
Hines C.O., Forsyth P.A.	1957	Can.J.Phys., 35, p.1033
Jordan E.C.	1950	Electromagnetic waves and radiating systems. Prentice Hall, N.J.
Kaiser T.R.	1954a	Mon.Not.R.Ast.Soc., 114, p. 39
	1954b	Ibid., 114, p. 52
Kaiser T.R.,Pickering W.M., Watkins C.D.	1969	Planet. Space Sci., 17, p. 519
Kashcheyev B.L., Lysenko I.A.	1968	J.Atmos.Terr.Phys., 30, p. 903
Kato S.	1956	J.Geomag.Geoelectr., 8, p. 24
Kent G.S., Wright R.W.H.	1968	J.Atmos.Terr.Phys., 30, p. 657
Kochanski A.	1964	J.Geophys. Res., 69, p. 3651
Kraus J.D.	1950	Antennas, McGraw-Hill
	1966	Radio Astronomy, McGraw-Hill
Lovell A.C.B.	1954	Meteor Astronomy, p. 108-122, Oxford Press
Manning L.A.,Villard O.G., Peterson A.M.	1950	Proc. IRE, 38, p. 877
McKinley D.W.R.	1961	Meteor Science and Eng., McGraw-Hill
Murray E.L.	1959	Planet.Spa.Sci., 1,p.125
Nowak R.	1968	AFCRL-68-0228* Rept. No.75 p. 131

Pawsey J.L., Bracewell R.N.	1955	Radio Astronomy, Clarendon Press, Oxford
Pazniokas J.	1968	AFCRL-68-0228* Rept. No.75 p. 139
Peterson A.	1968	Ibid., p. 275
Peterson A., Nowak R.	1968	Ibid., p. 67
Ramsey W., Myers R.	1968	Ibid., p. 39
Rice D.W., Forsyth P.A.	1963	Can.J.Phys., 41, p. 679
	1964	Ibid., 42, p. 2035
Robertson D.S., Liddy D.T., Elford W.G.	1953	J.Atmos.Terr.Phys., 4, p. 255
Roper R.G.	1966	J.Geophys.Res., 71, p. 2785
	1968	AFCRL-68-0228* Rept.No.75, p. 107
Southworth R.	1968	Ibid., p. 161
Spizzichino A., Revah I.	1968	Space Research, VIII, p. 679-682
Spizzichino A., Delcourt J., Girand A., Revah I.	1965	Proc. IEEE, 53, p. 1084
Tiuri M.E.	1964	IEEE Trans.Ante and Propag., AP-12, p. 939
Weiss A.A.	1955	Austr. J. Phys., 8, p.279
Weiss A.A.	1957	Ibid., 10, p. 77

* Proceedings of the Workshop on Methods of Obtaining Winds and Densities from Radar Meteor Trail Returns. Ed. Barnes A.A. Pazniokas J.J. Air Force Cambridge Research Laboratories, Mass.